

**HEAT TRANSFER IN TURBULENT CHANNEL FLOW WITH  
ROUGHNESS ON THE WALLS: NUMERICAL SIMULATION**

By

Amabel Reyes Rondon

A thesis submitted in partial fulfillment of the requirements for the degree of

MASTER OF SCIENCE

in

MECHANICAL ENGINEERING

UNIVERSITY OF PUERTO RICO  
MAYAGÜEZ CAMPUS

December, 2011

Approved by:

---

Stefano Leonardi, Ph.D  
Member, Graduate Committee

---

Date

---

Vikram R. Pandya, Ph.D  
Member, Graduate Committee

---

Date

---

Silvina Cancelos, Ph.D  
President, Graduate Committee

---

Date

---

Aldo Acevedo, Ph.D  
Representative of Graduate Studies

---

Date

---

Gustavo Gutierrez, Ph.D  
Chairperson of the Department

---

Date

Abstract of Thesis Presented to the Graduate School  
of the University of Puerto Rico in Partial Fulfillment of the  
Requirements for the Degree of Master of Science

**HEAT TRANSFER IN TURBULENT CHANNEL FLOW WITH  
ROUGHNESS ON THE WALLS: NUMERICAL SIMULATION**

By

Amabel Reyes Rondon

December 2011

Chair: Stefano Leonardi

Major Department: Mechanical Engineering

Reynolds Average Navier Stokes (RANS) simulations are performed to study a turbulent channel flow with different roughness on the lower and upper walls. Several roughness were used. Square Bars, V-shaped and segmented V-shaped with a  $p/e$  ratio equal to 1, 3, 5, 8, 10 and 15, where  $e$  is the bar height and  $p$  is the longitudinal separation between consecutive bars. The height of the turbulators was choose  $e/H = 0.25$ , where  $H$  is the channel half-height. The V-shaped and segmented V-shaped turbulators have an inclination angle with respect to the flow direction of  $45^\circ$ . For the segmented V-shaped turbulators case the used gap size was  $G/H = 0.2$  (where  $G$  is the width of the space in the middle of the ribs). The different types of roughness analyzed showed the most efficient cases for each roughness geometry. For the square Bars turbulators a pitch to height ratio,  $p/e$  equal to 10 presents the highest Nusselt number (Nu). For the V-shaped turbulators the most efficient configuration is that with  $p/e = 5$ . The segmented V-shaped turbulators present the highest Nu when compared with all the geometries considered. The  $p/e = 3$

configuration leads to the highest convective heat transfer. This is due to the vortices created at the sidewalls that eject the heat out of the turbulator cavity.

Resumen de Tesis Presentado a Escuela Graduada  
de la Universidad de Puerto Rico como requisito parcial de los  
Requerimientos para el grado de Maestría en Ciencias

**TRANSFERENCIA DE CALOR EN UN CANAL DE FLUJO  
TURBULENTO CON RUGOSIDAD EN LAS PAREDES:  
SIMULACIÓN NUMÉRICA**

Por

Amabel Reyes Rondon

Diciembre 2011

Consejero: Stefano Leonardi  
Departamento: Ingeniería Mecánica

Una simulación de Reynolds Average Navier Stokes (RANS) fue realizada para estudiar un canal con flujo turbulento con diferentes rugosidades en la pared de arriba y abajo. Diferentes rugosidades fueron utilizadas, barras cuadradas, barras en forma de V y barras en forma de V segmentadas con un radio  $p/e$  igual a 1, 3, 5, 8, 10 y 15, donde  $e$  es el alto de la barra y  $p$  es la separación longitudinal entre barras consecutivas. La altura de los turbuladores fue seleccionado como  $e/H = 0.25$ , donde  $H$  es la altura de la mitad del canal. Los turbuladores de barras en forma de V y barras en forma de V segmentadas tienen un ángulo de inclinación con respecto a la dirección del fluido de  $45^\circ$ . Para los turbuladores de barras en forma de V segmentadas el tamaño de la brecha en el medio de los turbuladores es  $G/H = 0.2$ , donde  $G$  es el ancho del espacio entre las barras. Los diferentes tipos de rugosidades analizados mostrarán el caso más eficiente para cada geometría de rugosidades. Para los turbuladores de barras cuadradas el radio de largo con respecto a altura de  $p/e = 10$  presento el mayor número de Nusselt. Para los turbuladores de barras en forma de

V la configuración más eficiente es aquella con  $p/e = 5$ . Los turbuladores de barras en forma de V segmentadas presento el mayor Nu cuando es comparado con todos los casos de rugosidades. La configuración de  $p/e = 3$  presento la mayor transferencia de calor convectiva. Esto es causado por los vórtices creado en las pareces de los lados que expulsan el calor hacia afuera de la cavidad de los turbuladores.

Copyright © 2011

by

Amabel Reyes Rondon

I want to dedicate this thesis to my family, especially to my father Amado Reyes for being an example for me and always being in my live. Also, to my boyfriend Carlo Otaño for his help and support.

## ACKNOWLEDGMENTS

I would like to thank Professor Stefano Leonardi for his help throughout my master's degree and for giving me the opportunity to work with him. This opportunity will give me the knowledge that I will use in my future studies and my career. I am very thankful for the teaching of all my master's professors that help me to understand for my master degree and my thesis. Thanks very much to all my laboratory partners for helping me in different ways in my research, especially to Benjamin Cruz and John Lucena. Finally, I want to thanks Pratt & Whitney for funding this research and giving me this wonderful opportunity.

## TABLE OF CONTENTS

		<u>page</u>
ABSTRACT ENGLISH	.....	ii
ABSTRACT SPANISH	.....	iv
ACKNOWLEDGMENTS	.....	viii
LIST OF TABLES	.....	xi
LIST OF FIGURES	.....	xii
LIST OF ABBREVIATIONS	.....	xvii
LIST OF SYMBOLS	.....	xviii
1	INTRODUCTION	1
2	JUSTIFICATION	9
3	NUMERICAL METHOD	10
	3.1 Governing Equation	10
	3.2 Mesh generation (Gambit)	11
	3.3 Numerical Solution of Governing Equations (Fluent)	13
	3.3.1 Problem Setup	14
	3.4 Sub Grid Model (RANS)	15
	3.5 Boundary Conditions	18
	3.6 Initial Condition	19
	3.7 Reference Values	19
4	SMOOTH CHANNEL	22
5	SQUARE BARS TURBULATORS	27
	5.1 Mean Flow	28
	5.2 Velocity Root Mean Square (RMS)	31
	5.3 Mean Temperature	34
	5.4 Root Mean Square Temperature	35
	5.5 Nusselt Number	35
	5.6 Skin Friction and Form Drag	36

6	V-SHAPED TURBULATORS . . . . .	39
6.1	Mean Flow . . . . .	40
6.2	Velocity Root Mean Square (RMS) . . . . .	46
6.3	Mean Temperature . . . . .	48
6.4	Root Mean Square (RMS) Temperature . . . . .	50
6.5	Nusselt Number . . . . .	52
6.6	Frictional Drag and Form Drag . . . . .	52
6.7	Comparison between the RANS model with DNS (V-Shaped) . . . . .	53
7	SEGMENTED V-SHAPED TURBULATORS . . . . .	59
7.1	Mean Flow . . . . .	59
7.2	Root Mean Square (RMS) Velocity . . . . .	62
7.3	Mean Temperature . . . . .	67
7.4	Root Mean Square (RMS) Temperature . . . . .	68
7.5	Nusselt Number . . . . .	69
7.6	Frictional Drag and Form Drag . . . . .	69
8	CONCLUSION AND FUTURE WORK . . . . .	71
	APPENDICES . . . . .	75
A	. . . . .	76
B	. . . . .	79
B.1	Flow Configuration . . . . .	79
B.2	Mean Flow . . . . .	80
B.3	Root Mean Square (RMS) Velocity . . . . .	82
B.4	Mean Temperature . . . . .	84
B.5	Root Mean Square Temperature . . . . .	85
B.6	Nusselt Number . . . . .	85
B.7	Skin Friction and Form Drag . . . . .	86

LIST OF TABLES

<u>Table</u>		<u>page</u>
3-1	<b>Initial Values to Setup Fluent</b> . . . . .	19
3-2	<b>Reference Values Used in Fluent</b> . . . . .	20

LIST OF FIGURES

<u>Figure</u>	<u>page</u>
1-1 <b>Left: Sketch of a gas turbine. Right: Air-standard ideal Brayton cycle.</b> . . . . .	2
1-2 <b>Cooling Configuration System.</b> . . . . .	3
2-1 <b>Left: Cooling Configuration System. Right: Example of a Damage Turbine Blade</b> . . . . .	9
3-1 <b>Quadrilateral/Hexahedral (Quad/Hex) Mesh.</b> . . . . .	12
3-2 <b>Triangle/Tetrahedral (Tri/Tet) Mesh.</b> . . . . .	13
4-1 <b>Smooth Channel Configuration</b> . . . . .	22
4-2 <b>Streamwise Average Velocity Profile of a Channel Flow. (—) DNS and (----) RANS</b> . . . . .	23
4-3 <b>Average Velocity Contour in the Streamwise Direction.</b> . . . . .	24
4-4 <b>Temperature Profile of a Channel Flow. (—) DNS and (----) RANS</b> . . . . .	24
5-1 <b>Left: Square Bars Turbulators Sketch. Right: 3-D Square Bars Turbulators Configuration.</b> . . . . .	27
5-2 <b>Streamwise Average Velocity profile distribution for Square Bars turbulators. Upper: Aligned, Lower: Staggered.</b> . . . . .	28
5-3 <b>Normal Average Velocity profile distribution for Square Bars turbulators. Upper: Aligned, Lower: Staggered.</b> . . . . .	29
5-4 <b>Side view of average velocity vectors in a contour of average velocity of the streamwise direction for Square Bars turbulators.</b> . . . . .	30
5-5 <b>Velocity Streamtracer in the Streamwise Direction for Square Bars turbulators.</b> . . . . .	31
5-6 <b>Streamwise Velocity RMS average in time for Square Bars turbulators. Upper: Aligned, Lower: Staggered.</b> . . . . .	32

5-7	Normal Velocity RMS average in time for Square Bars turbulators. Upper: Aligned, Lower: Staggered. . . . .	33
5-8	Temperature profile distribution for Square Bars turbulators. Upper: Aligned, Lower: Staggered. . . . .	34
5-9	Temperature RMS average in time for Square Bars turbulators. Upper: Aligned, Lower: Staggered. . . . .	36
5-10	The Nusselt Number on different $p/e$ for Square Bars turbulators. Left: Aligned, Right: Staggered. . . . .	37
5-11	Dependence of the skin frictional $C_f$ ( $\times$ ), form drag $P_d$ ( $*$ ) and total drag $C_f + P_d$ ( $\blacksquare$ ) on different $p/e$ for Square Bars turbulators. Left: Aligned, Right: Staggered. . . . .	37
6-1	Left: V-Shaped Turbulators Sketch in a Staggered Position. Right: 3-D V-Shaped Turbulators Configuration. . . . .	39
6-2	Top: Top view of the Normal Average Velocity contour with velocity vectors for V-Shaped turbulators (Left: $p/e=1$ , Right: $p/e=3$ ). Bottom: Side view of the Spanwise Average Velocity contour with velocity vector for the V-shaped turbulators (Left: $p/e=1$ , Right: $p/e=3$ ). . . . .	40
6-3	Top Left: Normal Average Velocity Contour with velocity vectors for $p/e=8$ for V-Shaped turbulators. Bottom Left: Spanwise Average Velocity contour with velocity vector for $p/e=8$ for the V-Shaped turbulators. . . . .	41
6-4	Streamwise Average Velocity profile distribution for V-Shaped turbulators. Upper: Aligned, Lower: Staggered. . . . .	42
6-5	Normal Average Velocity profile distribution for V-Shaped turbulators. Upper: Aligned, Lower: Staggered. . . . .	43
6-6	Average Velocity contour for the three direction in the $p/e = 3$ configuration for V-Shaped turbulators. (A) Streamwise Average Velocity. (B) Normal Average Velocity. (C) Spanwise Average Velocity. . . . .	45
6-7	Velocity Streamtracer in the Streamwise Direction for V-Shape turbulators. . . . .	46
6-8	Streamwise Velocity RMS average in space for V-Shape turbulators. Upper: Aligned, Lower: Staggered. . . . .	47
6-9	Normal Velocity RMS average in space for V-Shape turbulators. Upper: Aligned, Lower: Staggered. . . . .	48

6-10	Spanwise Velocity RMS average in space for V-Shape turbulators. Upper: Aligned, Lower: Staggered. . . . .	49
6-11	Temperature profile distribution for V-Shape turbulators. Upper: Aligned, Lower: Staggered. . . . .	50
6-12	Temperature RMS average in space for V-Shape turbulators. Upper: Aligned, Lower: Staggered. . . . .	51
6-13	The Nusselt Number on different $p/e$ for V-Shape turbulators. Left: Aligned, Right: Staggered. . . . .	52
6-14	Dependence of the Skin Frictional $C_f$ ( $\times$ ), Form Drag $P_d$ ( $*$ ) and Total Drag $C_f + P_d$ ( $\blacksquare$ ) on different $p/e$ for the V-Shape turbulators. Left: Aligned, Right: Staggered. . . . .	53
6-15	Streamwise Average Velocity profile distribution for V-Shaped turbulators: (—) RANS, (----) DNS. . . . .	54
6-16	Streamwise Velocity RMS average in space for V-Shape turbulators: (—) RANS, (----) DNS. . . . .	54
6-17	Normal Velocity RMS average in space for V-Shape turbulators: (—) RANS, (----) DNS. . . . .	55
6-18	Spanwise Average Velocity RMS average in space for V-Shape turbulators: (—) RANS, (----) DNS. . . . .	56
6-19	Temperature profile distribution for V-Shape turbulators. (—) RANS, (----) DNS. . . . .	56
6-20	Temperature RMS average in space for V-Shape turbulators. (—) RANS, (----) DNS. . . . .	57
6-21	Nusselt Number Comparison for the DNS and RANS model.	58
7-1	Left: Segmented V-Shaped Turbulators Sketch. Right: 3-D Segmented V-Shaped Turbulators Configuration. . . . .	59
7-2	Streamwise Average Velocity profile distribution for Segmented V-Shaped turbulators. Upper: Aligned, Lower: Staggered. . . . .	60
7-3	Normal Average Velocity profile distribution for Segmented V-Shaped turbulators. Upper: Aligned, Lower: Staggered.	61
7-4	Velocity Streamtracer in the Streamwise Direction for Segmented V-Shaped turbulators. . . . .	62

7-5	Velocity contour for the three direction in the $p/e = 3$ configuration for Segmented V-Shaped turbulators. (A) Streamwise Average Velocity. (B) Normal Average Velocity. (C) Spanwise Average Velocity. . . . .	63
7-6	Streamwise Velocity RMS average in time for Segmented V-Shaped turbulators. Upper: Aligned, Lower: Staggered. . .	64
7-7	Normal Velocity RMS average in time for Segmented V-Shaped turbulators. Upper: Aligned, Lower: Staggered. . .	65
7-8	Spanwise Velocity RMS average in time for Segmented V-Shaped turbulators. Upper: Aligned, Lower: Staggered. . .	66
7-9	Temperature profile distribution for Segmented V-Shaped turbulators. Upper: Aligned, Lower: Staggered. . . . .	67
7-10	Temperature RMS average in time for Segmented V-Shaped turbulators. Upper: Aligned, Lower: Staggered. . . . .	68
7-11	The Nusselt Number on different $p/e$ for Segmented V-Shaped turbulators. Left: Aligned, Right: Staggered . . . . .	69
7-12	Dependence of the Skin Frictional $C_f$ ( $\times$ ), Form Drag $P_d$ ( $*$ ) and Total Drag $C_f + P_d$ ( $\blacksquare$ ) on different $p/e$ for Segmented V-Shaped turbulators. Left: Aligned, Right: Staggered . .	70
8-1	Nusselt Number Comparison . . . . .	72
8-2	Dependence of the Form Drag $P_d$ for Square Bars Turbulators ( $\square$ ), V-Shaped Turbulators ( $*$ ) and Segmented V-Shaped Turbulators ( $\blacksquare$ ) on different $p/e$ . Left: Aligned, Right: Staggered . . . . .	72
8-3	Dependence of the Frictional Drag $C_f$ for Square Bars Turbulators ( $\square$ ), V-Shaped ( $*$ ) and Segmented V-Shaped ( $\blacksquare$ ) on different $p/e$ . Left: Aligned, Right: Staggered . . . . .	73
8-4	Dependence of the Total Drag $C_f + P_d$ for Square Bars Turbulators ( $\square$ ), V-Shaped ( $*$ ) and Segmented V-Shaped ( $\blacksquare$ ) on different $p/e$ . Left: Aligned, Right: Staggered . . . . .	74
B-1	Left: V-Shaped Turbulators Sketch. Right: 3-D V-Shaped Turbulators Configuration. . . . .	79
B-2	Left: Square Bars Inclined Turbulators Sketch. Right: 3-D Square Bars Inclined Turbulators Configuration. . . . .	80

B-3	<b>Streamwise Average Velocity profile distribution for different ribs turbulators:</b> (+) <i>V - Shaped 45°</i> , (—) <i>V - Shaped 60°</i> , (----) <i>V - Shaped 75°</i> , (-----) <i>Inclined Ribs 45°</i> , (...) <i>Inclined Ribs 60°</i> , (---) <i>Inclined Ribs 90°</i> . . . . .	81
B-4	<b>Normal Average Velocity profile distribution for different ribs turbulators:</b> (+) <i>V - Shaped 45°</i> , (—) <i>V - Shaped 60°</i> , (----) <i>V - Shaped 75°</i> , (-----) <i>Inclined Ribs 45°</i> , (...) <i>Inclined Ribs 60°</i> , (---) <i>Inclined Ribs 90°</i> . . . . .	81
B-5	<b>Streamwise Velocity RMS average in space for different ribs turbulators.</b> (+) <i>V - Shaped 45°</i> , (—) <i>V - Shaped 60°</i> , (----) <i>V - Shaped 75°</i> , (-----) <i>Inclined Ribs 45°</i> , (...) <i>Inclined Ribs 60°</i> , (---) <i>Inclined Ribs 90°</i> . . . . .	82
B-6	<b>Normal Velocity RMS average in space for different ribs turbulators.</b> (+) <i>V - Shaped 45°</i> , (—) <i>V - Shaped 60°</i> , (----) <i>V - Shaped 75°</i> , (-----) <i>Inclined Ribs 45°</i> , (...) <i>Inclined Ribs 60°</i> , (---) <i>Inclined Ribs 90°</i> . . . . .	83
B-7	<b>Spanwise Velocity RMS average in space for different ribs turbulators.</b> (+) <i>V - Shaped 45°</i> , (—) <i>V - Shaped 60°</i> , (----) <i>V - Shaped 75°</i> , (-----) <i>Inclined Ribs 45°</i> , (...) <i>Inclined Ribs 60°</i> , (---) <i>Inclined Ribs 90°</i> . . . . .	83
B-8	<b>Temperature profile distribution for different ribs turbulators:</b> (+) <i>V - Shaped 45°</i> , (—) <i>V - Shaped 60°</i> , (----) <i>V - Shaped 75°</i> , (-----) <i>Inclined Ribs 45°</i> , (...) <i>Inclined Ribs 60°</i> , (---) <i>Inclined Ribs 90°</i> . . . . .	84
B-9	<b>Temperature RMS average in space for different ribs turbulators.</b> (+) <i>V - Shaped 45°</i> , (—) <i>V - Shaped 60°</i> , (----) <i>V - Shaped 75°</i> , (-----) <i>Inclined Ribs 45°</i> , (...) <i>Inclined Ribs 60°</i> , (---) <i>Inclined Ribs 90°</i> . . . . .	85
B-10	<b>The Nusselt Number for different configurations of ribs turbulators.</b> (+) <i>V-Shape</i> and (*) <i>Square Bars</i> . . . . .	86
B-11	<b>Dependence of the different drag component for different ribs turbulators:</b> $C_f$ ( $\times$ ), form drag $P_d$ (*) and total drag $C_f + P_d$ ( $\circ$ ). <b>Left: Square Bars Turbulators Inclined , Right: V-Shape Turbulators.</b> . . . . .	86

## LIST OF ABBREVIATIONS

DNS	Direct Numerical Simulation.
FAS	Full Approximation Storage.
FMG	Full Multigrid.
LES	Large Eddy Simulation.
RANS	Reynolds Average Navier Stokes.
RKE	Realizable $k - \epsilon$ .
RMS	Root Mean Square.
RNG	Renormalization group.

## LIST OF SYMBOLS

$\omega_k$	Angular Velocity
$\bar{p}$	Average Pressure
$U_b$	Bulk Velocity
$\beta$	Coefficient of Thermal Expansion
$g_i$	Component of the Gravitational Vector in the $i$ Direction
$\rho$	Density
$\vec{J}_j$	Diffusion Flux of the Species $j$
$\underline{y}^*$	Dimensionless Normal Direction
$\bar{T}$	Dimensionless Temperature
$\mu_t$	Eddy Viscosity
$k_{eff}$	Effective Conductivity
$\eta$	Efficiency
$\bar{u}_i$	Ensemble-Average Velocity
$h$	Enthalpy of an Ideal Gases
$s$	Entropy
$F$	Fahrenheit
$P_d$	Form Drag
$G_b$	Generation of the Turbulent Kinetic Energy due to Buoyancy
$G_k$	Generation of the Turbulent Kinetic Energy due to the Mean Velocity
	Gradients
$\rho\vec{g}$	Gravitational Body Force
$q$	Heat Flux
$U$	Instantaneous Velocity
$\nu$	Kinematic Viscosity
$\delta_{ij}$	Kronecker Delta
$h_f$	Local Heat Transfer Coefficient
$p$	Longitudinal Separation between Consecutive Bars
$Y_j$	Mass Fraction Species $j$
$\bar{\Omega}_{ij}$	Mean Rate-of-Rotation Tensor
$H$	Mid-Channel Height
$\mu$	Molecular Viscosity
$\bar{v}$	Normal Average Velocity
$Nu$	Nusselt Number
$\lambda$	Pitch
$Pr$	Prandtl Number
$s_{ij}$	Rate of Strain
$T_{ref}$	Reference Temperature
$Re$	Reynolds Number

$e$	Roughness Height
$\overline{\rho u'_i u'_j}$	Reynolds Stress Tensor
$C_f$	Skin Frictional Drag
$\overline{w}$	Spanwise Average Velocity
$a$	Speed of Sound
$p$	Static Pressure
$\overline{u}$	Streamwise Average Velocity
$\overline{\sigma}$	Stress Tensor
$T$	Temperature
$t$	Time
$\epsilon$	Turbulent Dissipation
$C_D$	Total Drag
$k$	Turbulent Kinetic Energy
$M_t$	Turbulent Mach Number
$Pr_t$	Turbulent Prandtl Number
$k_t$	Turbulent Thermal Conductivity
$I$	Unit Tensor
$u'_i$	Velocity Fluctuation
$\tau_w$	Wall Shear Stress
$T_w$	Wall Surface Temperature
$G$	Width of the Space in the Middle of the Ribs Turbulators

# CHAPTER 1

## INTRODUCTION

To improve turbulent heat transfer in electronic cooling devices, heat exchangers and turbine blades different techniques are used, for examples the use of pin fins, swirl chambers and the rib turbulators [1]. These improvements are partly responsible for many innovations in our daily lives, like smaller computers, more efficient engines and power plants. According to Kim & Lee (2007) the use of high-performance computers has been increasing in the last decade. These computers are used to develop numerical optimization techniques based in Reynolds-Averaged Navier-Stokes analysis. The development of high-performance computers has allowed us to solve many complicated numerical problems which would have been very difficult to solve in the past.

Advanced gas turbine engines operate at high temperatures (1600K-1700K) to improve thermal efficiency and power output. As the turbine inlet temperature increases, the thermal stresses in the blade increase too limiting the durability of the turbine [2]. For this reason, it is necessary to optimize the cooling technique, operation system, and turbine blade cooling system geometry.

A schematic of a gas turbine power plant is shown in Figure 1–1 (Left). This figure shows a simple gas turbine open to the atmosphere. With an air-standard analysis, the complexities of the combustion process are avoided. The idealization of the cycle is called the air-standard Brayton cycle. Figure 1–1 (Right) shows the  $T - s$  diagram of this ideal cycle [3].

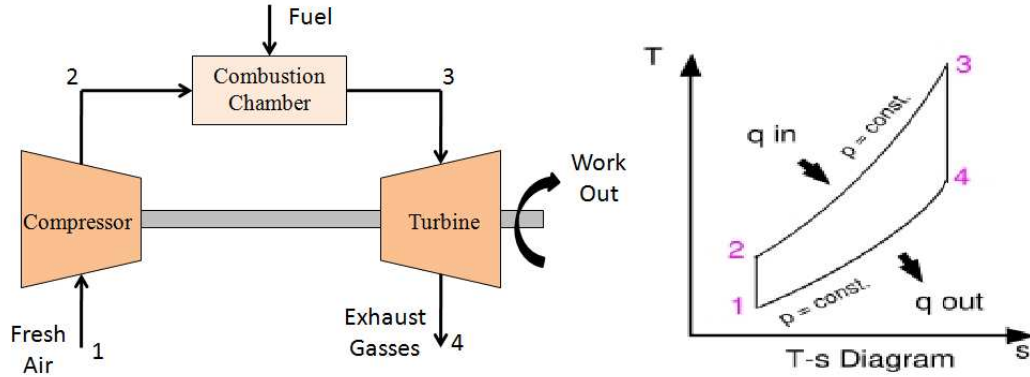


**Figure 1–1: Left: Sketch of a gas turbine. Right: Air-standard ideal Brayton cycle.**

On the  $T - s$  diagram, the area 2 – 3 represents the heat added per unit mass and area 1 – 4 is the heat rejected per unit mass. To determine the efficiency of the cycle is important to know the temperature in the entrance and exit of the turbine. The equation of the cycle thermal efficiency is

$$\eta = 1 - \frac{T_4}{T_3} \quad (1.1)$$

The efficiency depends on the temperature at the entrance of the turbine. The higher the inlet temperature of the turbine, the higher the efficiency of the system.

To resist at these high temperature, cooling techniques are used in the turbine blades. Figure 1–2 shows the stage-1 internally cooling high-pressure turbine rotor blade for a turbofan engine. This figure shows the different cooling techniques of the blades: internally and externally. The external cooling consists of a film of cold air flowing through discrete holes or slots in the surface of the turbine blade to protect the outside surface of the blade from hot combustion gases. The external cooling is also called film cooling.

The internal cooling is based on the flow of cold air extracted from the compressor of the engine through channel casted inside the turbine. The cooling system is based on the use of convective cooling at the leading edge region and film cooling

through the gill holes, augmented convective cooling with rib turbulators in the mid-chord region, and squealer tip-cap cooling and augmented convective cooling with pin fins in combination with film cooling at the trailing edge.

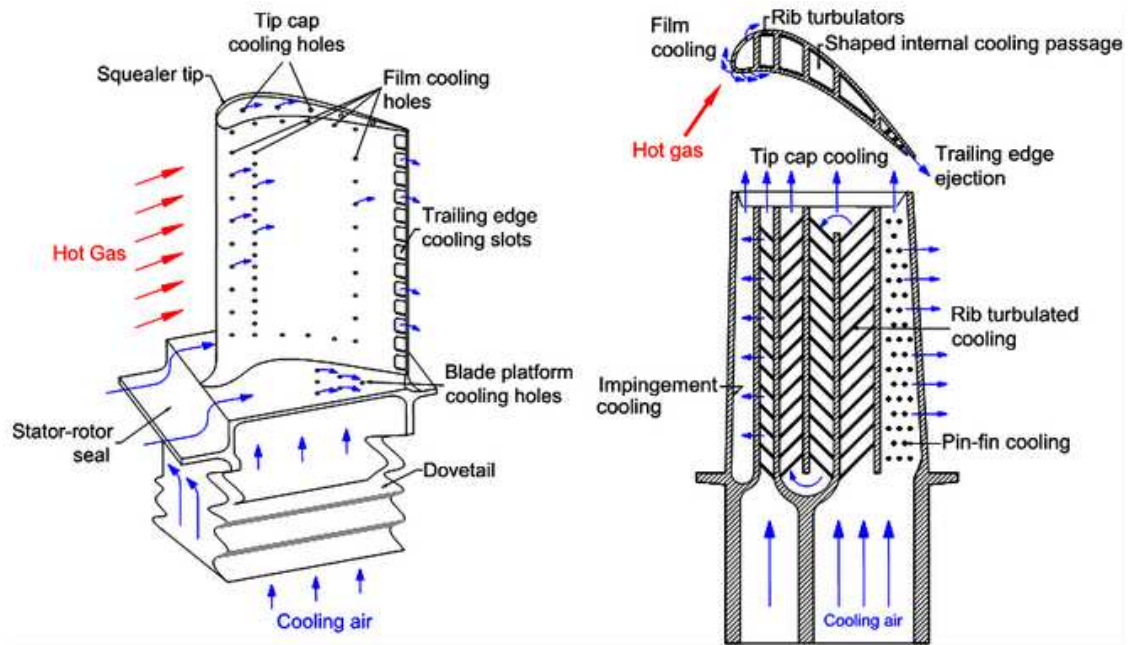


Figure 1–2: Cooling Configuration System.

Figure 1–2 was reproduce from [2].

A blade midchord region uses serpentine coolant passage with rib turbulators on the inner walls of the rotor blades, while the blade trailing-edge region uses short pins due to space limitation and structure integrations. These cooling configuration are very helpful for the convective heat transfer. The optimum combination of these cooling techniques to meet the highly complex design requirements is the key to designing air-cooled turbine blades and vanes [2]. This work is focused on the rib turbulators in the midchord region. The goal is to *find the optimal configuration of the ribs turbulators to enhance the heat transfer*.

Leonardi *et al.* (2003-2007) have carried out Direct Numerical Simulations (DNS) for transverse square bars in one wall for a fully developed turbulent channel flow. The study compares different configurations of the roughness varying the  $p/e$  ratio to achieve an improvement of the overall heat transfer from one wall to

the other. Higher heat transfer was achieved for  $p/e = 7$ . For  $p/e \geq 7$ , the flow reattaches on the bottom wall at  $4.8e$  downstream of the back face of the element. The cavity is occupied by a large recirculation region with two secondary vortices, of opposite direction to the main recirculatory zone. The distribution of  $C_f$  and  $P$  in conjunction with the mean streamlines, indicate that, for  $p/e > 7$ , the roughness elements are isolated since the strength and size of the main recirculation zone no longer depend on  $p/e$ . The minimum  $C_f$  and maximum  $P_d$  occur at  $p/e = 7$  when the reattachment on the bottom wall occurs immediately upstream of the subsequent element. For  $p/e \leq 2$ , the total drag is closely approximated by the skin frictional drag on the crest of the elements. In the range  $5 < p/e < 19$ , the total drag is contributed almost entirely by  $P_d$ .

Han (2004) presents some studies that demonstrate that in a non-rotating channel, the  $45^\circ$  ribs perform better than  $90^\circ$  ribs and than the smooth channel [4]. Besides, a smaller rib height is more efficient for higher Reynolds number flows, and the heat transfer enhancement decreases but pressure drop penalty increases with the Reynolds number. The experimental study of the 3D roughness have been performed by Han *et al.* (2000). This study shows that 3D roughness are more effective in the enhance of the heat transfer.

Ashrafian, Andersson, Manhart (2004) studied the pressure-driven flow in a rod-roughened channel in a  $k$ -type roughness with a pitch-to height ratio  $\lambda/e$  was observed all along the bottom of the cavity [5]. Outside the roughness sublayer, i.e. beyond  $5e$ , no discernible streamwise variation of mean velocity could be observed. Inside the roughness sublayer, however, significant differences in the turbulence field between smooth- and rough-wall layers were observed, for instance the high-energy region formed by a shear layer emanating from the crest of the roughness elements. In this study it is also observed a high level of local skin-friction coefficient  $C_f$  at the corner of the rod, and therefore the wall-friction decays with  $x$ . The form drag

is responsible for the entire resistance in the channel walls except in the crest of the rods. It is possible to observe the contribution of form drag to the total drag is much bigger than that of shear stress or viscous drag. The amounts of form and viscous contributions to the total drag were evaluated; the form drag consisted about 97% of the total drag. Another observation is that in the  $k$ -type roughness, both the height of the roughness elements and the spacing between them are crucial parameters in the study of roughness.

Orlandi & Leonardi (2006) performed DNS for turbulent channel flow with two- and three-dimensional roughness elements [6]. Results showed that the convective heat transfer in the presence of roughness elements depends on the orientation and on the shape of the elements. They also concluded that drag increases when the bars are orthogonal to the flow. With staggered cubes the flow inside the cavity is diverted from the cubes and strong ejections occur.

Leonardi, Orlandi & Antonia (2007) have carried out a DNS for passive scalar transport in a turbulent channel flow with square bars on one wall [7]. The total heat transfer depends on  $p/e$ , the pitch to height ratio of the roughness and it is maximum for  $p/e = 7$ . The temperature gradient is smallest in the inner channel and largest near walls. The total heat flux is maximum for  $p/e = 7$  the configuration for which  $v^2$  is maximum. This simulation clearly demonstrate that the roughness can be very effective in enhancing the turbulent (and total) heat transfer.

Leonardi, Orlandi, Djenidi & Antonia (2004) have performed numerical simulations of transverse square bars varying the ratio  $p/e$ , where  $e$  is the bar height and  $p$  is the longitudinal separation between consecutive bars [8]. With roughness on both walls, the velocity profile is, as expected, symmetric while, when roughness is only on the bottom wall, the maximum of  $\bar{U}$ ,  $y_{max}$ , is shifted upward. Very close to the crest plane, the roughness splits the elongated streaky structures into nearly circular regions located above the grooves. The no-slip condition on the crest reduces the

coherence in the streamwise direction and produces gradients of velocities in  $x$ . For very large values of  $p/e$  ( $p/e > 19$ ), the flow tends to that over a smooth wall and then streaky structures are expected to appear on the bottom wall. For  $p/e = 1$ , the wall-normal velocity is very weak and this is, indeed, the case closer to the smooth wall. As  $p/e$  increases, the vertical motion becomes increasingly important, and reaches its maximum intensity for  $p/e = 7$ . Near a rough wall, made up of transverse square bars, the structures are less elongated than over a smooth wall. The case with  $p/e = 7$  present a maximum outward ejections of fluid from the cavities. The dependence on  $p/e$  is very strong; for very small values of  $p/e$ , structures and turbulent intensities resemble those over a smooth wall. For  $p/e = 3$ , the effect of the wall extends up to about  $2e$  above the plane of the crest, while, for  $p/e = 7$ , the distance is as large as  $5e$ . For larger values of  $p/e$ , the normal wall motion induced by the roughness is confined to smaller regions, and the overlying flow is closer to that above a smooth wall.

Kim & Lee (2007) presented a numerical optimization procedure in which a square channel with V-Shaped rib turbulators on both walls was analyzed [1]. They found that two small vortices are initiated on surface of each rib and develop rapidly streamwise on the surface. Consequently, the whole flow field consist of four big vortices of almost the same size. Also, the heat transfer and friction coefficients are commonly sensitive to the ratio of the rib height to channel height. The heat transfer coefficient decreases abruptly just behind the rib due to flow separation, and it increases downstream to reach a maximum near the reattachment line.

Lee *et al.* (2009) present a study suggesting that introducing ribs to a coolant channel is one of the most typical methods to enhance heat transfer between solid surface and fluid flow [9]. The rib turbulators augment heat transfer in the internal coolant passages because they cause flow separations and reattachment, which result in breakage of the laminar sublayer. In addition, when the angled ribs are installed

in a channel, the heat transfer is enhanced because of secondary flow structures. For the  $45^\circ$  multiple V-Shaped rib configurations, small-scale secondary flow cells were generated at the center region, while relatively strong secondary flows developed near sidewall due to its geometric feature. Therefore, the peak values at the center region were lower than those near the sidewalls and asymmetric distributions were observed. The average heat/mass transfer channel characteristic were not affected significantly by the channel aspect ratio. This was due to the small-scale secondary flow patterns in the channel.

Toro (2010) performed Direct Numerical Simulations (DNS) on V-Shaped turbulators in order to find the configuration with the highest heat transfer [10]. He found that the V-Shaped turbulators configuration with the highest heat transfer is  $p/e = 3$  and  $e/H = 0.25$ . In his thesis he found a secondary motion generation due for the ejections in the side walls. The results found a correlations with the reduction of the secondary motion while the  $p/e$  ratio increase.

In the present work, numerical simulations will be performed to analyze heat transfer for different configurations of turbulators. The turbulators analyzed are: Square Bars, V-Shaped and Segmented V-Shaped. This geometry configurations are analyzed for several values of the ratio  $p/e$  (where  $e$  is the bar height and  $p$  is the longitudinal separation between consecutive bars). The value of  $p/e$  ratio will be 1, 3, 5, 8, 10 and 15. The Reynolds number is  $Re = 10,400$  using RANS model (Reynolds Average Navier Stokes model). The Reynolds number is  $Re = UH/\nu$ , where  $U$  is the inlet velocity and  $\nu$  is the kinematic viscosity. The kinematic viscosity is defined by  $\nu = \mu/\rho$ , where  $\mu$  is the dynamic viscosity and  $\rho$  is the density. The computational box is  $6H \times 2H \times 2H$  in the streamwise, normal and spanwise direction, respectively. Periodic boundary conditions are applied to the streamwise and spanwise direction. For the upper and lower wall a no-slip boundary condition is applied. The walls have different temperatures, the lower wall was defined like a

hot wall and the upper wall was defined like a cold wall. The mesh dimensions are  $128 \times 60 \times 64$  in the streamwise, normal, and spanwise distance respectively. In the normal direction a non uniform grid was used, with 30 points in the center of the channel and 15 points in the cavity region.

## CHAPTER 2 JUSTIFICATION

The gas turbine engines are designed to withstand high temperatures while in operation. Propulsion efficiency is proportional to the fluid temperature at the combustion chamber. By increasing the temperature of the fluid, efficiency increase but the turbine risk damage by employing. Sophisticated cooling technique (Figure 2-1 left) increase the heat transfers in the blade [11] to avoid damage and increase durability of the turbine (Figure 2-1 right). The purpose of this research is find the best configuration of the rib turbulators to enhance the heat transfer and increases the thermal efficiency.

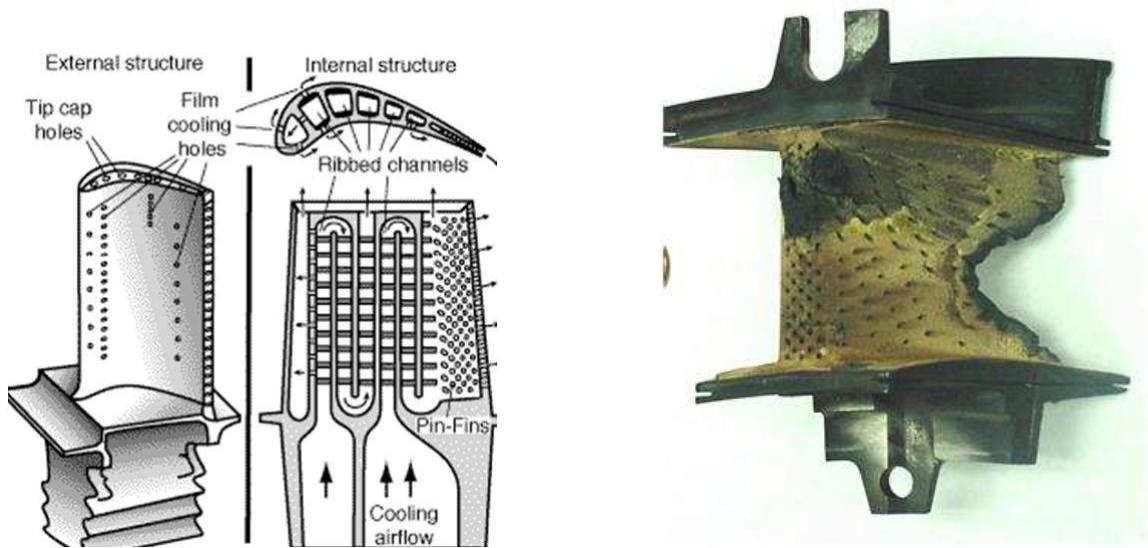


Figure 2-1: Left: Cooling Configuration System. Right: Example of a Damage Turbine Blade

Figure 2-1 (Left) was reproduce from [2].

## CHAPTER 3

# NUMERICAL METHOD

To study the heat transfer in a channel with roughness on the wall have to solve numerically the governing equations: Mass Conservation, Conservation of Momentum, and Conservation of Energy.

### 3.1 Governing Equation

The equation of conservation of mass, or continuity equation, can be written as follows:

$$\frac{\partial \rho}{\partial t} + \nabla \cdot (\rho u) = 0 \quad (3.1)$$

where  $\rho$  is the density of the air and  $u$  is the instantaneous velocity vector. With the assumptions of incompressible flow and steady state, the equation (3.1) can be reduced to

$$\nabla \cdot u = 0 \quad (3.2)$$

The conservation of momentum equation in an inertial (non-accelerating) reference frame is described in the next equation

$$\frac{\partial}{\partial t}(\rho u) + \nabla \cdot (\rho u u) = -\nabla p + \nabla \cdot (\bar{\sigma}) + \rho g \quad (3.3)$$

where  $p$  is the static pressure,  $\bar{\sigma}$  is the stress tensor, and the  $\rho g$  is the gravitational body force. Using the steady state condition and neglecting gravitational body force the equation (3.3) becomes

$$\nabla \cdot (\rho u u) = -\nabla p + \nabla \cdot (\bar{\sigma}) \quad (3.4)$$

The stress tensor  $\bar{\sigma}$  is given by

$$(\bar{\sigma}) = \mu \left[ (\nabla u + \nabla u^T) - \frac{2}{3} \nabla \cdot (uI) \right] \quad (3.5)$$

where  $\mu$  is the molecular viscosity,  $I$  is the unit tensor, and the second term on the right hand side is the effect volume dilation.

The conservation of energy it is derived from the first law of thermodynamics applied to the rate of change in total energy in the fluid. This equation can be expressed by

$$\frac{\partial}{\partial t}(\rho E) + \nabla \cdot (\rho U E) = -\nabla \cdot (pU) - \nabla \cdot q + \nabla \cdot (U\bar{\sigma}) \quad (3.6)$$

where  $E = \frac{1}{2}u_k u_k$  and the term of the Fourier's Law for heat conduction is

$$q_j = k \frac{\partial T}{\partial x_j}$$

Applying the steady state condition to the equation (3.6) it is obtain

$$\nabla \cdot (\rho U E) = -\nabla \cdot (pU) - \nabla \cdot q + \nabla \cdot (U\bar{\sigma}) \quad (3.7)$$

With these three equations it is possible model to the behavior of a fluid.

## 3.2 Mesh generation (Gambit)

The first step is to create a 3D square duct in GAMBIT. GAMBIT is a Fluent's geometry and mesh generation software. The computational box used is  $6H \times 2H \times 2H$  in which  $x$  is the streamwise direction,  $y$  is the normal direction and  $z$  is the spanwise direction. The square channel has roughness in the upper and lower wall, and this will be analyzed in aligned and staggered position. The boundary conditions

for the upper and lower walls are no-slip conditions. Periodic boundary conditions are applied for the streamwise and spanwise direction. The mesh dimensions are  $128 \times 60 \times 64$  in the streamwise, normal, and spanwise distance respectively. In the normal direction the cavity region will be meshed with 15 points. The center of the channel, the portion outside of the roughness layer, will have 30 points with clustering at the crest plane region to model more accurately the boundary layer. In the process to generate the mesh, a quadrilateral/hexahedral (Quad/Hex) grid is used. The Quad/Hex mesh is used instead of the Triangle/Tetrahedral (Tri/Tet) mesh because it does not cause numerical problems by skewness and the faces are automatically aligned with the flow so a false diffusion is not generate. The Tri/Tet mesh can reduce the accuracy of the problem it is inefficient therefore more mesh points are needed compared to a hexahedral mesh. The Figure 3–1 shows an example of the mesh used in this work. This Quad/Hex mesh is aligned to the flow, that is very efficient because the flow will be modeled with more precision.

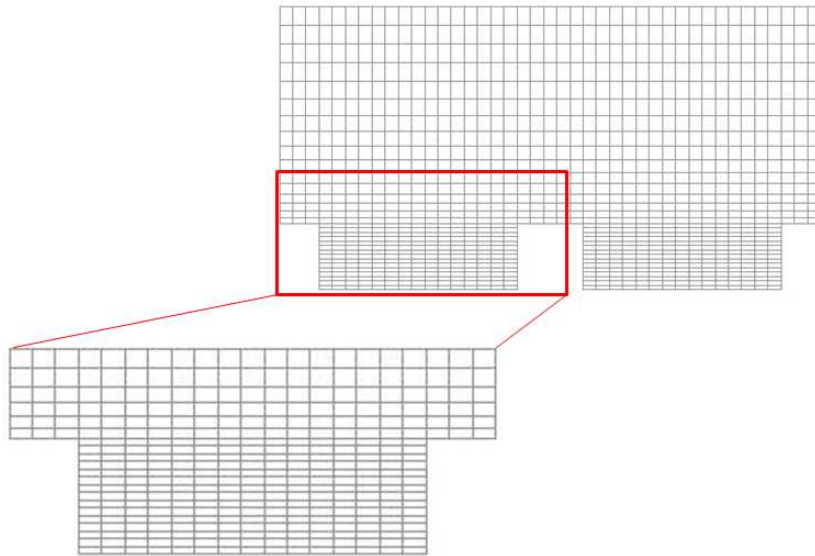


**Figure 3–1: Quadrilateral/Hexahedral (Quad/Hex) Mesh.**

An example of the Tri/Tet mesh is shown in the Fig. 3–2. It is possible to observe in this figure that the Tri/Tet mesh is an irregular mesh and does not follow

any pattern. This mesh is not aligned with the flow, that's mean that the simulation has larger truncation errors. That is the reason to not select this type of mesh.

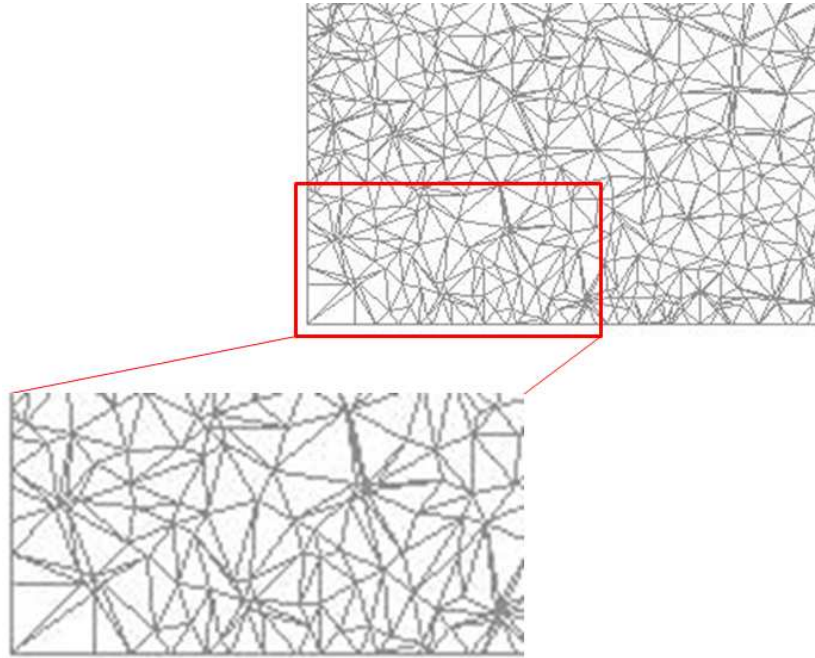


**Figure 3–2: Triangle/Tetrahedral (Tri/Tet) Mesh.**

### 3.3 Numerical Solution of Governing Equations (Fluent)

FLUENT is a software capable of solving Navier Stokes and energy equations. The different cases in this study will be have approximately 80,000 iterations. For the continuity and momentum equation a residual below  $1 \times 10^{-3}$  will be desired. For the energy equation and the components of the  $k - \epsilon$  a residual value below  $1 \times 10^{-8}$  is wanted. For a steady state condition FLUENT solves the energy equation in the following form:

$$\nabla \cdot (\rho U E) = - \nabla \cdot (pU) + \nabla \cdot (k_{eff} \nabla T) - \nabla \cdot \left( \sum_j h_j J_j \right) + \nabla \cdot (\bar{\tau}_{eff} \cdot U) \quad (3.8)$$

where  $k_{eff}$  is the effective conductivity ( $k + k_t$ , where  $k_t$  is the turbulent thermal conductivity, and this is defined by the turbulence model used in this analysis),

and  $\vec{J}_j$  is the diffusion flux of the species  $j$ . The first three terms on the right-hand side on the Equation (3.8) represent energy heat transfer due to conduction, species diffusion, and viscous dissipation, respectively. The term of  $E$  is described in the next equation

$$E = h - \frac{p}{\rho} + \frac{v^2}{2} \quad (3.9)$$

where for incompressible flow the enthalpy  $h$  is defined as

$$h = \sum_j Y_j h_j + \frac{p}{\rho} \quad (3.10)$$

Now the term  $E$  for the Equation (3.11) is defined as

$$E = \sum_j Y_j h_j + \frac{v^2}{2} \quad (3.11)$$

The factor  $Y_j$  in the equation (3.10) is the mass fraction species  $j$  and

$$h_j = \int_{T_{ref}}^T c_{p,j} dT \quad (3.12)$$

where  $T_{ref}$  is the reference temperature used in the analysis.

## Spatial Discretization

For the Mass Conservation, Momentum Conservation and Energy Conservation the first order upwind scheme is used until results converge. A second order upwind scheme is further used to have more accurate results.

### 3.3.1 Problem Setup

A steady state model is used with the Pressure-Based Solver. This segregated algorithm has proven to be robust and versatile and has been utilized in concert with a wide range of physical models, including multiphase flows, conjugate heat transfer and combustion. In the segregated pressure-based solver, each equation

is solved separately [12]. The continuity equation takes the form of a Patankar's SIMPLE algorithm. For the turbulent model it was chosen the Reynolds-Averaged Navier-Stokes (RANS) model that solve ensemble-average (or time average) Navier-Stokes equations. Choosing the RANS models over the Large Eddy Simulation (LES) model or the Direct Numerical Simulation (DNS) model is a logical decision because LES and DNS are computationally demanding and requirements are still too large for most practical industrial applications.

### 3.4 Sub Grid Model (RANS)

To solve the turbulence in the flow the Navier Stokes equations are used. By averaging in time the Navier-Stokes equations it is obtain the Reynolds-Average Navier Stokes equations which are used to model the mean flow.

$$\frac{\partial \bar{u}_i}{\partial x_i} = 0 \quad (3.13)$$

$$\rho \bar{u}_j \frac{\partial \bar{u}_i}{\partial x_j} = -\frac{\partial \bar{p}}{\partial x_i} + \rho \frac{\partial^2 \bar{u}_i}{\partial u_j \partial u_j} + \frac{\partial}{\partial x_j} (-\overline{\rho u'_i u'_j}) \quad (3.14)$$

The Equation (3.13) and (3.14) are the Reynolds Average Navier Stokes for a steady state case (see Appendix A). The term of Reynold Stress Tensor ( $\overline{\rho u'_i u'_j}$ ) is the one that needs to be modeled because this closure problem has three velocity components, one pressure component and six Reynold stress terms (ten unknown). There are four equations from (3.13) and (3.14). For this reason a turbulent model is needed to solve this six unknowns. Several models are used in literature, the two most used models are two equations models:  $k - \epsilon$  and  $k - \omega$ . The model which was decided to be use is the  $k - \epsilon$  model because the computational cost per iteration is less, in particular it is used the RANS model Realizable  $k - \epsilon$  (RKE) available in Fluent. The Realizable  $k - \epsilon$  model is chooses over the Standard  $k - \epsilon$  model and the Renormalization group (RNG)  $k - \epsilon$  model because none of the other models

are realizable. The Realizable  $k - \epsilon$  offers largely the same benefits and has similar applications as RNG but it is more accurate and easier to converge than RNG. The modeled transport equations for  $k$  and  $\epsilon$  in the realizable  $k - \epsilon$  model are

$$\frac{\partial}{\partial t}(\rho k) + \frac{\partial}{\partial x_j}(\rho k u_j) = \frac{\partial}{\partial x_j} \left[ \left( \mu + \frac{\mu_t}{\sigma_k} \right) \frac{\partial k}{\partial x_j} \right] + G_k + G_b - \rho \epsilon - Y_M + S_k \quad (3.15)$$

and

$$\frac{\partial}{\partial t}(\rho \epsilon) + \frac{\partial}{\partial x_j}(\rho \epsilon u_j) = \frac{\partial}{\partial x_j} \left[ \left( \mu + \frac{\mu_t}{\sigma_\epsilon} \right) \frac{\partial \epsilon}{\partial x_j} \right] + \rho C_1 S_\epsilon - \rho C_2 \frac{\epsilon^2}{k + \sqrt{\nu \epsilon}} + C_{1\epsilon} \frac{\epsilon}{k} C_{3\epsilon} G_b + S_\epsilon \quad (3.16)$$

where

$$C_1 = \max \left[ 0.43, \frac{\eta}{\eta + 5} \right] \quad \eta = S \frac{k}{\epsilon} \quad S = \sqrt{2 S_{ij} S_{ij}}$$

In the equations (3.15) and (3.16),  $G_k$  represents the generation of the turbulent kinetic energy due to the mean velocity gradients and  $G_b$  is the generation of the turbulent kinetic energy due to buoyancy (this term is neglected because the buoyancy is not considered in this work). The equation that describe the variable  $G_k$  is

$$G_k = -\rho \overline{u'_i u'_j} \frac{\partial u_j}{\partial x_i}$$

The variable  $Y_M$  from equation (3.15) represents the contribution of the fluctuating dilatation in compressible turbulence to the overall dissipation rate. This term is also neglected because the fluid was assumed incompressible

For a steady state simulation and eliminating the term that does not apply to this work the following equations for the realizable  $k - \epsilon$  model are

$$\frac{\partial}{\partial x_j}(\rho k u_j) = \frac{\partial}{\partial x_j} \left[ \left( \mu + \frac{\mu_t}{\sigma_k} \right) \frac{\partial k}{\partial x_j} \right] + G_k - \rho \epsilon \quad (3.17)$$

and

$$\frac{\partial}{\partial x_j}(\rho \epsilon u_j) = \frac{\partial}{\partial x_j} \left[ \left( \mu + \frac{\mu_t}{\sigma_\epsilon} \right) \frac{\partial \epsilon}{\partial x_j} \right] + \rho C_1 S_\epsilon - \rho C_2 \frac{\epsilon^2}{k + \sqrt{\nu \epsilon}} \quad (3.18)$$

The eddy viscosity is computed from

$$\mu_t = \rho C_\mu \frac{k^2}{\epsilon}$$

$C_\mu$  is not a constant and it is computed from

$$C_\mu = \frac{1}{A_0 + A_s \frac{kU^*}{\epsilon}}$$

where

$$U^* \equiv \sqrt{S_{ij}S_{ij} + \tilde{\Omega}_{ij}\tilde{\Omega}_{ij}}$$

and

$$\tilde{\Omega}_{ij} = \overline{\Omega_{ij}} - \epsilon_{ijk}\omega_k$$

where  $\overline{\Omega_{ij}}$  is the mean rate-of-rotation tensor viewed in a rotation reference frame with the angular velocity  $\omega_k$ . The model constant  $A_0$  and  $A_s$  are given by

$$A_0 = 4.04 \quad A_s = \sqrt{6}\cos\phi$$

where

$$\begin{aligned} \phi &= \frac{1}{3}\cos^{-1}(\sqrt{6}W) \\ W &= \frac{S_{ij}S_{jk}S_{ki}}{\tilde{S}^3} \\ \tilde{S} &= \sqrt{S_{ij}S_{ij}} \\ S_{ij} &= \frac{1}{2} \left( \frac{\partial u_j}{\partial x_i} + \frac{\partial u_i}{\partial x_j} \right) \end{aligned}$$

The model constant  $C_{1\epsilon}$ ,  $C_2$ ,  $\sigma_k$ , and  $\sigma_\epsilon$  have been established to ensure that the model performs well certain canonical flows. The model constant are

$$C_{1\epsilon} = 1.44 \quad C_2 = 1.9 \quad \sigma_k = 1.0 \quad \sigma_\epsilon = 1.2$$

### 3.5 Boundary Conditions

- **Thermal Boundary Conditions at Wall**

When the energy equation is solved, different thermal boundary conditions at the wall boundary can be assigned: fixed heat flux or fixed temperature. In this present study the temperature is imposed at the wall. The lower wall is  $T_1 = 900$  K and the upper  $T_2 = 300$  K therefore the heat is transported away from the lower wall and dissipated on the upper wall. The heat flux at the wall is computed as

$$q = h_f(T_w - T_f) \quad (3.19)$$

where

$h_f$  = fluid-side local heat transfer coefficient.

$T_w$  = wall surface temperature.

$T_f$  = local fluid temperature.

- **Wall Motion and Shear Condition**

Wall boundaries can be either stationary or moving. In this case the walls do not move and the no-slip condition applies.

- **Periodic Condition**

Periodic boundary conditions are used when the flows across two opposite planes in the computational model are identical, such in ours. The inlet and outlet of the channel are the same and periodicity is applicable [13]. For the boundary condition is choose a specific mass flow rate of  $0.208 \text{ Kg/s}$  that depends of the Reynolds number. The flow direction is parallel to the streamwise direction. A upstream bulk temperature is calculate for the periodic zone, this will be the average temperature between the lower and upper wall. The bulk temperature is 300 K.

### 3.6 Initial Condition

To solve the Navier-Stokes equations an initial condition is needed. The closer is the initial condition to the solution, the faster the results converge. The table 3–1 has the initial input:

**Table 3–1: Initial Values to Setup Fluent**

Gauge Pressure (pascal)	0
X Velocity ( $m/s$ )	0.151916
Y Velocity ( $m/s$ )	0
Z Velocity ( $m/s$ )	0
Turbulent Kinetic Energy ( $m^2/s^2$ )	1
Turbulent Dissipation Rate ( $m^2/s^3$ )	1
Temperature (K)	300

The Full Multigrid initialization (FMG initialization) can be used to create better initialization of the flow fluid field and can provide an initial and approximate solution at a minimum cost to the overall computational expense. The equations are solved with first-order accuracy on the coarse-level meshes. FMG uses the Full Approximation Storage (FAS) multigrid method to solve the flow problem on a sequence of coarse meshes, before transferring the solution onto the actual mesh. In the process of the case initialization a process of reordering the domain and zone is completed, to do this FLUENT used the reverse Cuthill-McKee algorithm. The algorithm reorder the zones, cell and faces, and gives a bandwidth reduction of the grid partition.

After all the process describe before it is possible to start with the iteration until that the solution converge. Afterwards it is possible to start with the post-processing and obtain the quantities of interest.

### 3.7 Reference Values

The table 3–2 shows the reference values used:

Table 3–2: Reference Values Used in Fluent

Area ( $m^2$ )	1
Density ( $kg/m^3$ )	1.225
Enthalpy ( $J/Kg$ )	0
Length (m)	1
Pressure (pascal)	0
Temperature (K)	288.16
Velocity ( $m/s$ )	1
Viscosity ( $Kg/m - s$ )	$1.7894e^{-05}$
Ratio of Specific Heat	1.4

## Evaluation of Gradients

Gradients are needed not only for constructing values of a scalar at the cell faces, but also for computing secondary diffusion terms and velocity derivatives. The gradient  $\Delta\phi$  of a given variable  $\phi$  is used to discretized the convection and diffusion terms in the flow conservation equations. In this situation the gradient used is the Green-Gauss Node-Based method. When the Green-Gauss theorem is used to compute the gradient of the scalar  $\phi$  at the cell center  $c0$ , the discrete form is

$$(\Delta\phi)_{c0} = \frac{1}{V} \sum_f \bar{\phi}_f \vec{A}_f \quad (3.20)$$

where  $\phi_f$  is the value of  $\phi$  at the cell face centroid, computed as shown in the sections below. The summation is over all the faces enclosing the cell. The  $\bar{\phi}_f$ , in Equation (3.20) can be computed by the arithmetic average of the nodal values on the face.

$$\bar{\phi}_f = \frac{1}{N_f} \sum_i^{N_f} \bar{\phi}_n$$

where  $N_f$  is the number of nodes on the face. The nodal values,  $\bar{\phi}_n$  are constructed from the weighted average of the cell values surrounding the nodes. This

scheme reconstructs exact values of a linear function at a node from surrounding cell-centered values on arbitrary unstructured meshes by solving a constrained minimization problem, preserving a second-order spatial accuracy. The node-based averaging scheme is known to be more accurate than the default cell-based scheme for unstructured meshes, most notably for triangular and tetrahedral meshes.

## CHAPTER 4

# SMOOTH CHANNEL

Before studying the flow in a turbulent rough channel, it is important to know the behavior of the flow in the most simple situation. A smooth channel presents the simplest case in which the flow and validity of the code can be studied.

A numerical simulation for a smooth channel was performed. Figure 4–1 shows the configuration of a smooth channel. The computational box is  $6H \times 2H \times 2H$  in the streamwise, normal and spanwise direction, respectively. The boundary conditions are periodic in x and z direction and no-slip condition in the wall normal direction. The grid dimensions are  $128 \times 60 \times 64$  in the streamwise, normal, and spanwise distance respectively.

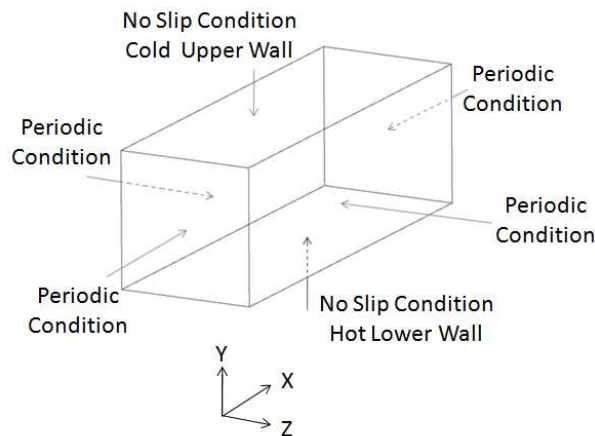


**Figure 4–1: Smooth Channel Configuration**

Figure 4–2 shows the streamwise average velocity profile along the normal direction for the RANS and DNS simulation. The average velocity for the RANS is normalized by the bulk velocity ( $u_{Bulk} = 0.151916m/s$ ).

It is possible to see that at the walls the average velocity is zero for the no-slip conditions applied before. The average velocity in the streamwise direction has the highest value at the center of the channel ( $y^* = 0$ ). The plot shows that the results of the two simulations agree well.

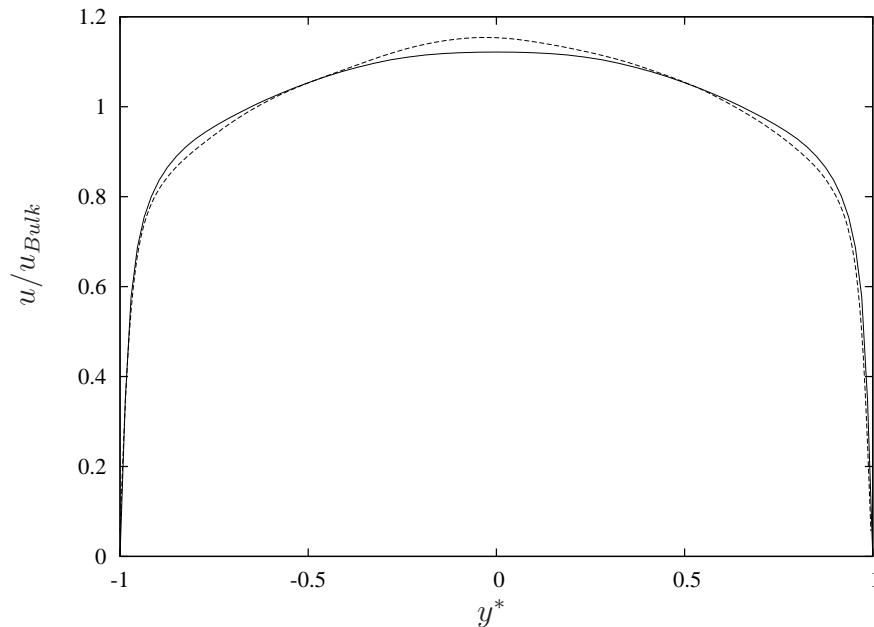


**Figure 4-2: Streamwise Average Velocity Profile of a Channel Flow.** (—) DNS and (----) RANS

The Figure 4-3 shows an average velocity contour of the smooth channel for the RANS simulations to understand better physical behavior of the flow velocity along the channel. The highest average velocity is represented by red color and the lowest by blue color. The middle of the channel present the highest average velocity (like is present in the Figure 4-2), for that reason the highest red color contour is present in this area. In the different two wall, the blue color is present showing the exist the no-slip boundary condition.

Another important component in the analysis of a turbulent channel flow is the distribution of the temperature along the channel. The dimensionless temperature  $\tilde{T}$  is defined by the next equation:

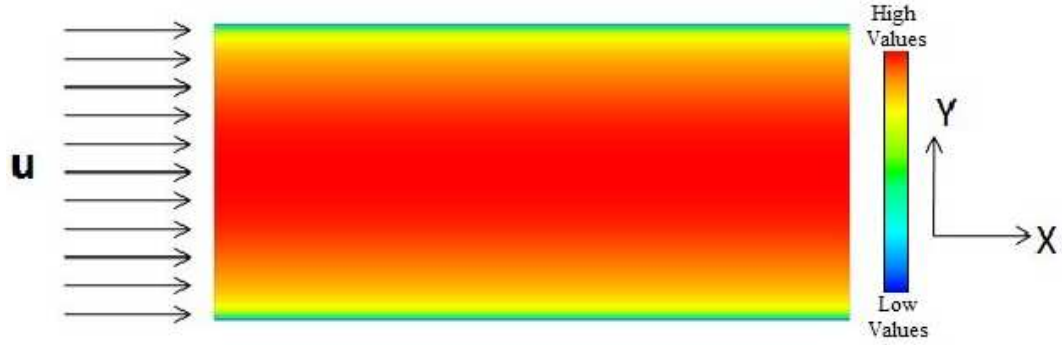


Figure 4-3: Average Velocity Contour in the Streamwise Direction.

$$\tilde{T} = \frac{T - T_{Bulk}}{T_{Wall} - T_{Bulk}} \quad (4.1)$$

where  $T$  represents the static temperature,  $T_{Bulk}$  is the bulk temperature ( $T_{Bulk} = 300$ ), and  $T_{Wall}$  is the wall temperature. The dimensionless temperature ranges from  $-1$  to  $1$ .

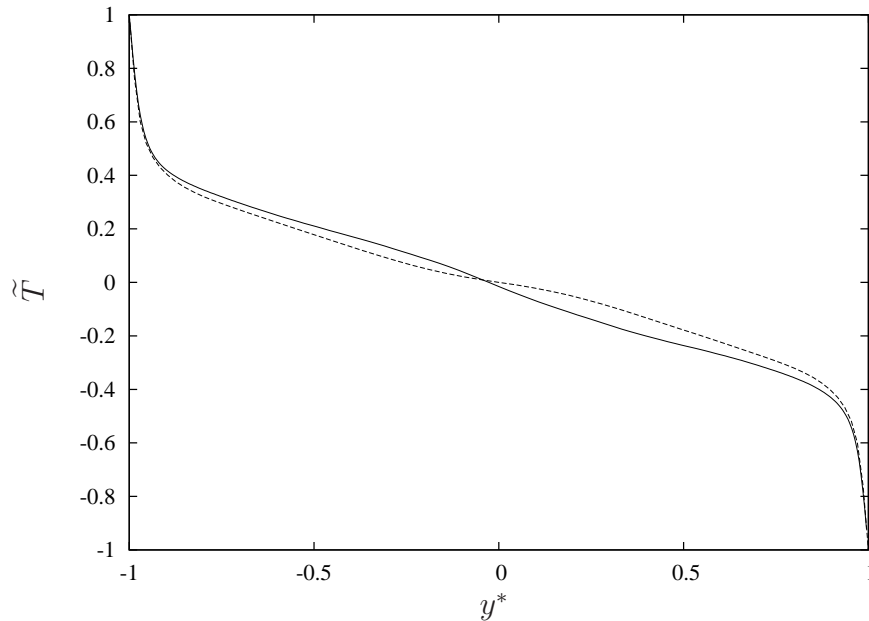


Figure 4-4: Temperature Profile of a Channel Flow. (—) DNS and (----) RANS

Figure 4-4 shows the distribution of the non-dimensional temperature along the normal direction of the channel for the RANS and DNS simulations. For the bottom wall ( $y^* = -1$ ) the temperature has the highest value of the temperature  $\tilde{T} = 1$  because this wall represent the hot wall. For the top wall ( $y^* = +1$ ) the

temperature of the channel is  $\tilde{T} = -1$  because this wall represent the cold wall. The temperature profiles for the two simulations have a similar pattern.

The Nusselt number (Nu) is a parameter that provides a measure of the heat transfer occurring at the surface of the channel. The Nu is defined by the difference of non-dimensional temperature with the difference of the non-dimensional distance at the surface. The following equation shows how is calculate the Nusselt number

$$Nu = \frac{hL}{k} = \left. \frac{\partial \tilde{T}}{\partial y^*} \right|_{y^*=-1} \quad (4.2)$$

where  $h$  is the heat transfer coefficient,  $L$  is the length of the channel in the streamwise direction and  $k$  is the molecular thermal conductivity.  $\tilde{T}$  is the non-dimensional temperature and  $y^*$  is the non-dimensional normal direction. Nusselt number (Nu) of the smooth channel is  $Nu = 21.82$ .

Another important information is needed to analyze the behavior of the flow in a turbulent channel, the drag force affecting the flow in the channel. The different drag force acting in the channel are: skin frictional ( $C_f$ ), form drag ( $P_d$ ) and total drag ( $C_f + P_d$ ) that is the sum of the skin frictional and the form drag.

The skin friction arises from the interaction due between the fluid and the surface of the channel. The skin friction coefficient is a non-dimensional parameter defined mainly by wall shear stress. The following equation is used to calculate the skin friction coefficient

$$C_f = \frac{\tau_w}{\frac{1}{2}\rho v^2} \quad (4.3)$$

where  $\tau_w$  is the wall shear stress, and  $\rho$  and  $v$  are the density and velocity of the fluid. In the smooth channel, the skin frictional drag coefficient is 0.005104.

The form drag is due to the pressure on the walls perpendicular to the flow direction. Since the smooth channel does not present obstacles perpendicular to the

flow, the form drag is zero. The non-dimensional parameter of the form drag is the drag coefficient that is defined for the next equation

$$C_d = \frac{\Delta P}{\frac{1}{2}\rho v^2} \quad (4.4)$$

The form drag is calculate projecting the pressure force onto the streamwise direction. The total drag is the summation of both component, the skin friction coefficient and the form drag.

Some studies demonstrate that the use of roughness in the walls help to enhance the heat transfer between the walls (Han *et al.* 2000). The next cases analysis different type of roughness to find the best configuration that enhance the heat transfer in the channel.

## CHAPTER 5

# SQUARE BARS TURBULATORS

Perhaps the most common rough surface studied experimentally and numerically, is the case of square bars turbulators [6] [7] [8] [14]. Leonardi *et al.* (2007) performed a direct numerical simulation of the flow in a channel with transverse square bars. They found that for  $p/e = 7$  a higher heat transfer occurs.

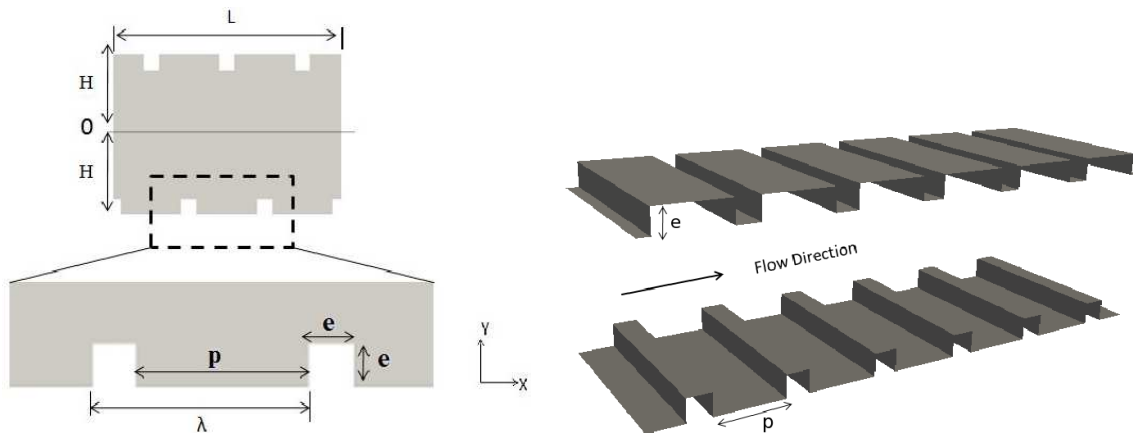


**Figure 5–1: Left: Square Bars Turbulators Sketch. Right: 3-D Square Bars Turbulators Configuration.**

In this thesis the same geometrical configuration was studied by carrying out Reynolds Average Navier Stokes (RANS). RANS models the small scales so the results are an approximation with respect to DNS. It is interesting to see the error done by RANS compared to DNS.

A numerical simulation has been performed to observe the development of the flow in a turbulent channel with square bars Turbulators and find the better configuration with the highest heat transfer. These simulation have been performed to a turbulent channel flow with roughness in the upper and lower wall in the aligned

and staggered positions. The upper wall represent a cold wall and the lower wall represent a hot wall. The two walls have a no-slip condition while periodic boundary conditions apply in streamwise and spanwise direction. Several values of  $p/e$  have been performed ( $p/e = 1, 3, 5, 8, 10$  and  $15$ , where  $k$  is the bar height and  $w$  is the longitudinal separation between consecutive bars). Figure 5–1 shows a sketch of the geometry of the Square Bars turbulators in the turbulent channel for  $p/e = 3$ .

## 5.1 Mean Flow

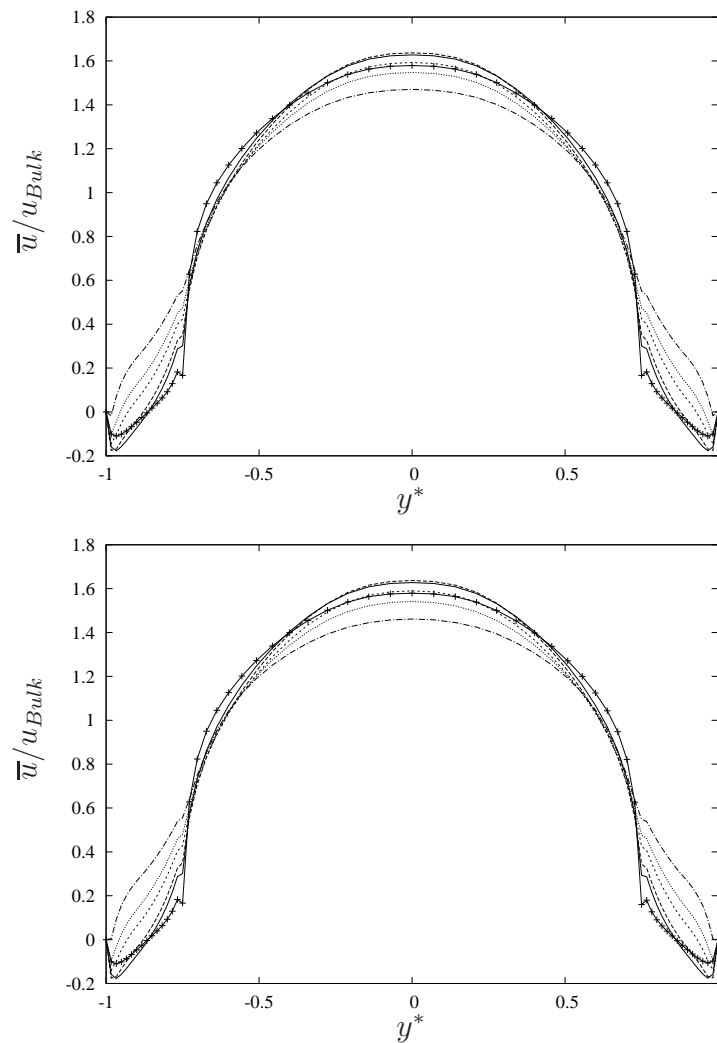


**Figure 5–2: Streamwise Average Velocity profile distribution for Square Bars turbulators. Upper: Aligned, Lower: Staggered.**

(+)  $p/e = 1$ , (—)  $p/e = 3$ , (----)  $p/e = 5$ , (-·-·-)  $p/e = 8$ , (···)  $p/e = 10$ , (---)  $p/e = 15$

Figure 5–2 shows the streamwise average velocity distribution in the normal wall direction for the aligned and staggered configuration. It is observed that the average velocity reaches a maximum at the center of the channel ( $y^* = 0$ ) and a minimum in the cavities ( $y^* = -1 : -0.75$  and  $y^* = 0.75 : 1$ ). In the cavities area the average velocity reaches negative values, due to the fluid recirculation occurring in the area between the turbulators. The cases of  $p/e = 3$  and  $p/e = 5$  are the cases with the higher negative averaged velocity values.

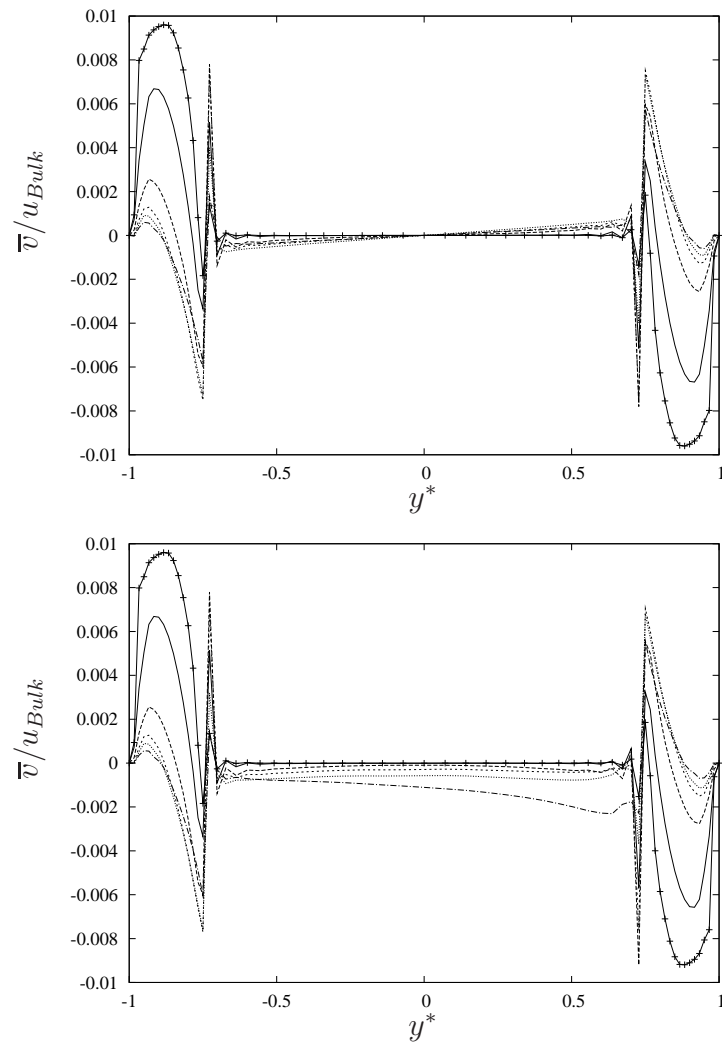


**Figure 5–3: Normal Average Velocity profile distribution for Square Bars turbulators. Upper: Aligned, Lower: Staggered.**

(+)  $p/e = 1$ , (—)  $p/e = 3$ , (----)  $p/e = 5$ , (-·-·-)  $p/e = 8$ , (···)  $p/e = 10$ , (---)  $p/e = 15$

In the Figure 5–3 the normal wall velocity averaged in  $x,z$  is shown for the aligned and staggered configuration. The normal average velocity in the mid-channel is near to zero because of symmetry. In the roughness layers ( $y^* < -0.75$  and  $y^* > 0.75$ ) the averaged velocity has the same magnitude values with opposite sign. The normal wall velocity is maximum for  $p/e = 1$  and minimum for  $p/e = 15$ .

Velocity vectors are shown in side views in the Figure 5–4. The reattachment of the flow on the bottom wall occurs for  $p/e = 8$ . For  $p/e > 8$  the flow reattaches on the bottom wall (see Leonardi *et al.* 2003). The flow moves parallel to the bottom wall and has a positive friction from the reattachment point to the next downstream turbulator. When the reattachment increase, a streamwise average velocity increases in the cavity (see Figure 5–2).

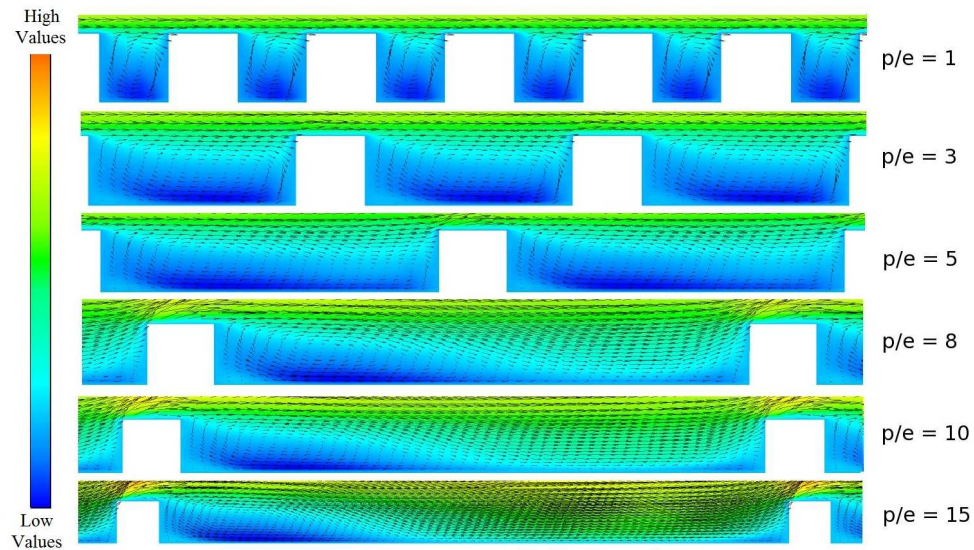


**Figure 5–4: Side view of average velocity vectors in a contour of average velocity of the streamwise direction for Square Bars turbulators.**

The Figure 5–5 shows the streamtracer along a channel with square bars turbulators in the streamwise direction (the figure only shows the lower wall of the channel with square bars turbulators). In the cavity it is possible observe the recirculation in the trailing edge of the turbulators and the reattachment of the flow on the bottom wall as mentioned before.

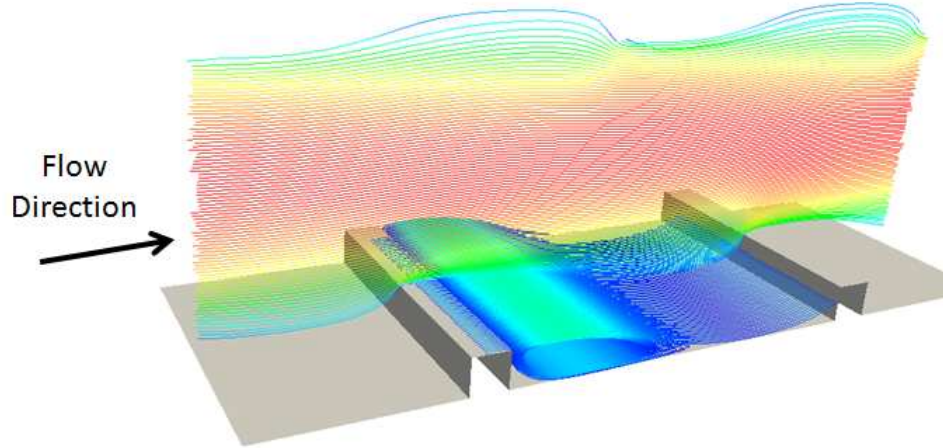


**Figure 5–5: Velocity Streamtracer in the Streamwise Direction for Square Bars turbulators.**

## 5.2 Velocity Root Mean Square (RMS)

The velocities Root Mean Square are calculate for the different configurations (Aligned and Staggered) and for the different  $p/e$  ratio. Since we performed a RANS simulation, the time dependence is modeled, and RMS refers to a spacial variation of the velocity. If the mean velocity is

$$\overline{U(y)} = \sum_{i,k} U_{i,j,k} \quad (5.1)$$

the RMS of the velocity is

$$RMS_U(y) = \sqrt{\sum_{i,k} (U_{i,j,k} - \overline{U(y)})^2} \quad (5.2)$$

The definition of the Equation 5.2 is also referred to a dispersive stress. The RMS velocity shows how much the velocity varies in the plane (x,z) with respect to the mean value.

In Figure 5–6 the streamwise velocity RMS is shown. The velocity RMS in the interior of the channel is constant and it has the lowest value for  $p/e = 1$ . In fact for square cavities ( $p/e = 1$ ) the flow skims the roughness (see Leonardi *et al.* (2004), Djenidi *et al.* (2003) while the  $p/e$  ratio increases, the velocity RMS in the channel

interior and in the crest plane ( $y^* \approx \pm 0.75$ ) increases. The average velocity is zero on the crest plane of the rib turbulators for the no-slip condition and this cause a higher velocity RMS due to the velocity gradients in x. In the cavity region, the average velocity is not zero and then the velocity RMS at this location is very high.

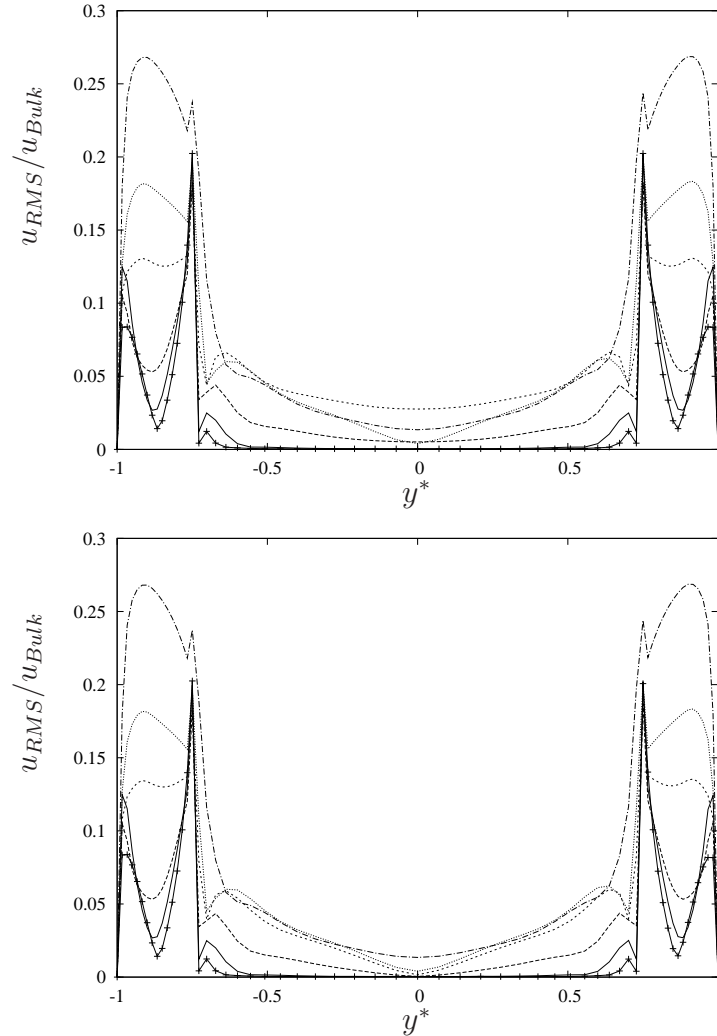


**Figure 5–6: Streamwise Velocity RMS average in time for Square Bars turbulators. Upper: Aligned, Lower: Staggered.**

(+)  $p/e = 1$ , (—)  $p/e = 3$ , (---)  $p/e = 5$ , (-·-·-)  $p/e = 8$ , (···)  $p/e = 10$ , (----)  $p/e = 15$

For the velocity RMS in the normal direction (Fig. 5–7) a maximum RMS value is shown in the area of crest plane of the turbulators ( $y^* = \pm 0.75$ ). The maximum values in this area are due to the ejections occurring at the leading edge of the turbulators. While the  $p/e$  ratio increases, the RMS of streamwise velocity for

the area around the center of the channel increases too (see Fig. 5–6). The aligned and staggered cases of the square bars turbulators are compared for the normal velocity RMS and it is possible observed that there is a smaller the difference in the channel interior for both cases. The streamwise average velocity for the aligned and staggered cases in the channel interior has a value very close to the bulk velocity (see Fig. 5–6) and that is the reason why the RMS normal velocity for these cases has the smaller magnitude values.

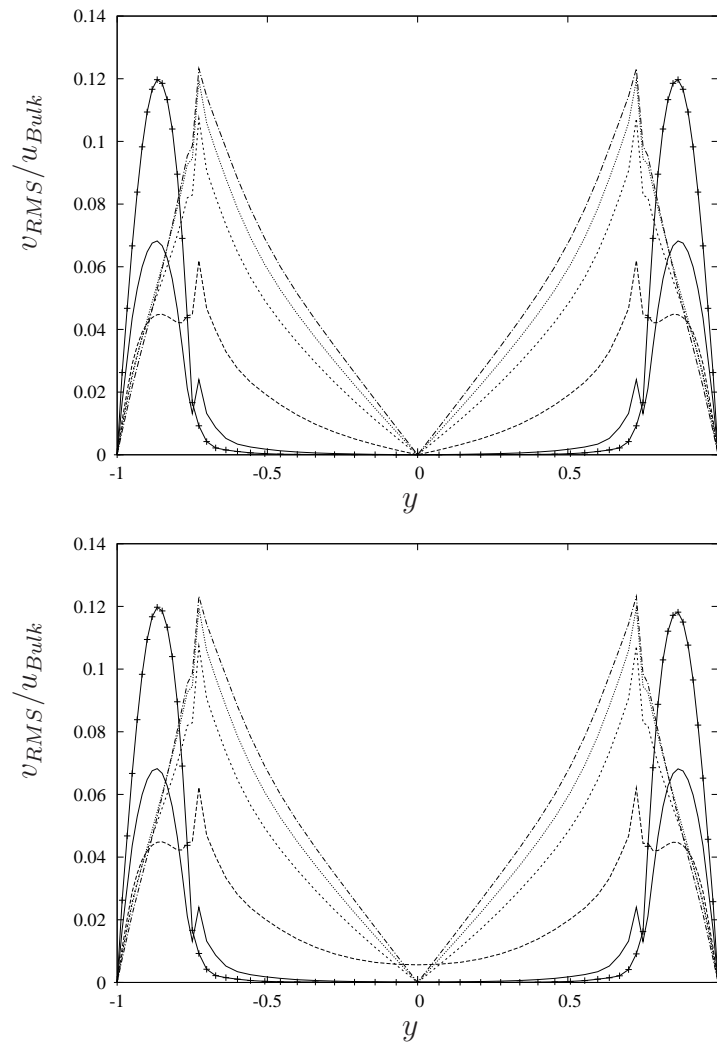


**Figure 5–7: Normal Velocity RMS average in time for Square Bars turbulators. Upper: Aligned, Lower: Staggered.**

(+)  $p/e = 1$ , (—)  $p/e = 3$ , (----)  $p/e = 5$ , (-·-·-)  $p/e = 8$ , (···)  $p/e = 10$ , (---)  $p/e = 15$

The velocity RMS in the spanwise direction are very small because the flow is approximately 2D.

### 5.3 Mean Temperature

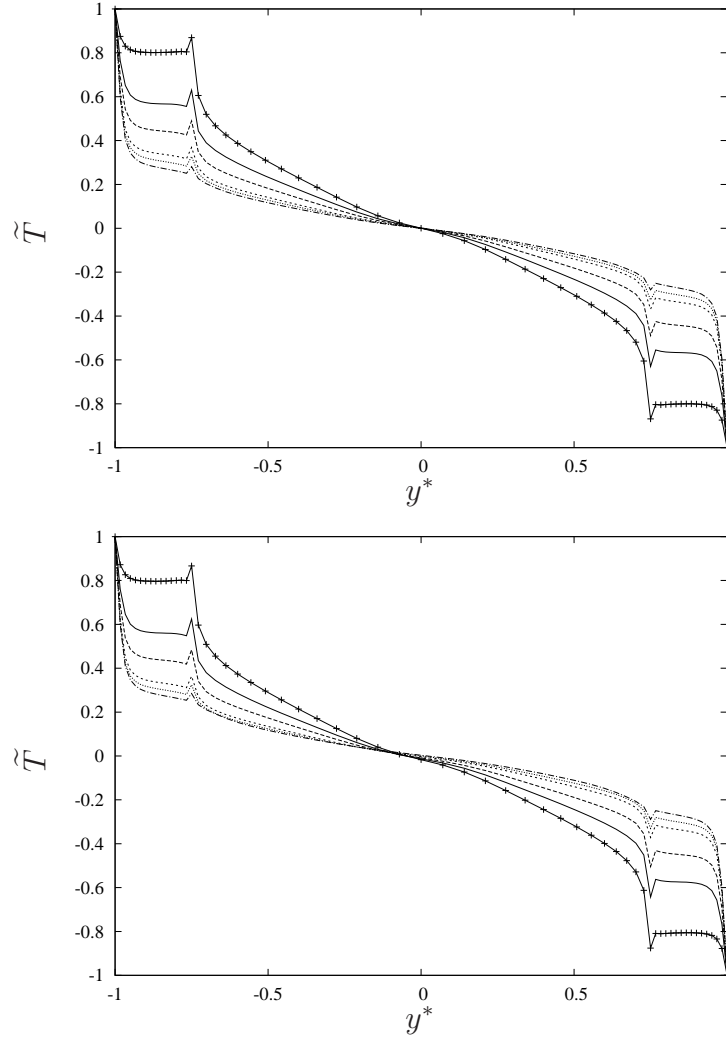


**Figure 5–8: Temperature profile distribution for Square Bars turbulators. Upper: Aligned, Lower: Staggered.**

(+)  $p/e = 1$ , (—)  $p/e = 3$ , (----)  $p/e = 5$ , (-·-·-)  $p/e = 8$ , (···)  $p/e = 10$ , (- - -)  $p/e = 15$

The Fig. 5–8 shows the distribution of the dimensionless temperature profile along the normal direction in the channel. The boundary condition for the lower wall is  $\tilde{T} = +1$  (hot wall). The boundary condition for the upper wall is  $\tilde{T} = -1$  (cold wall). These boundary condition are used to obtain the heat transfer between the walls. The Fig. 5–8 shows the development of the temperature between the

upper and the lower wall. Also shows how the square bars turbulators affect the temperature profile. There is no difference between the aligned and staggered layout of the square bars turbulators and that is because the figure shows the average in space of the different configurations. Both configurations have a constant temperature distribution in the cavity and a linear distribution of the temperature in the inner part of the channel.

By increasing  $p/e$  the temperature gradient at the wall increases and the gradient in the inner part of the channel decreases. In fact, near the wall the conduction dominates over the turbulent heat flux. The opposite happens at the center of the channel. So when  $p/e$  increases, the temperature gradient at the wall and the turbulent heat flux  $\langle Tv \rangle$  in the center of the channel increases too. As a consequence by increasing  $p/e$  the heat flux increases too.

## 5.4 Root Mean Square Temperature

For aligned and staggered square bars distribution the Root Mean square (RMS) of the temperature are shows in the Fig. 5–9. The temperature gradient in both cases is smaller in the channel interior because is the area where the average temperature are locate. Also, the temperature do not have a drastic change like happens in the walls and the turbulators area. The largest temperature gradient are nearby to the walls and in the crest plane of the square bars turbulators. The configuration with the large temperature RMS in the aligned and staggered cases is the  $p/e = 5$ .

## 5.5 Nusselt Number

The Nusselt number (Nu) is a parameter that provides a measure of the heat transfer occurring at the surface of the channel. The Nu it is defined by the non-dimensional temperature gradient at the wall (see Eq. (4.2)). Nusselt number as function of  $p/e$  is shows in the Figure 5–10. In this figure the configuration with  $p/e = 0$  represent the smooth channel.

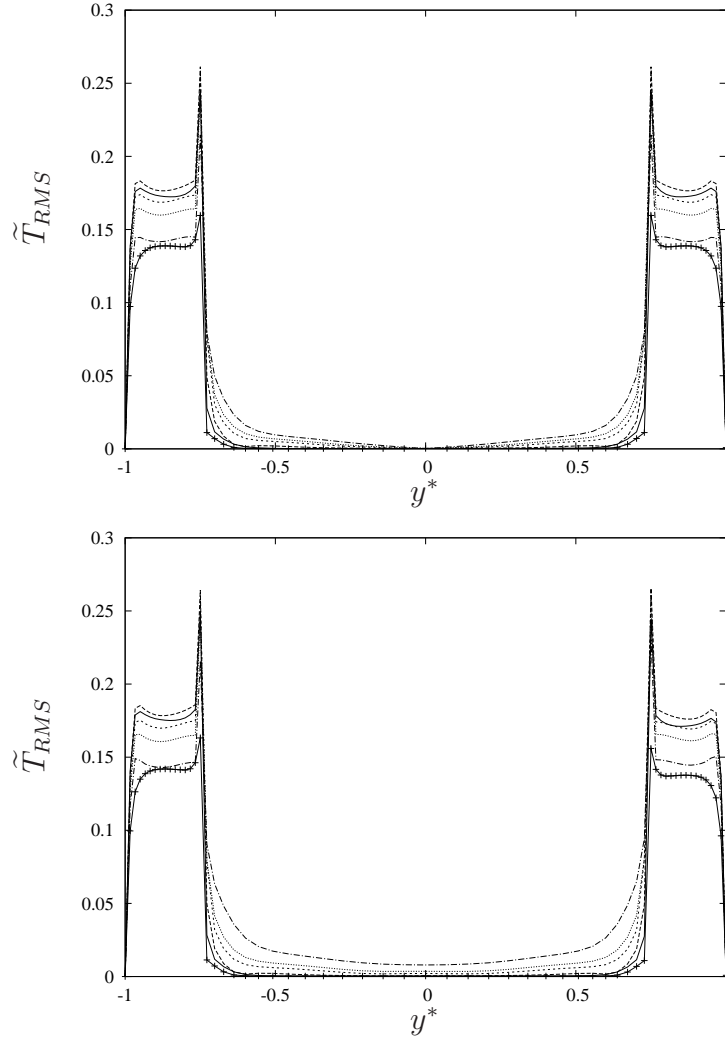


**Figure 5–9: Temperature RMS average in time for Square Bars turbulators. Upper: Aligned, Lower: Staggered.**

(+)  $p/e = 1$ , (—)  $p/e = 3$ , (----)  $p/e = 5$ , (-·-·-)  $p/e = 8$ , (···)  $p/e = 10$ , (---)  $p/e = 15$

The configuration with the highest Nusselt number is the  $p/e = 10$  with Nusselt number equal to 36.49 for the aligned case and 36.62 for the staggered case. That means that the configuration with the  $p/e = 10$  ratio has the highest heat transfer at the surface. According to Leonardi *et al.* (2007) the case with the highest heat transfer was obtain for  $p/e = 7$ .

## 5.6 Skin Friction and Form Drag

The skin friction arises from the interaction between the fluid and the surface of the channel. The skin friction coefficient is a non-dimensional parameter defined by

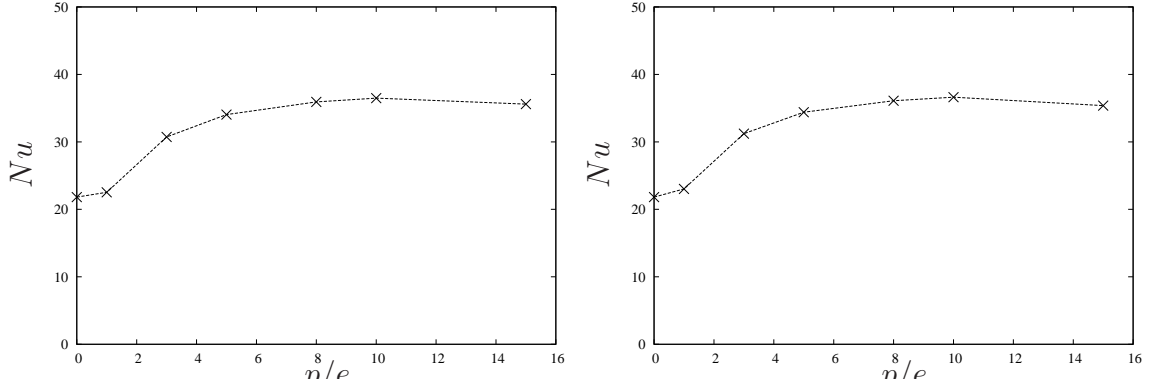


**Figure 5–10: The Nusselt Number on different  $p/e$  for Square Bars turbulators. Left: Aligned, Right: Staggered.**

Equation (4.3). For the square bars turbulators it is negative in the cavity between two rods a recirculation occurs. The friction is positive at the crest plane of the rods. When the  $p/e$  ratio increases the skin friction coefficient decrease (see Figure 5–11) up to a minimum for  $p/e = 10$  and then increase by increasing

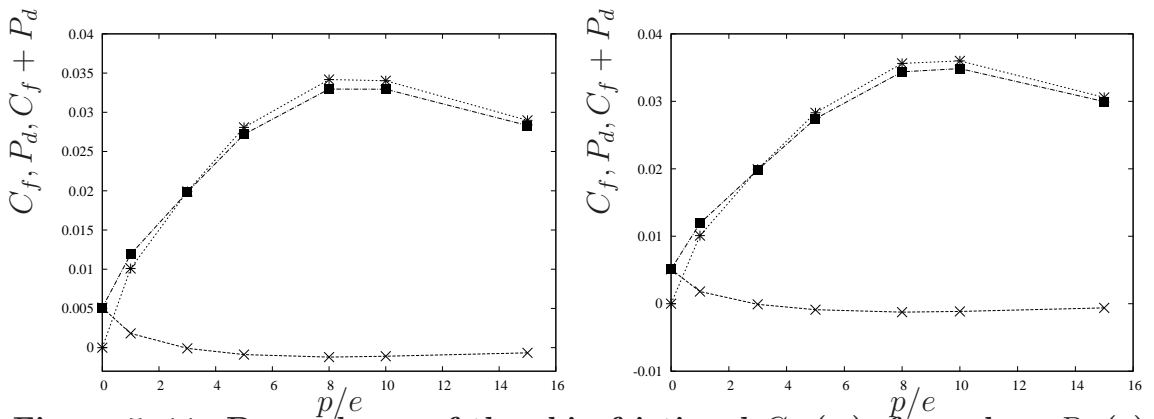


**Figure 5–11: Dependence of the skin frictional  $C_f$  ( $\times$ ), form drag  $P_d$  ( $*$ ) and total drag  $C_f + P_d$  ( $\blacksquare$ ) on different  $p/e$  for Square Bars turbulators. Left: Aligned, Right: Staggered.**

In the square bar turbulator, on the two faces perpendicular to the flow, a difference in pressure is observed. This difference causes the form drag (see Eq. (4.4)). The form drag is calculated projecting the pressure force onto the streamwise direction. The total drag is the sum of both components, the skin frictional and the form drag.

The Figure 5–11 shows the plot of the different contribution to the total drag and shows that the case with the highest value of form drag and total drag is the

configuration of  $p/e = 10$  ratio. For the  $p/e = 10$  ratio the skin friction coefficient and the form drag are  $-0.001143$  and  $0.036$  respectively. The more significant component in the total drag is the form drag, the skin frictional does not affect much the resistance of the flow and have a minimum contribution in the total drag.

Leonardi *et al.* (2003) shows that the case with the higher heat transfer present also the major total drag. In qualitative agreement here the major Nusselt number and total drag are in  $p/e = 10$ , this mean that the heat transfer is correlated with the flow resistance.

## CHAPTER 6

### V-SHAPED TURBULATORS

In the previous past chapter, heat transfer augmentation using square bars turbulators in a turbulent channel flow was clearly observed. Preliminary studies demonstrated that using rib turbulators inclined with respect to the flow direction may enhance the heat transfer [9]. For this reason, a numeral simulation of V-shaped turbulators was performed to observe the difference between V-shaped turbulators and the square bars turbulators.

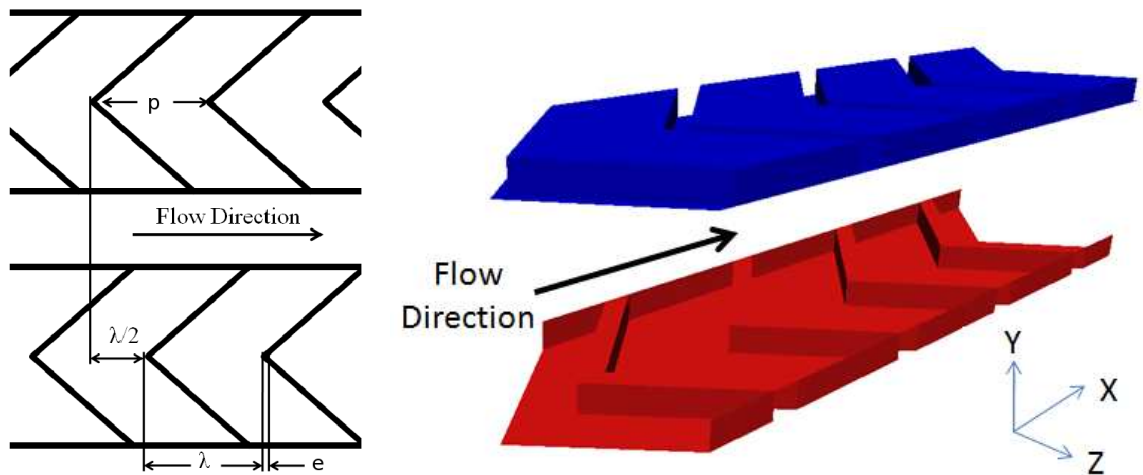


**Figure 6–1: Left: V-Shaped Turbulators Sketch in a Staggered Position. Right: 3-D V-Shaped Turbulators Configuration.**

Numerical simulations have been performed with V-shaped turbulators in the aligned and staggered position. The upper and lower wall have a no-slip condition. Periodicity applies in the streamwise and spanwise direction. Several values of  $p/e$  have been performed ( $p/e = 1, 3, 5, 8, 10$  and  $15$ , where  $e$  is the bar height and  $p$  is the longitudinal separation between consecutive bars). The Figure 6–1 (Left) shows

a sketch of the geometry of the turbulators in the turbulent channel for the  $p/e = 3$  configuration.

## 6.1 Mean Flow

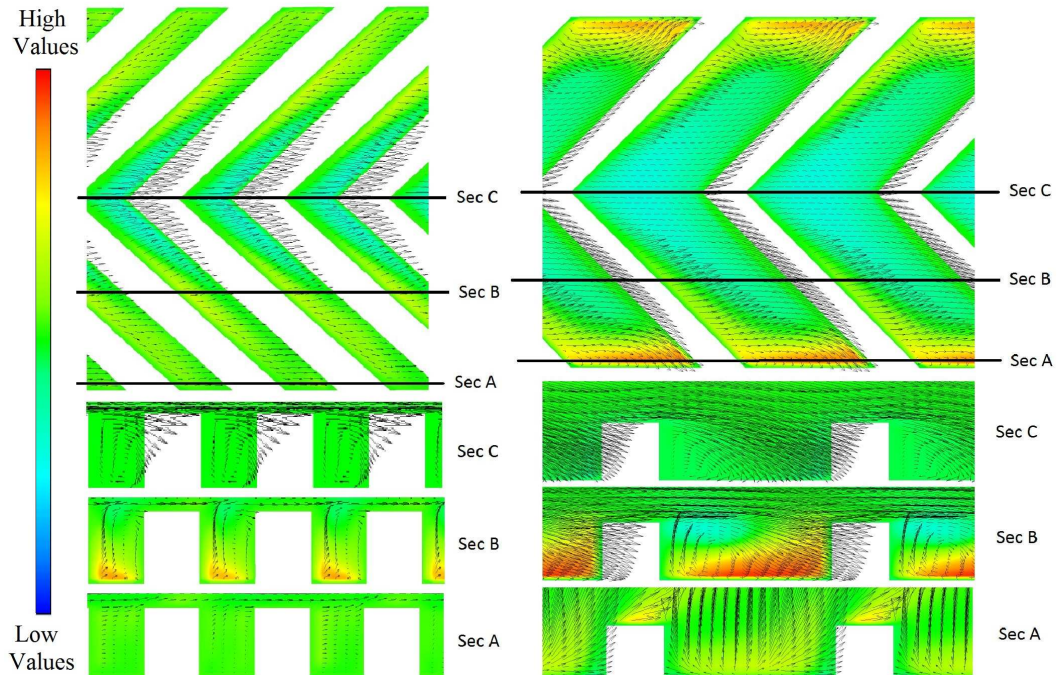


**Figure 6–2: Top: Top view of the Normal Average Velocity contour with velocity vectors for V-Shaped turbulators (Left:  $p/e=1$ , Right:  $p/e=3$ ). Bottom: Side view of the Spanwise Average Velocity contour with velocity vector for the V-shaped turbulators (Left:  $p/e=1$ , Right:  $p/e=3$ ).**

The flow structure in a square channel with V-shaped turbulators is different compared with the channel with square bars turbulators. The Figure 6–2 shows different section of the V-shaped turbulators for the staggered configurations of  $p/e = 1$  and  $p/e = 3$ . The normal average velocity contour and velocity vectors are taken near to the crest plane (this section is shown on the Figure 6–2). For Sec. C when the fluid hits the roughness, the fluid is separated in two direction following the cavity inclination. It is possible to observe that at the trailing edge of the roughness a recirculation is formed.

In the Sec. B it still exists a recirculation at the trailing edge but the fluid follow the spanwise direction. In Sec. A, close to the side walls of the V-shaped

turbulators the flow hits the side walls and then an upward ejection occurs. This creates two big counter-rotating vortices in opposite directions on each side of the channel. This behavior is also observe for Lee D.H. [9].

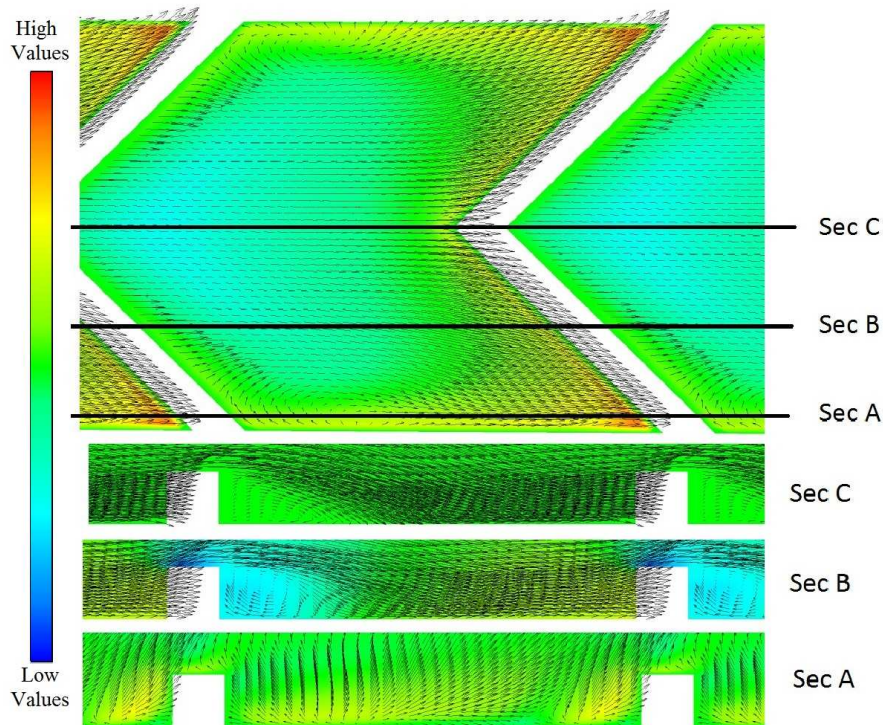


**Figure 6–3: Top Left: Normal Average Velocity Contour with velocity vectors for  $p/e=8$  for V-Shaped turbulators. Bottom Left: Spanwise Average Velocity contour with velocity vector for  $p/e=8$  for the V-Shaped turbulators.**

For square bars turbulators, it is found that the flow reattaches on the bottom wall when  $p/e > 8$ . When the flow starts to reattach, the distance between the V-shaped turbulators does not have an important effect compared with the cases with a ratio between  $3 \leq p/e \leq 7$ . In the Sec. C, for the  $p/e = 8$  configuration (see Figure 6–3) it is possible to observe the reattachment on the bottom wall. A recirculation on the trailing edge of the V-shaped turbulators is also observed. In the zone close to the side walls (Sec. A) an upward ejection occurs similarly to  $p/e = 3$ . The behavior of the flow for  $p/e = 10$  and  $p/e = 15$  is very similar of the  $p/e = 8$  configuration. In these cases the reattachment is on the bottom of the two walls

and the V-shaped turbulators don't have the same effect on the flow compared with the cases of ratio between  $3 < p/e < 7$ . In the  $p/e = 15$  the flow acts independent of the configuration array.

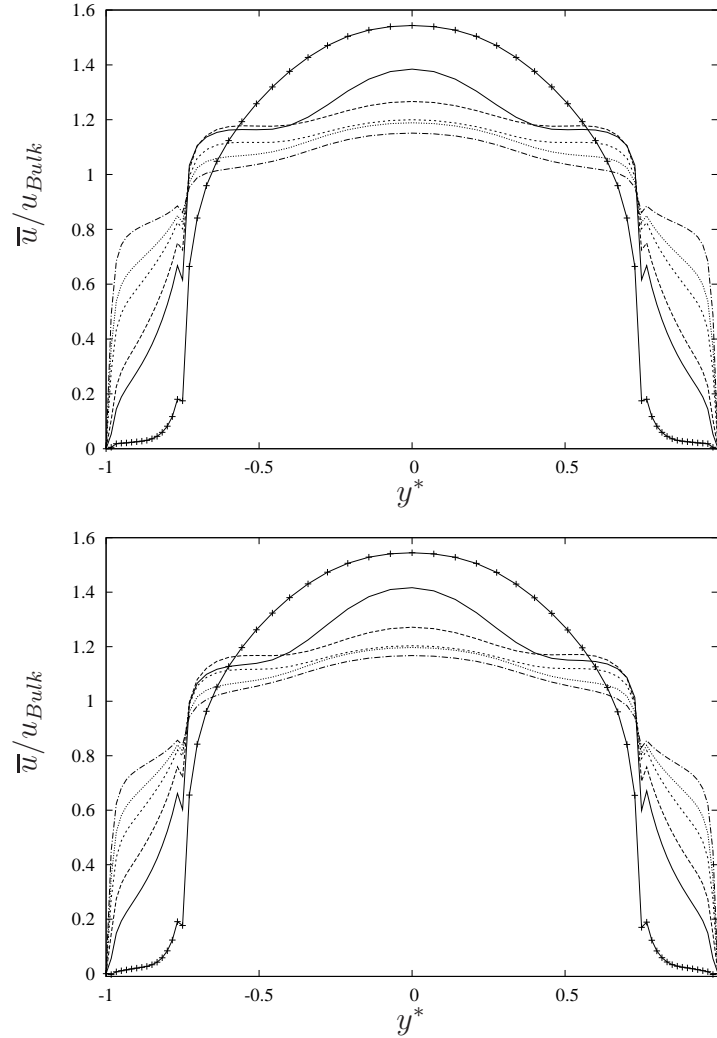


**Figure 6–4: Streamwise Average Velocity profile distribution for V-Shaped turbulators. Upper: Aligned, Lower: Staggered.**

(+)  $p/e = 1$ , (—)  $p/e = 3$ , (---)  $p/e = 5$ , (-·-·-)  $p/e = 8$ , (···)  $p/e = 10$ , (----)  $p/e = 15$

In the square channel the lower and upper wall are located at  $y^* = -1$  and  $y^* = +1$  respectively. The crest plane of the V-shaped turbulators for the lower wall are located at  $y^* = -0.75$  and for the upper wall it is located at  $y^* = +0.75$ . Figure 6–4 shows the streamwise average velocity distribution in the normal distance of the channel for the aligned and staggered configuration. It is observed that for

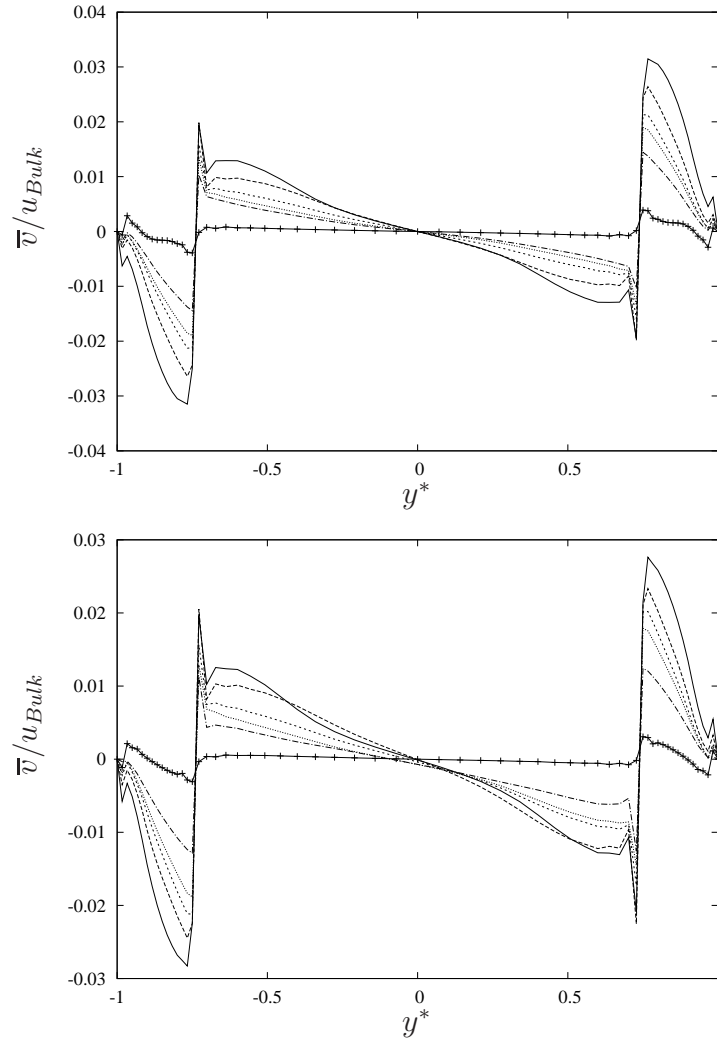


**Figure 6–5: Normal Average Velocity profile distribution for V-Shaped turbulators. Upper: Aligned, Lower: Staggered.**

all cases the average velocity reach the maximum value at the centerline ( $y^* = 0$ ). The average velocity in the V-shaped turbulators experience the lowest values in the lower and upper walls. The streamwise average velocity, near the roughness layer has the lowest value for  $p/e = 1$ . That is because in the cavity area of  $p/e = 1$  the flow rate is very low and the major amount of the fluid is in the center of the channel. The center of the channel for the  $p/e = 1$  configuration is the one with the highest value of the streamwise average velocity. While  $p/e$  increases, the streamwise average velocity on the turbulators area increases too and meanwhile the streamwise average velocity in the center of the channel is reduced.

Figure 6–5 shows the average normal wall velocity distribution. It is possible to see in the figure that highest velocities are near the crest plane of the V-shaped turbulators. The normal wall velocity has a sharp gradient close to the crest plane. This drastically change of average velocity in the normal direction is because in the leading edge of the turbulators, close to the crest plane, the normal average velocity are in the negative direction due to the recirculation in this area. Then, the fluid hit the top of the crest plane causing an ejection outward the wall. Also, it is observed near the upper corner of the ribs (on the upstream edge) the presence of a stagnation point. This has a high pressure and induce two large pressure gradients one upward inducing ejections, and one downward so that the flow enters into the cavity. The more intense is the stagnation point, the stronger are the pressure gradients and then the normal wall velocities. The upper and the lower walls have the same velocity magnitude with opposite direction.

In the Figure 6–5 the  $p/e = 1$  configuration does not have a significant change in the normal velocity because the space of the cavity is not enough for the flow to enter since the momentum of the flow in the cavity is low, ejections are low also. The  $p/e = 3$  configuration has the maximum normal velocity magnitude. For  $p/e > 3$ , by increasing  $p/e$  the normal velocity magnitude decrease up to a minimum for  $p/e = 15$ .

To understand better the physical behavior of the flow in a channel with V-shape turbulator a streamtracer figure is shown (Figure 6–7). In this figure is possible observe how the fluid move inside the turbulators and the development in the middle of the channel. When the flow enter in the cavity and hits the V-Shape turbulators, the flow follow the V-Shape turbulators inclination. Then, the flow hit the side walls and has an upward ejections. These ejections are the responsible of the secondary motion. After these ejections, the flow continue in the streamwise direction. In this figure is also shown the recirculation in the trailing edge of the V-Shape turbulators.

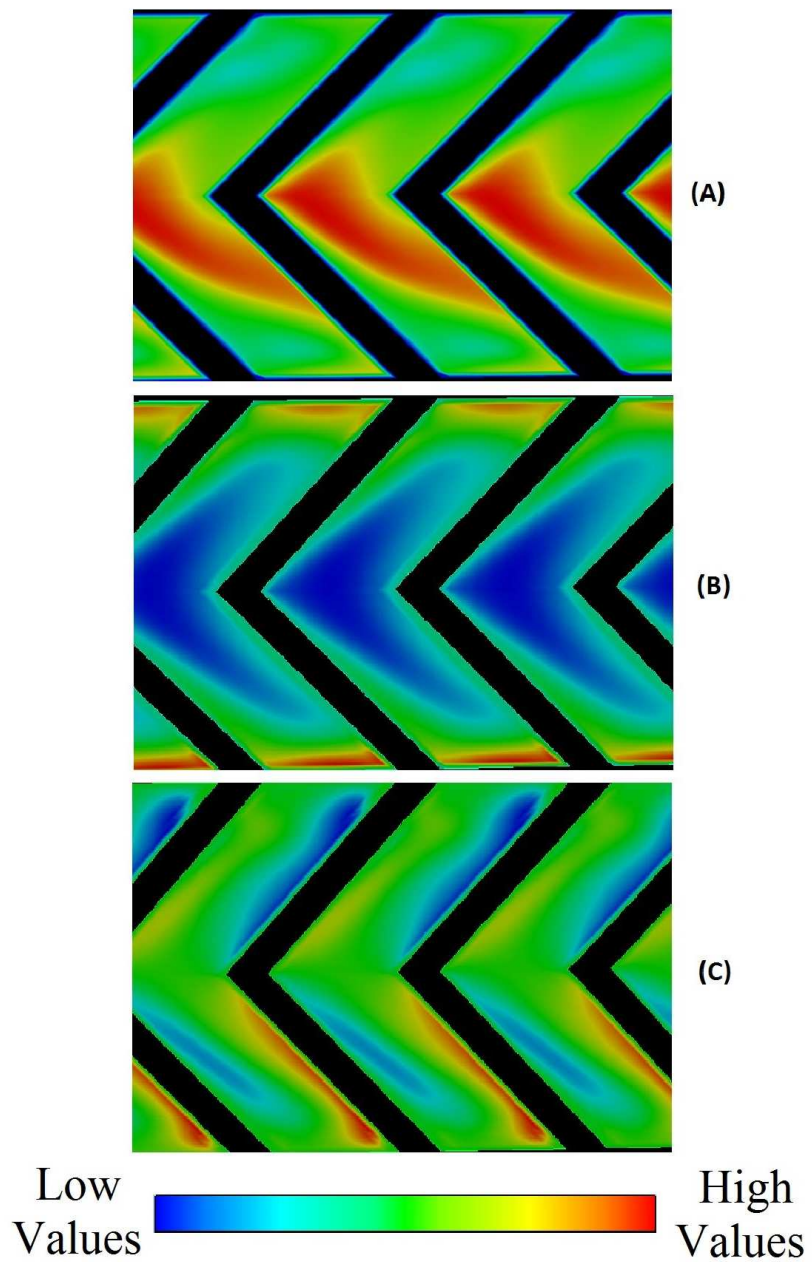
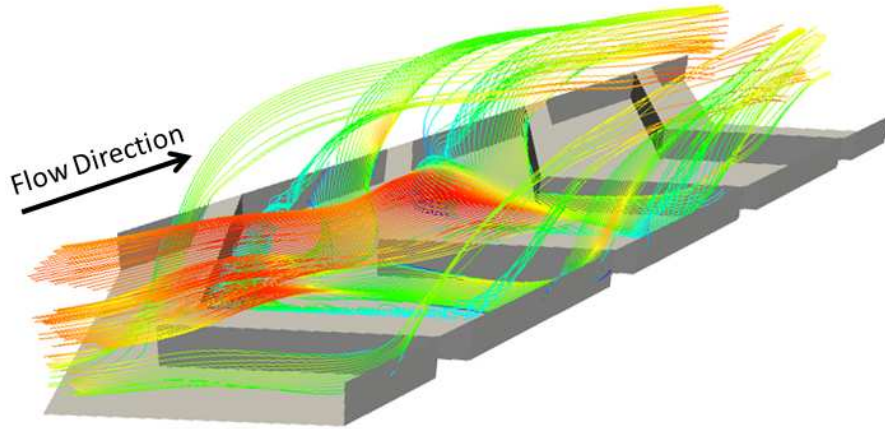


Figure 6–6: Average Velocity contour for the three direction in the  $p/e = 3$  configuration for V-Shaped turbulators. (A) Streamwise Average Velocity. (B) Normal Average Velocity. (C) Spanwise Average Velocity.



**Figure 6–7: Velocity Streamtracer in the Streamwise Direction for V-Shape turbulators.**

To see how is the development of the fluid in the cavity of the V-shaped turbulators a color contour of velocity is presented in the Figure 6–6. The figure presents a horizontal section taken near to the crest plane of the turbulators. The red color represents the highest velocities while the blue color represents the lowest magnitude velocities.

## 6.2 Velocity Root Mean Square (RMS)

The Equation 5.2 is used to calculate the velocity RMS. The RMS is calculated for the different cases (Aligned and Staggered) for all  $p/e$  ratio. Figure 6–8 shows the RMS for the streamwise velocity along the normal distance. The behaviors of the velocity RMS for both cases (aligned and staggered) is very similar. Both cases present the highest streamwise velocity RMS on the crest plane of the V-shaped turbulators. This is due to the large vortices in the streamwise direction and to the pressure gradient at the edge of the turbulators. The velocity RMS in the cavity increases by increasing the  $p/e$  ratio. The center of the channel the RMS decreases but the lowest RMS is obtained for the case of  $p/e = 1$ . For the aligned and staggered configuration the highest streamwise velocity RMS is presented in the  $p/e = 3$  cases. The RMS of the normal wall velocity is shown in Figure 6–9. It is possible to notice that the RMS increases at the crest plane of the V-shaped

turbulators. This increase is due for the ejection of the flow in the normal direction when the flow particles hit the leading edge of the crest plane turbulators. In the center of the channel the normal velocity RMS has the lowest values because the flow goes mainly in the streamwise direction and turbulence levels are lower.

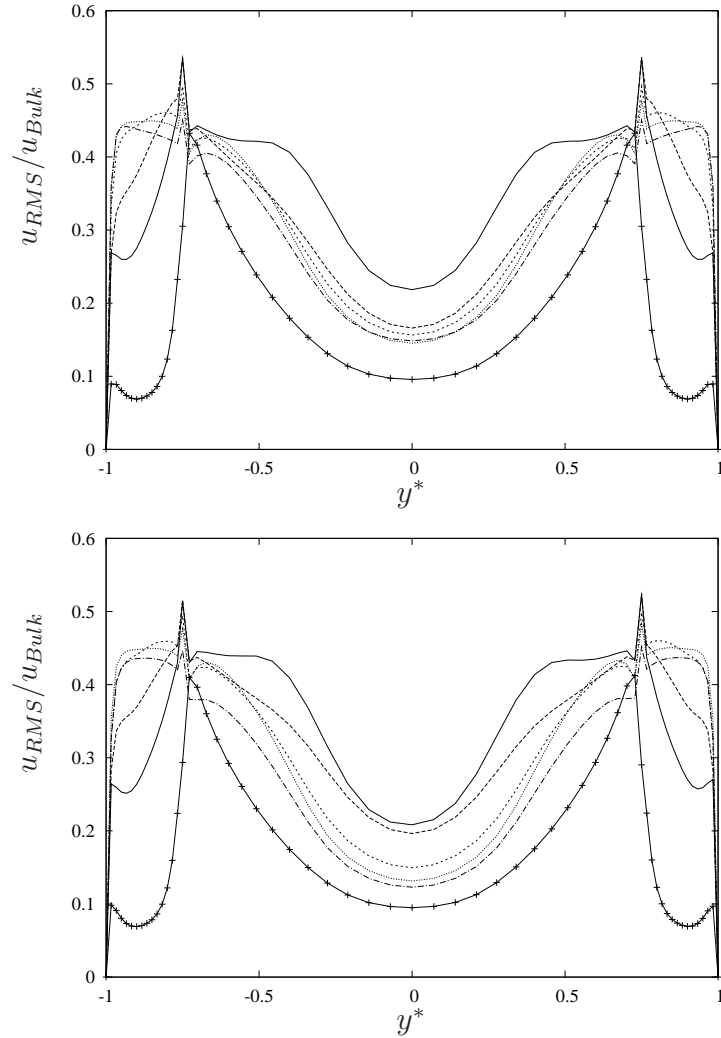


**Figure 6–8: Streamwise Velocity RMS average in space for V-Shape turbulators. Upper: Aligned, Lower: Staggered.**

(+)  $p/e = 1$ , (—)  $p/e = 3$ , (---)  $p/e = 5$ , (-·-·-)  $p/e = 8$ , (···)  $p/e = 10$ , (— — —)  $p/e = 15$

The largest RMS is in the spanwise velocity and is presented close to the lower and upper walls. When the flow enters in the cavity it follows the inclination of the V-shaped turbulators and goes in the streamwise and the spanwise direction. The kink of the turbulators form streams moving in opposite spanwise direction. Therefore,

the mean spanwise average velocity is zero and the spanwise RMS velocity present the highest values at the walls.

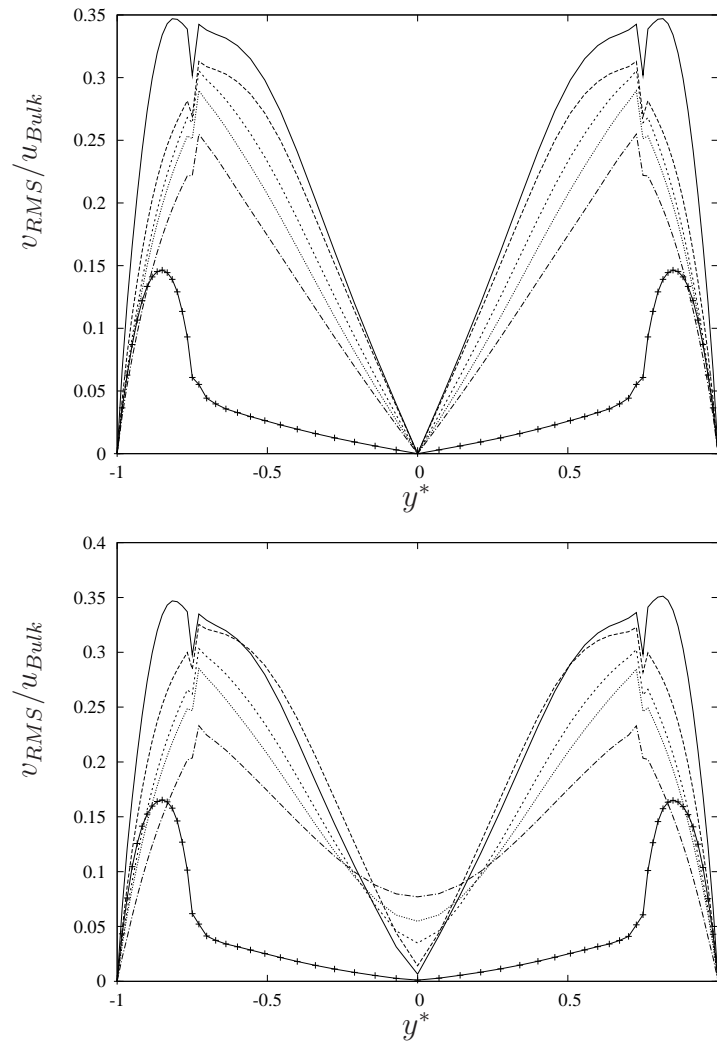


**Figure 6–9: Normal Velocity RMS average in space for V-Shape turbulators. Upper: Aligned, Lower: Staggered.**

(+)  $p/e = 1$ , (—)  $p/e = 3$ , (----)  $p/e = 5$ , (-·-·-)  $p/e = 8$ , (···)  $p/e = 10$ , (---)  $p/e = 15$

### 6.3 Mean Temperature

The temperature was defined in a previous section. The lowest wall being the hot wall ( $\tilde{T} = +1$ ) and the upper wall the cold wall ( $\tilde{T} = -1$ ). The temperature distribution along the normal distance for the V-shaped turbulators is shown in the Figure 6–11. There exist similarities in temperature profile between the aligned and staggered cases of the V-shaped turbulators. The temperature has a constant

distribution in the roughness layer in the lower and upper walls except in the area close to the walls. This constant distribution is an effect of the turbulators. These configurations have a constant temperature distribution in the cavity area and a smooth distribution of the temperature at the center of the channel.

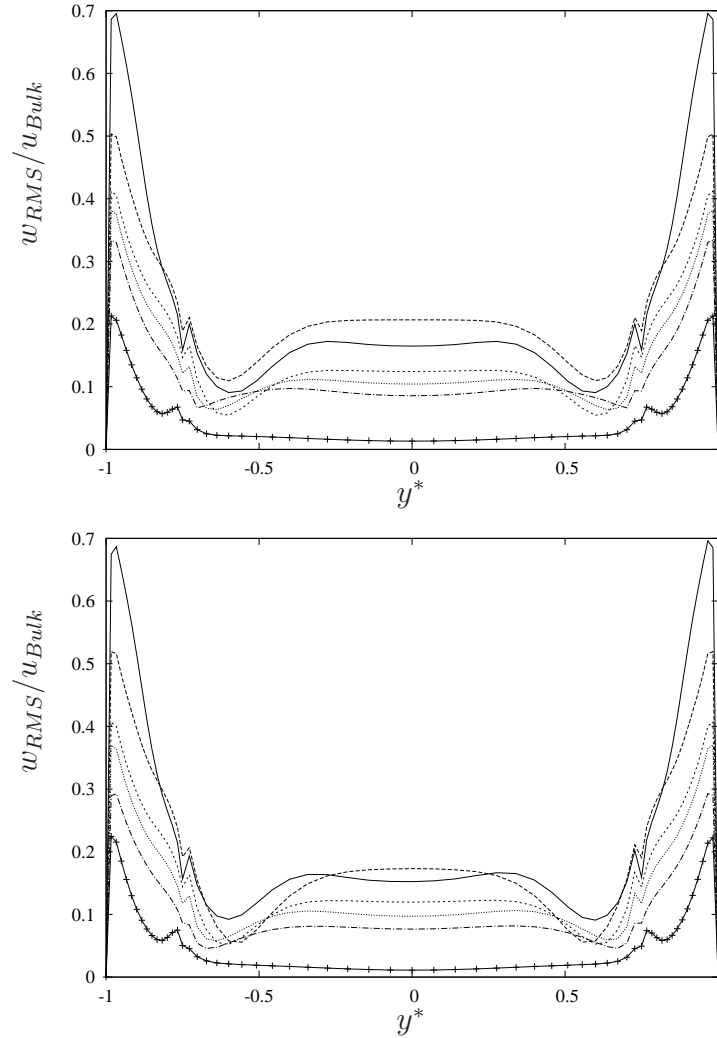


**Figure 6–10: Spanwise Velocity RMS average in space for V-Shape turbulators. Upper: Aligned, Lower: Staggered.**

(+)  $p/e = 1$ , (—)  $p/e = 3$ , (----)  $p/e = 5$ , (-·-·-)  $p/e = 8$ , (···)  $p/e = 10$ , (---)  $p/e = 15$

The temperature gradient at the wall is highest and it takes into account the heat flux at the flux. The lowest case is the  $p/e = 1$  which in fact is the case with less interaction between outer and inner flow. For  $p/e = 3$  the temperature in the lower wall cavity decreases (is colder) due to the stronger mixing with the outer layer

flow and the larger vertical fluctuations discussed before. For  $p/e = 1$  turbulent convection is low, the heat goes from the lower wall to the upper wall  $d\tilde{T}/dy^*$  for conduction mainly. On the other hand for  $p/e = 3$   $\langle Tv \rangle$  is very large and  $d\tilde{T}/dy^*$  is low, the heat is transferred mostly for turbulent convection.

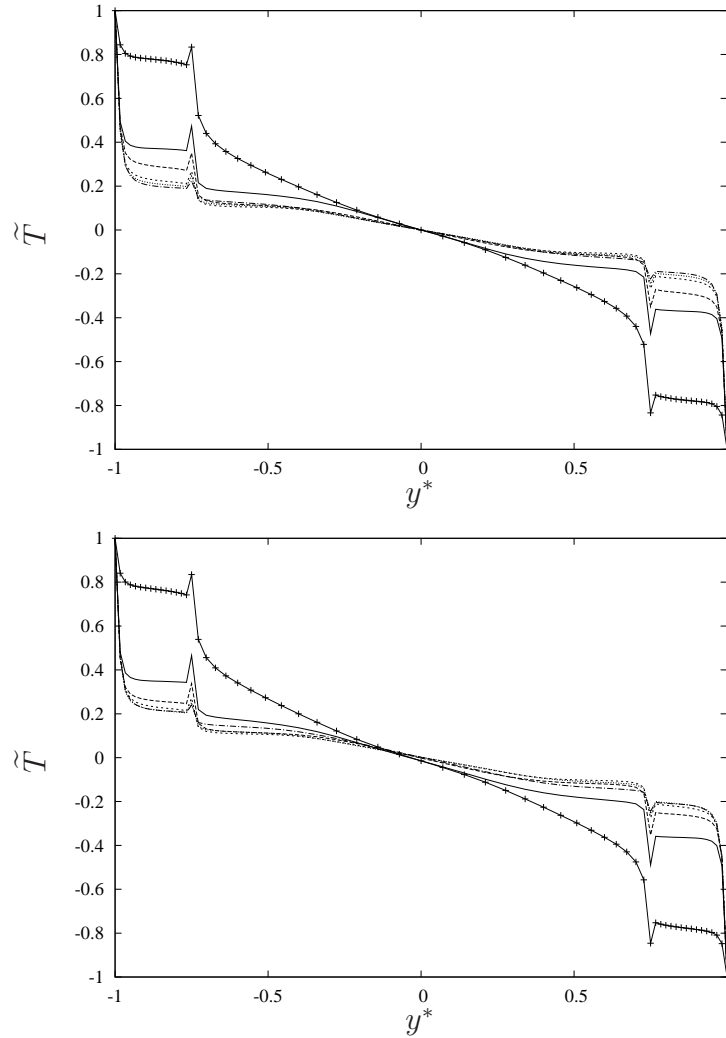


**Figure 6–11: Temperature profile distribution for V-Shape turbulators. Upper: Aligned, Lower: Staggered.**

(+)  $p/e = 1$ , (—)  $p/e = 3$ , (----)  $p/e = 5$ , (-----)  $p/e = 8$ , (···)  $p/e = 10$ , (---)  $p/e = 15$

## 6.4 Root Mean Square (RMS) Temperature

As mentioned before, the temperature RMS is a measure of the difference between the temperature in a point with the average temperature of the channel. The highest RMS temperatures are presented at the crest plane of the turbulators in the

upper and lower wall of the channel. The temperature gradient in this zone is very significant compared to other flow regions. The same conduct is presented in the both walls of the channel, where the temperature RMS is very large. This behavior is the same for the aligned and staggered configuration. The smaller temperature RMS is found at the center of the channel. The  $p/e = 3$  case has the highest RMS temperature for both configurations. This is not surprising since  $p/e = 3$  is the configuration with highest mixing and heat transfer.

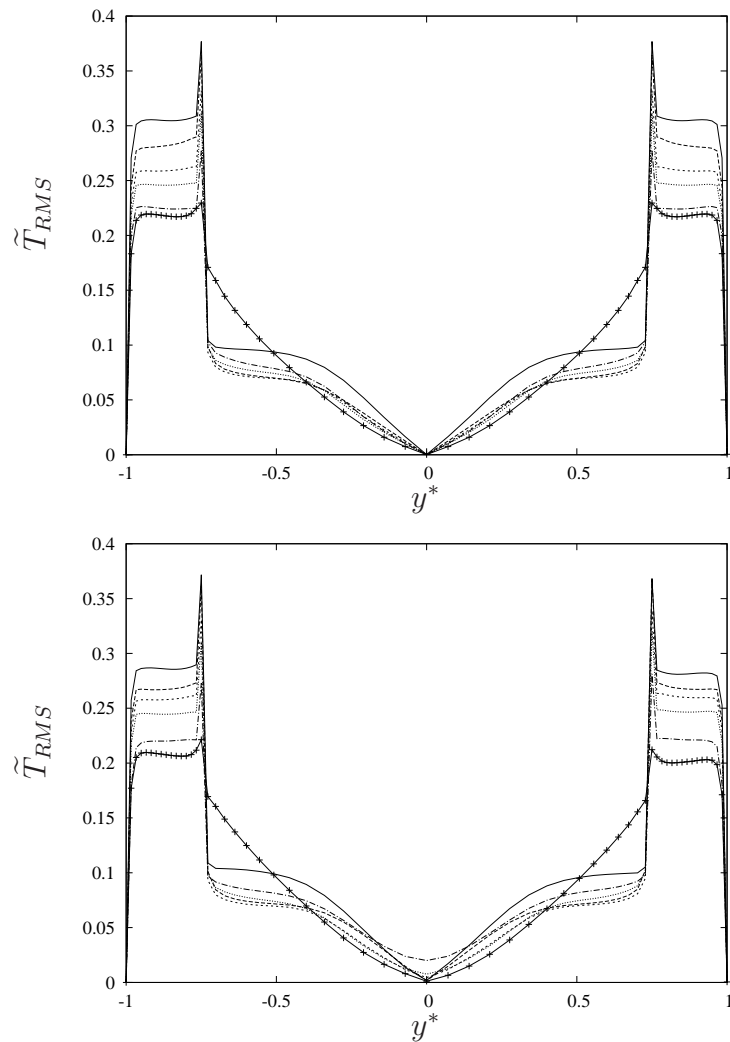


**Figure 6–12: Temperature RMS average in space for V-Shape turbulators. Upper: Aligned, Lower: Staggered.**

(+)  $p/e = 1$ , (—)  $p/e = 3$ , (----)  $p/e = 5$ , (-·-·-)  $p/e = 8$ , (···)  $p/e = 10$ , (---)  $p/e = 15$

## 6.5 Nusselt Number

The Nusselt number was define before as the dimensionless temperature gradient at the surface and provides a measure of the heat transfer occurring at the surface (see Eq. (4.2)). Figure 6–13 present the different Nusselt for the different study layout.

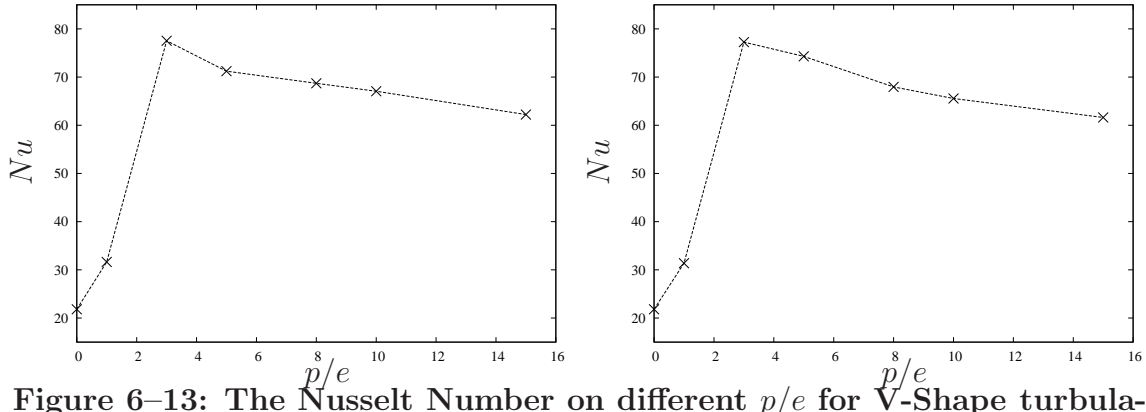


**Figure 6–13: The Nusselt Number on different  $p/e$  for V-Shape turbulators. Left: Aligned, Right: Staggered.**

For both the aligned configuration and staggered configuration the highest Nusselt number is the case with a pitch to height ratio  $p/e = 3$ . The Nusselt number for both configuration is very similar. The former being  $Nu = 77.52$ , the latter  $Nu = 77.82$ . This difference is within the numerical error and does not have a particular physical meaning.

## 6.6 Frictional Drag and Form Drag

Equation (4.3) shows how it is calculated the frictional drag. A difference in pressure between leading and trailing edge of the turbulators is the cause of the form drag (Eq. (4.4)).

The total drag is the sum of both contributions, the skin friction coefficient and the form drag (Figure 6–14). It is possible to observe that the maximum contribution to the total drag is the form drag. The skin friction is only a small part of this value. For the aligned configuration the  $p/e = 3$  has the highest total drag which is equal to 0.0987. For  $p/e > 3$  the total drag decreases by increasing  $p/e$ . For the staggered

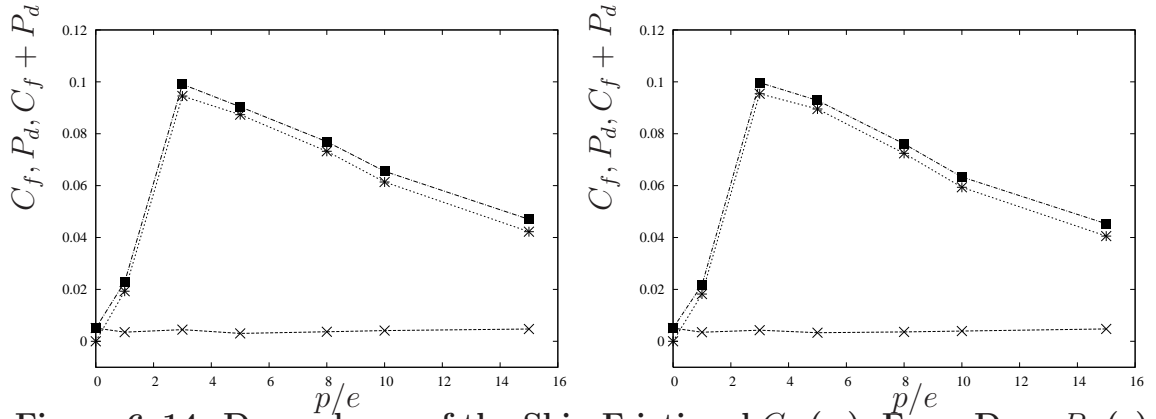


**Figure 6–14: Dependence of the Skin Frictional  $C_f$  ( $\times$ ), Form Drag  $P_d$  ( $*$ ) and Total Drag  $C_f + P_d$  ( $\blacksquare$ ) on different  $p/e$  for the V-Shape turbulators. Left: Aligned, Right: Staggered.**

configuration the  $p/e = 3$  has a total drag value of 0.0997. This configuration has the same behavior of the aligned configuration.

## 6.7 Comparison between the RANS model with DNS (V-Shaped)

A comparison of the V-shaped turbulators for the staggered configuration was performed for the RANS model with a Direct Numerical Simulation (DNS). The boundary conditions used are the same of the RANS simulations here discussed. No-slip conditions are applied in the upper and lower wall. Periodic conditions in the streamwise and spanwise direction are applied. A Reynolds number of 10,400 are used in both simulations. The configuration with the  $p/e = 3$  ratio was considered. The turbulators on the upper wall are staggered of half wavelength compared to those on the lower wall.

The streamwise average velocity ( $u/u_{Bulk}$ ) as a function of the normal distance ( $y^*$ ) is shown in the Figure 6–15. The streamwise average velocity for the DNS case (----) shows a slower velocity in the cavity compared with the RANS case (—). In the crest plane of the V-shaped turbulators ( $y^* = \pm 0.75$ ) the two models (— and ----) agree well. In the center of the channel the velocity calculated with the DNS is about 7% higher. Overall the two simulations agree in

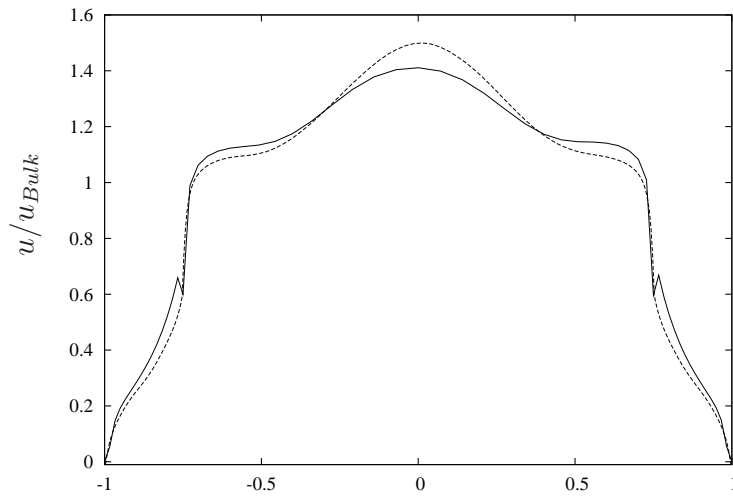


**Figure 6–15: Streamwise Average Velocity profile distribution for V-Shaped turbulators: (—) RANS, (----) DNS.**

good approximation. Considering that the grid of the DNS was  $192 \times 192 \times 600$  finer than the used for RANS, the results obtained with RANS are very encouraging.

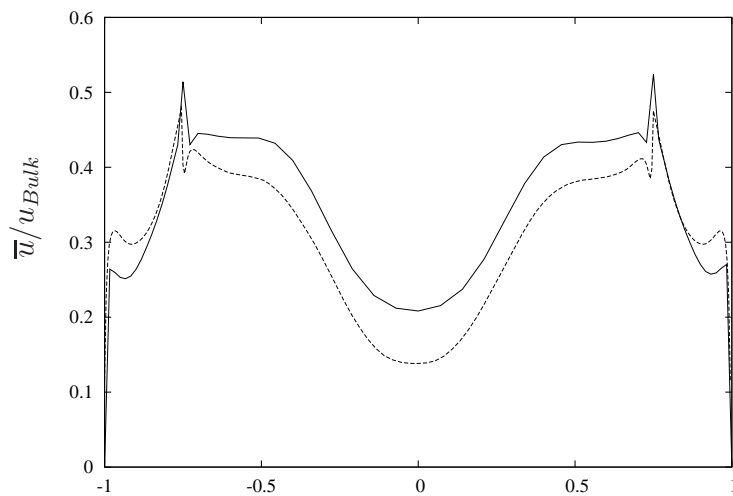


**Figure 6–16: Streamwise Velocity RMS average in space for V-Shape turbulators: (—) RANS, (----) DNS.**

The velocity Root Mean Square (RMS) demonstrates how much the velocity values for the field deviates from the average. The Figure 6–16 shows the streamwise velocity RMS for the RANS (—) and the DNS (----) cases. Although the two simulations have in the behavior some differences and this can be observed especially at the center of the channel. The RANS model presents higher RMS in this area

compared with the DNS. In the cavity area (specifically in the area near to the crest plane of the turbulators  $y^* = \pm 0.75$ ) both cases have a similar behavior.

The RMS of the normal and spanwise velocity components are shown in Figure 6–17 and Figure 6–18 respectively. The profile relative to the RANS and the DNS simulations are very similar. In the case of the normal velocity there are only two small differences. The first difference is in the center of the channel ( $y^* = 0$ ), the RANS simulation have a RMS velocity smaller than the DNS. The second difference is in the area around the crest plane of the V-shaped turbulators, where the DNS simulation present a higher RMS compared with the RANS simulation.

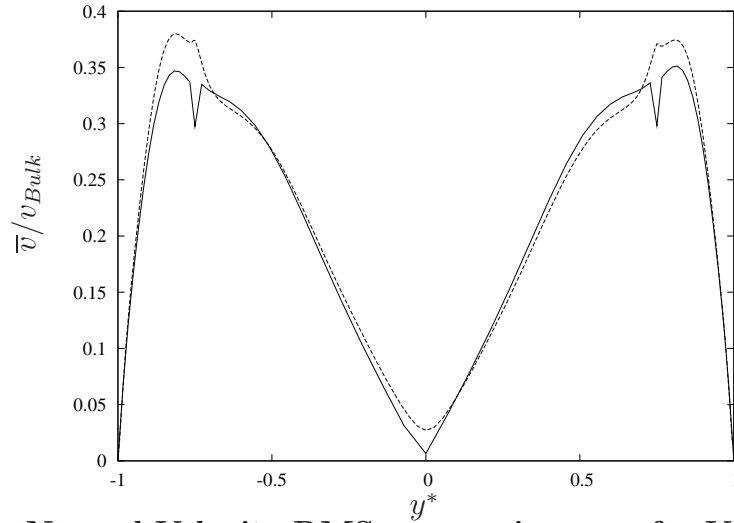


**Figure 6–17: Normal Velocity RMS average in space for V-Shape turbulators: (—) RANS, (----) DNS.**

The RMS of spanwise velocity of the DNS and RANS simulations presents the same behavior in the cavity area and in the center of the channel. On both walls the spanwise velocity RMS is slightly higher for the RANS simulation. Otherwise, in the area after the crest plane of the V-shaped turbulators the DNS presents a higher value than that of the RANS simulation.

Comparing the temperature for the DNS and RANS simulation (Figure 6–19) is observed a similar behavior in the temperature profile. In the center area of the channel the RANS and DNS simulation has small differences. The biggest difference

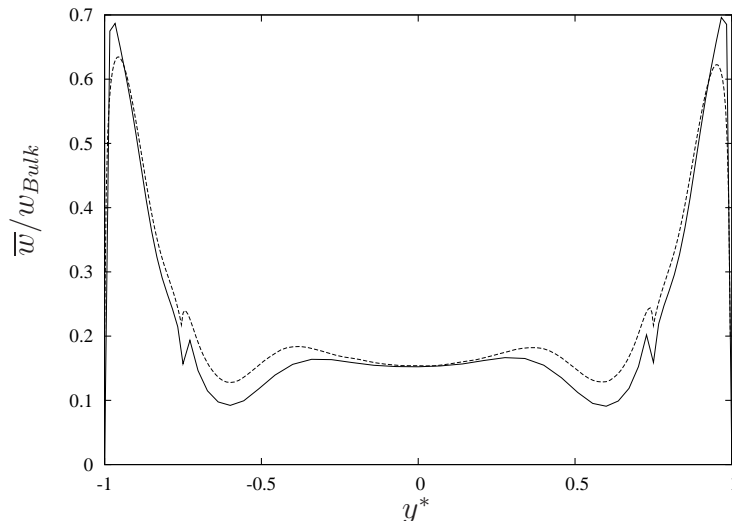


**Figure 6–18: Spanwise Average Velocity RMS average in space for V-Shape turbulators: (—) RANS, (----) DNS.**

is in the cavity area of the V-shaped turbulators in which the RANS simulation has a highest gradient compared with the DNS simulation. This is the region where RANS model the unsteady phenomena such as recirculation and stagnation points oscillating in time while the DNS accurately solves it. A difference with DNS which resolve the Navier-Stokes and Energy equations in time is expected.

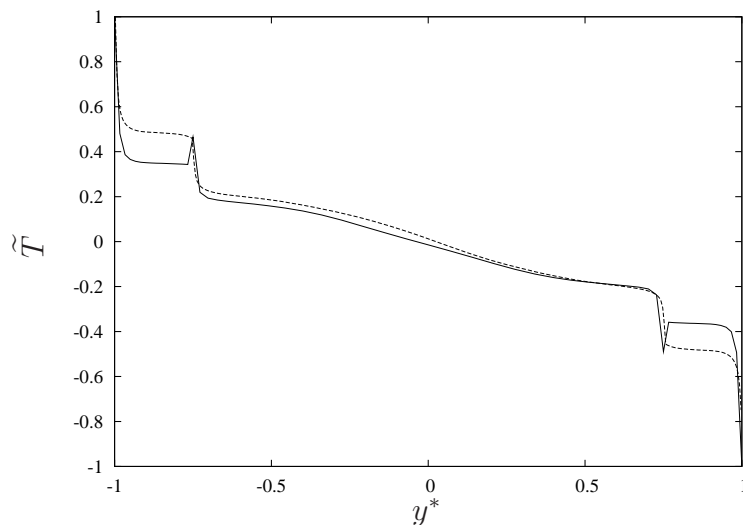


**Figure 6–19: Temperature profile distribution for V-Shape turbulators. (—) RANS, (----) DNS.**

For the temperature RMS, RANS and DNS simulations present a similar behavior in which the minimum temperature RMS is in the center of the channel (Figure

6–20), the temperature RMS in this area is close to zero. There is a difference in the cavity area on the RMS temperature plot. The DNS results show higher temperature RMS in the cavity area than that relative to the RANS simulation. This means that the heat transfer obtained in the RANS simulation will be higher than that obtained with the DNS simulation.

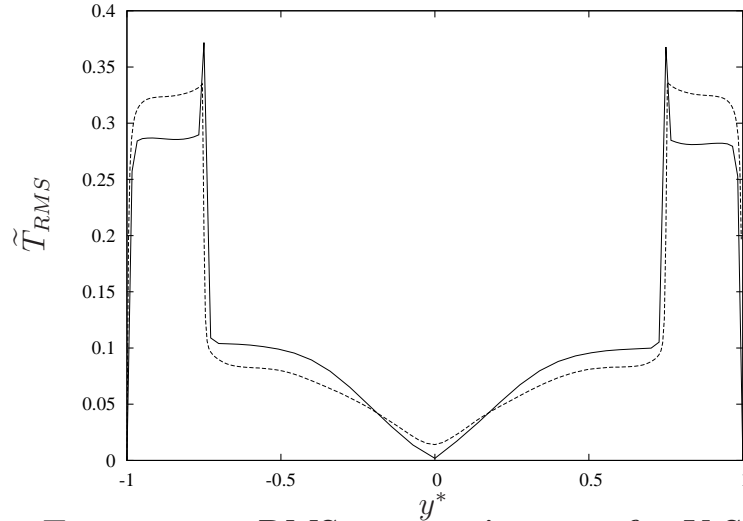


**Figure 6–20: Temperature RMS average in space for V-Shape turbulators. (— ) RANS, (---- ) DNS.**

The surface Nusselt number obtained for the RANS simulation and the DNS is 77.82 and 50.8 respectively (see Figure 6–21). The RANS simulation presents the higher Nusselt number as it expected by the higher temperature gradient at the wall shown in Figure 6–19. The percentage of difference of the Nusselt number (Nu) was calculated, with a corresponding value of 42%.

Another comparison between the RANS and the DNS simulation is the part of the total drag. The total drag is made up of the form drag and the frictional drag. The total drag for the RANS simulation is 0.0997 meanwhile the total drag for the DNS simulation is 0.0632. The difference percentage of the total drag for the RANS and the DNS simulation is 44.8%.

In conclusion the comparison between RANS and DNS is encouraging. It is recalled that the DNS performed by Lucena [19] has about 25 million points and

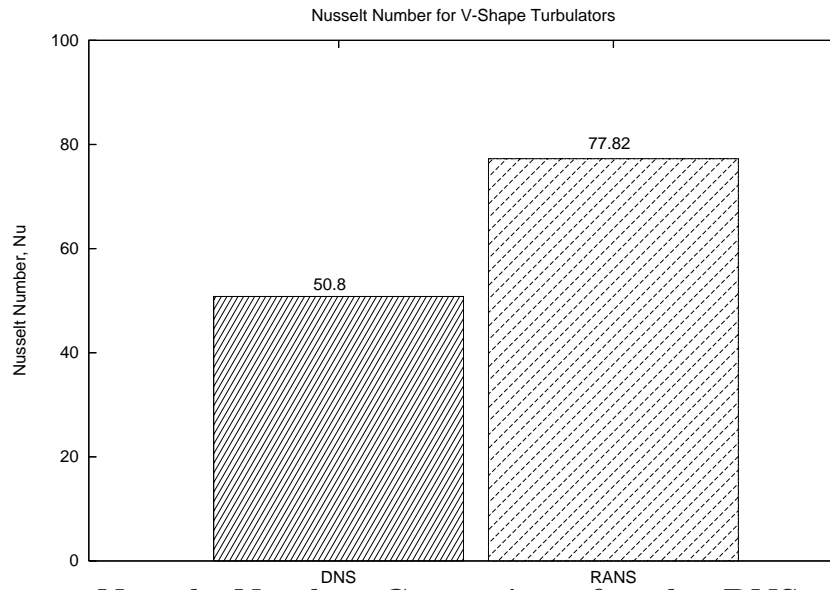


**Figure 6–21: Nusselt Number Comparison for the DNS and RANS model.**

runs for about one month on 32 processors in the super computer center in Texas. The simulations here discussed run for about two days on a grid of about 500,000 points.

Despite the coarse resolution and the use of simple turbulence models, first and second order statistics agree extremely well. Higher error are found for the heat flux and total drag, in fact temperature and pressure gradients cannot be calculated accurately with a coarse grid and are affected by the dynamics of vorticity.

# CHAPTER 7

## SEGMENTED V-SHAPED TURBULATORS

In practical applications is very difficult to manufacture the kind of a V-shaped turbulators as shown in the previous chapter. For this reason a gap ( $G$ ) is used between the two straight ribs (see Fig. 7-1). Reynolds Average Navier-Stokes simulations have been performed for a turbulent channel with broken V-shaped turbulators on the walls. The mean velocity distribution is independent whether the turbulators on the upper wall are aligned or staggered with the lower wall.

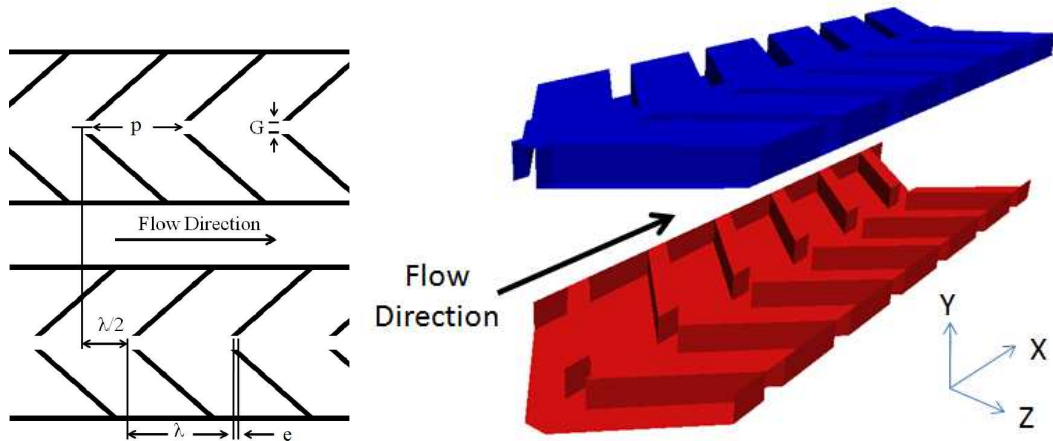
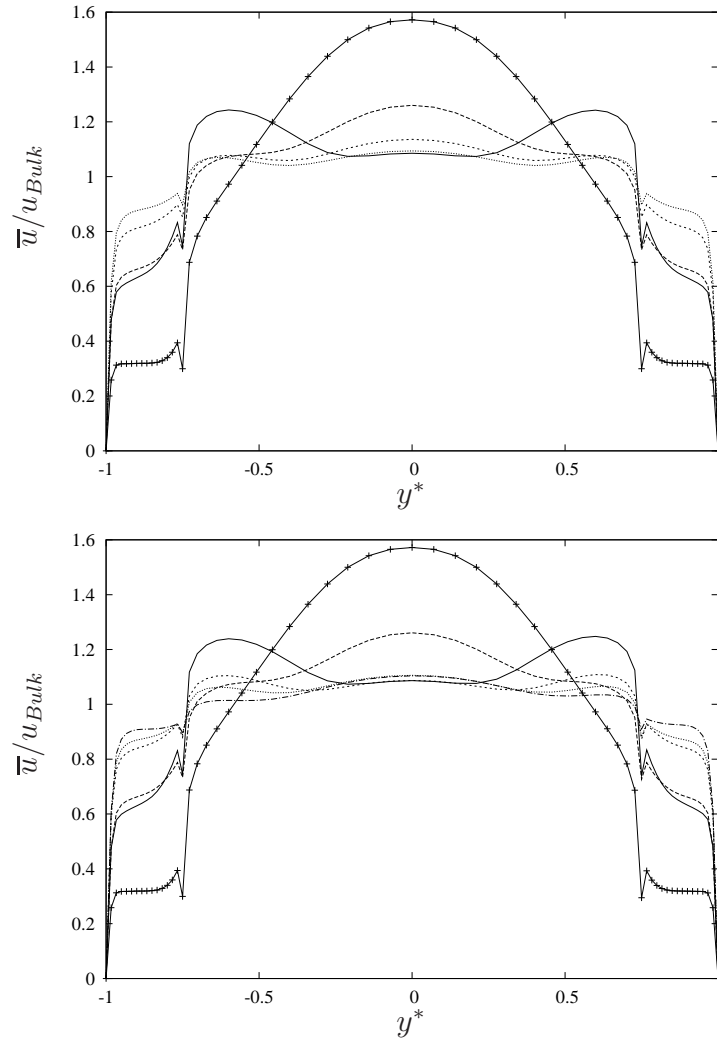


Figure 7-1: Left: Segmented V-Shaped Turbulators Sketch. Right: 3-D Segmented V-Shaped Turbulators Configuration.

### 7.1 Mean Flow

The streamwise distribution along the normal distance is presented in Figure 7-2. It is observed that the highest streamwise velocities are in the center of the channel. The  $p/e = 1$  case presents the minimum velocity in the ribs area and the maximum velocity in the center of the channel. While the  $p/e$  ratio increases the streamwise velocity in the center decreases.



**Figure 7–2: Streamwise Average Velocity profile distribution for Segmented V-Shaped turbulators. Upper: Aligned, Lower: Staggered.**

(+)  $p/e = 1$ , (—)  $p/e = 3$ , (----)  $p/e = 5$ , (-·-·-)  $p/e = 8$ , (···)  $p/e = 10$ , (---)  $p/e = 15$

The normal velocity profile for the segmented V-shaped turbulators (see Figure 7–3) has a very similar behavior of the continuous V-shaped turbulators (Chapter 6). In the cavity of the segmented V-shaped the normal velocity the lower wall ( $y^* = -1$ ) and positive in the upper wall ( $y^* = +1$ ) denoting a flow inward the cavity. However, at the crest plane the velocity has opposite sign, in fact this indicated ejections. The normal velocity in the center of the channel is very low because the flow is mainly passing through the center of the channel. The lowest normal velocity magnitude is found for  $p/e = 1$ . For both configuration (aligned

and staggered) the  $p/e = 3$  case is the one with the highest normal velocity profile along the normal distance.

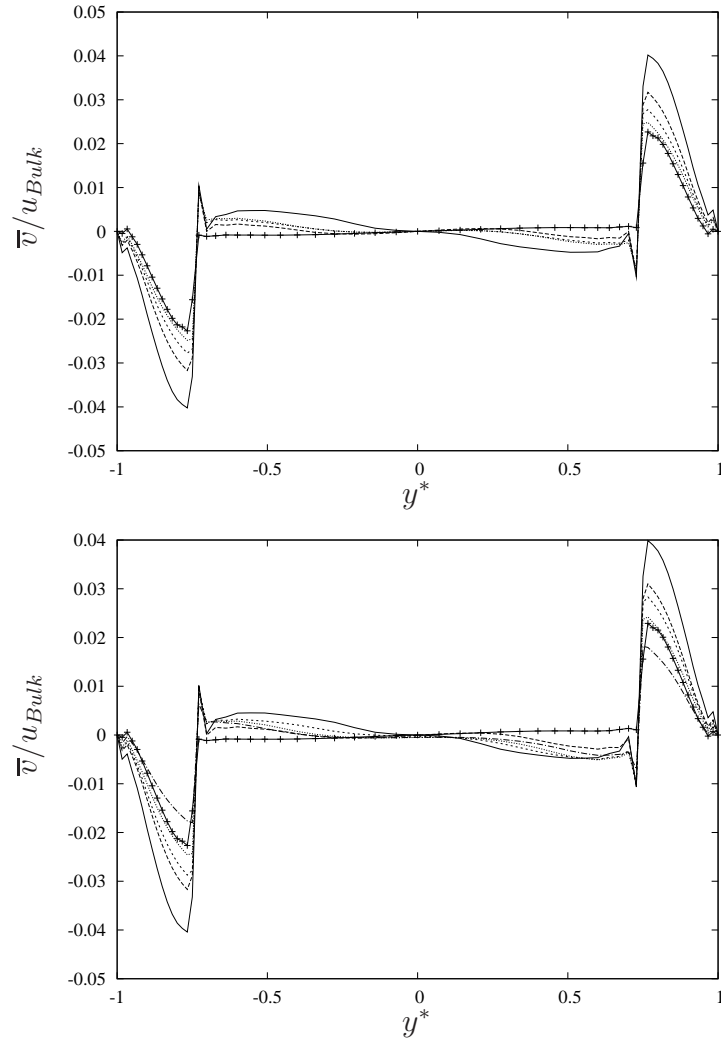


**Figure 7–3: Normal Average Velocity profile distribution for Segmented V-Shaped turbulators. Upper: Aligned, Lower: Staggered.**

(+)  $p/e = 1$ , (—)  $p/e = 3$ , (----)  $p/e = 5$ , (-·-·-)  $p/e = 8$ , (···)  $p/e = 10$ , (---)  $p/e = 15$

Figure 7-4 shows a channel with segmented V-shaped turbulator with velocity streamtracer. This figure is very helpful to understand the behavior of the fluid in this channel. Flow from the center of the channel enters into the cavities. Three streams are formed, one going through the gap of the segmented V-shaped turbulators. The other two streams follow the inclination of the segmented V-shaped turbulators. The secondary motion generated when the fluid hits the side walls of

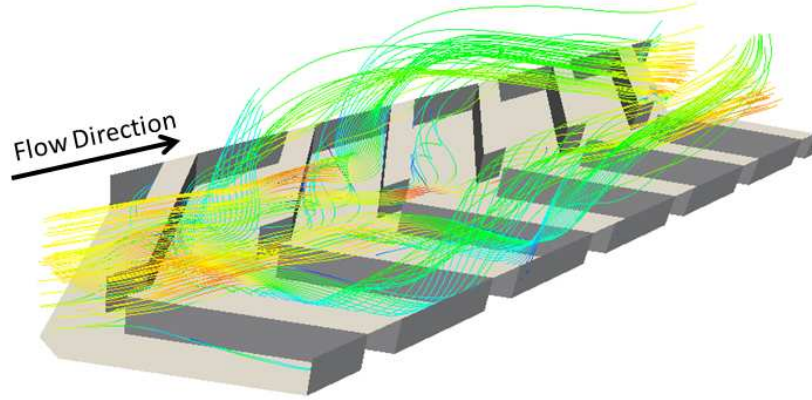


**Figure 7–4: Velocity Streamtracer in the Streamwise Direction for Segmented V-Shaped turbulators.**

the channel are also in this channel. A fluid recirculation is observed at the trailing edge of the turbulators.

A color contour velocity of the segmented V-shaped turbulators is presented in the Figure 7–5 in which the red and blue color represent the highest and lower magnitude of velocities, respectively. The top view of the contour is taken near the crest plane of the turbulators. In the gap of the segmented V-shaped high velocities in the streamwise direction can be observed (Fig 7–5 (A)) and correspond to the inward motion (blue region can be observe in the Figure 7–5 (B)). Two streams (red-blue Fig. 7–5 (C)) follow the rib inclination.

## 7.2 Root Mean Square (RMS) Velocity

Figure 7–6 shows the RMS streamwise velocity for the aligned and staggered configuration of all  $p/e$  cases. Higher values of RMS are observed at the crest plane due to the flow ejections generated in the turbulators leading edge. The center of the channel presents the lowest values of RMS. The case with the pitch to height ratio  $p/e = 3$  both for aligned and staggered configurations present the highest streamwise velocity RMS.

The RMS normal velocity are presented in Figure 7–7 in which is possible observe that the minimum RMS normal velocity are in the center of the channel and in the two walls ( $y^* = -1$  and  $y^* = +1$ ).

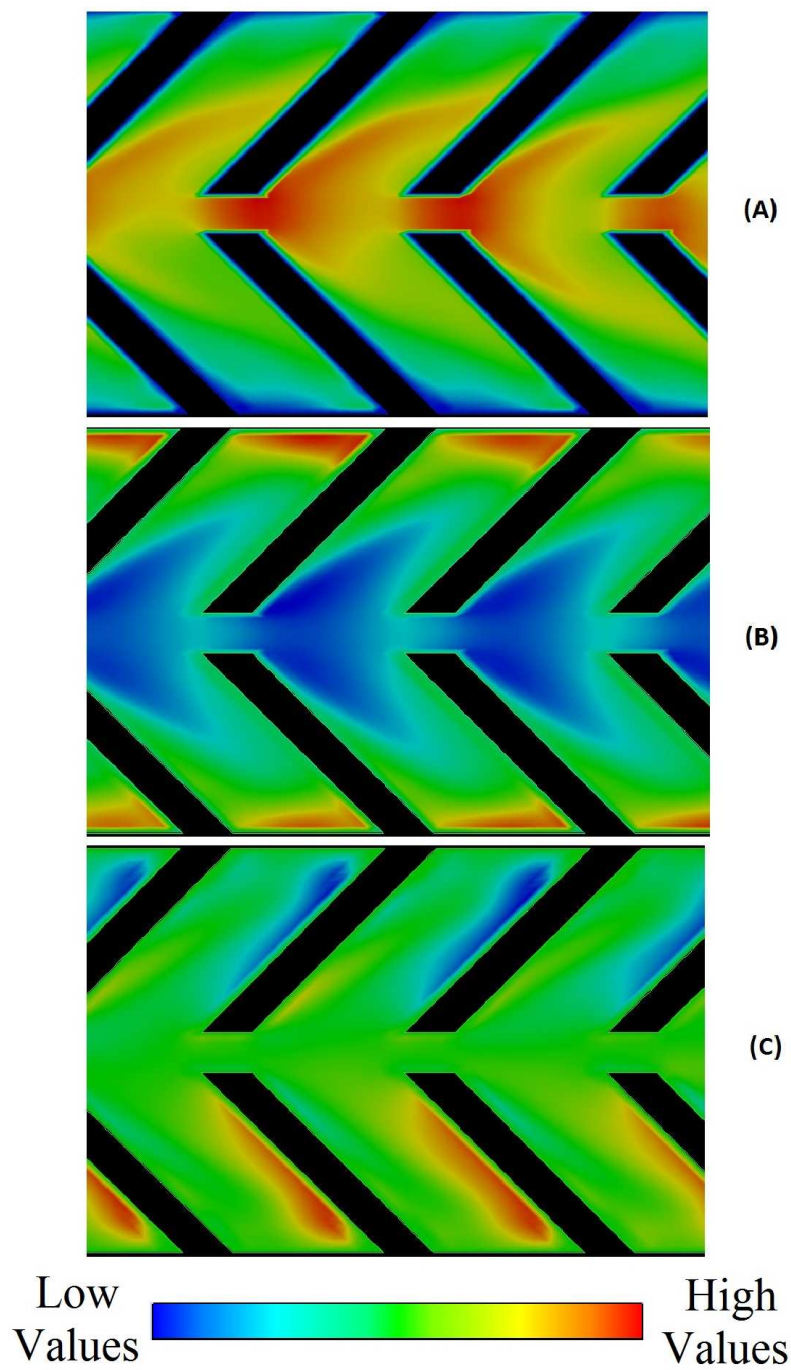
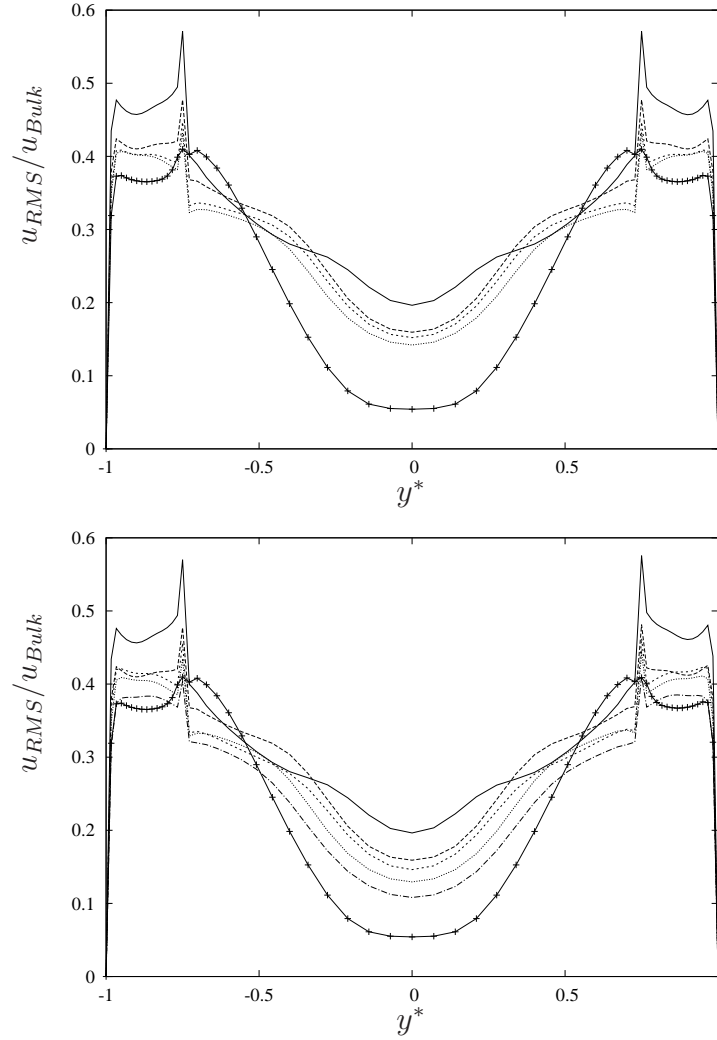


Figure 7-5: Velocity contour for the three direction in the  $p/e = 3$  configuration for Segmented V-Shaped turbulators. (A) Streamwise Average Velocity. (B) Normal Average Velocity. (C) Spanwise Average Velocity.



**Figure 7–6: Streamwise Velocity RMS average in time for Segmented V-Shaped turbulators. Upper: Aligned, Lower: Staggered.**

(+)  $p/e = 1$ , (—)  $p/e = 3$ , (----)  $p/e = 5$ , (-·-·-)  $p/e = 8$ , (···)  $p/e = 10$ , (- - -)  $p/e = 15$

From Figure 7–7 the RMS normal velocity start to increase in the cavity of the segmented V-shaped turbulators to reach a maximum right above the crest plane of the turbulators ( $y^* > \pm 0.75$ ). This increase in the region after the crest plane of the turbulators is due to the secondary vortices of opposite directions in this area. The  $p/e = 3$  case presents the maximum RMS normal velocity while the  $p/e = 1$  case has the minimum RMS normal velocity. The results present a similar behavior for the aligned and staggered configurations.

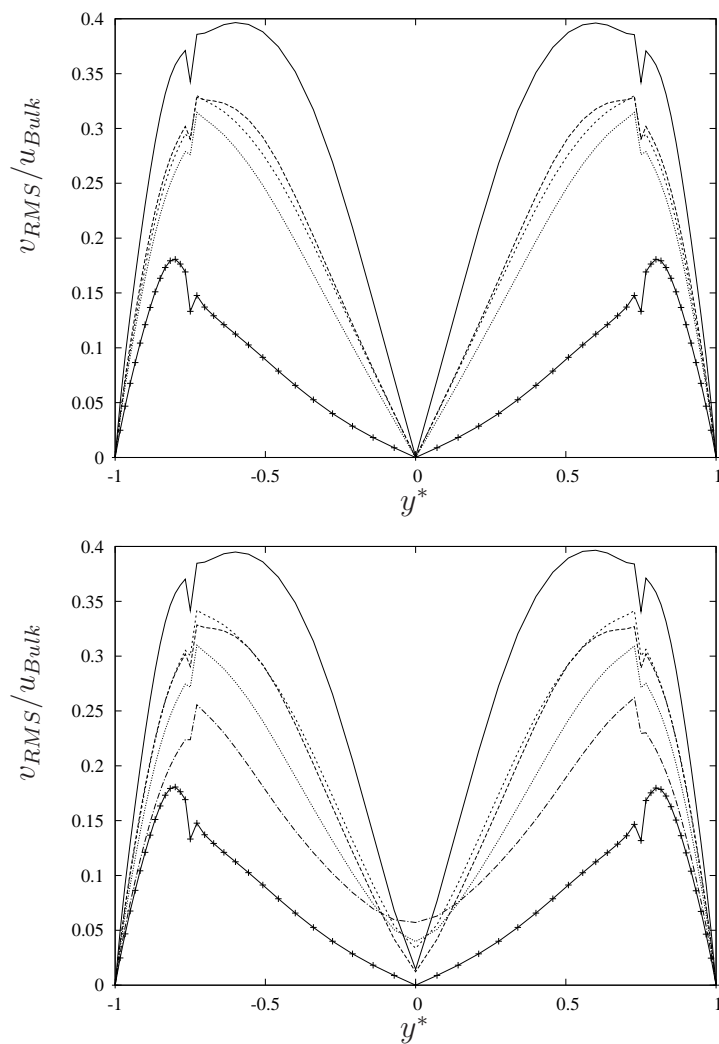
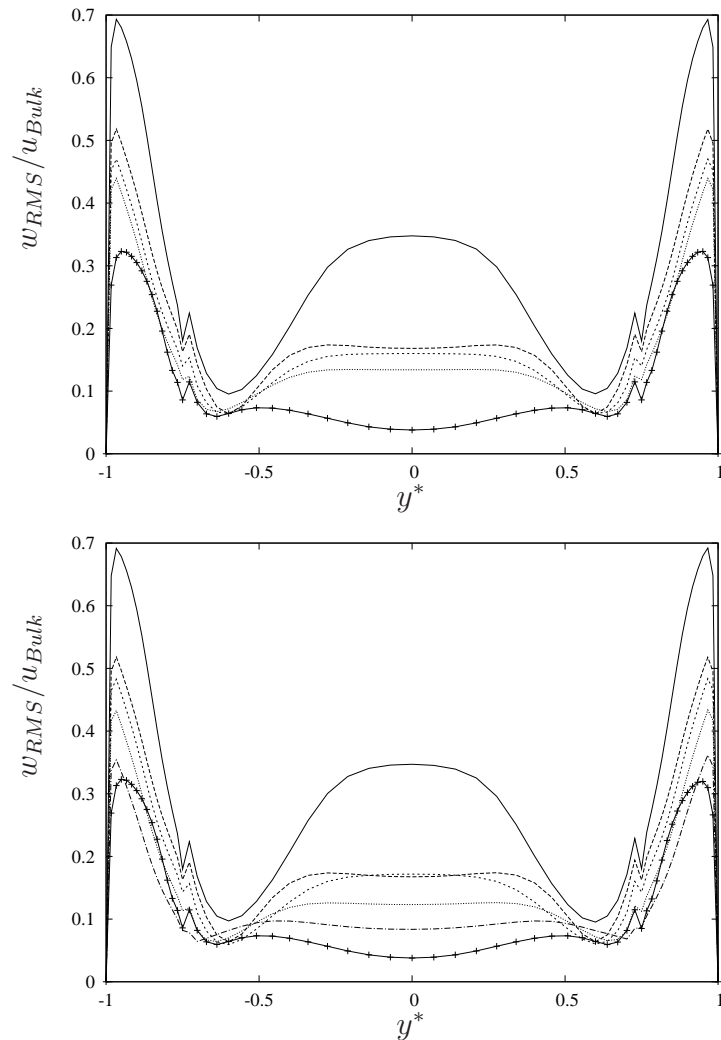


Figure 7–7: Normal Velocity RMS average in time for Segmented V-Shaped turbulators. Upper: Aligned, Lower: Staggered.

Figure 7–8 shows the RMS spanwise velocity along the normal direction. Close to the lower and upper wall the RMS spanwise velocity has a significant increase. This phenomenon has been observed before for the V-shaped turbulators and is due for the flow entering into the cavity and moving towards the side walls. The fluid follows the segmented V-shaped turbulators inclination and the major velocities are in the streamwise and spanwise direction.



**Figure 7–8: Spanwise Velocity RMS average in time for Segmented V-Shaped turbulators. Upper: Aligned, Lower: Staggered.**

(+)  $p/e = 1$ , (—)  $p/e = 3$ , (----)  $p/e = 5$ , (-·-·-)  $p/e = 8$ , (···)  $p/e = 10$ , (---)  $p/e = 15$

### 7.3 Mean Temperature

Mentioned before the thermal boundary condition for the lowest wall (hot wall) is  $\tilde{T} = -1$  and for the upper wall (cold wall) is  $\tilde{T} = +1$ .

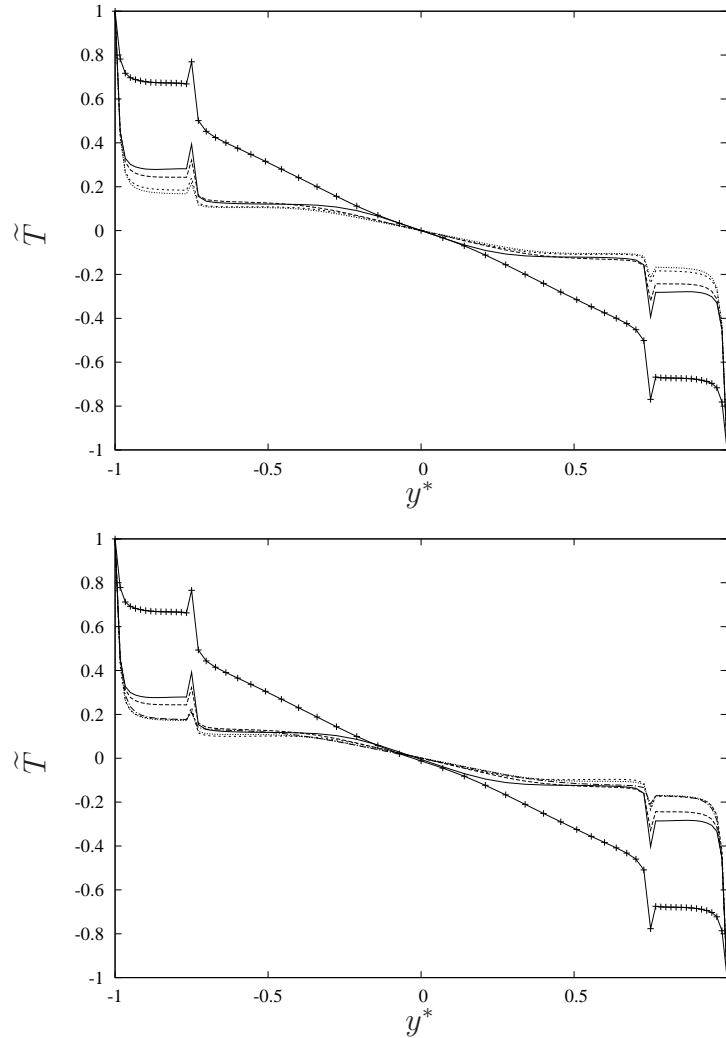


**Figure 7–9: Temperature profile distribution for Segmented V-Shaped turbulators. Upper: Aligned, Lower: Staggered.**

(+)  $p/e = 1$ , (—)  $p/e = 3$ , (----)  $p/e = 5$ , (-·-·-)  $p/e = 8$ , (···)  $p/e = 10$ , (---)  $p/e = 15$

The distribution of the temperature profile along the normal direction for the segmented V-shaped turbulators are shown in Figure 7–9. The behavior of the temperature profile for the aligned and staggered configurations of the segmented V-shaped turbulators are very similar to the temperature profile of the V-shaped turbulators. The segmented V-shaped shows a high gradient temperature at the

walls. The temperature is constant in the cavity  $-1 < y^* < -0.75$  for the lower wall and  $+0.75 < y^* < +1$  for the upper wall. The behavior of the temperature in the center of the channel is linear with a larger gradient for  $p/e = 1$ , being the heat flux dominated by conduction. For larger  $p/e$  the temperature gradient decrease.

## 7.4 Root Mean Square (RMS) Temperature

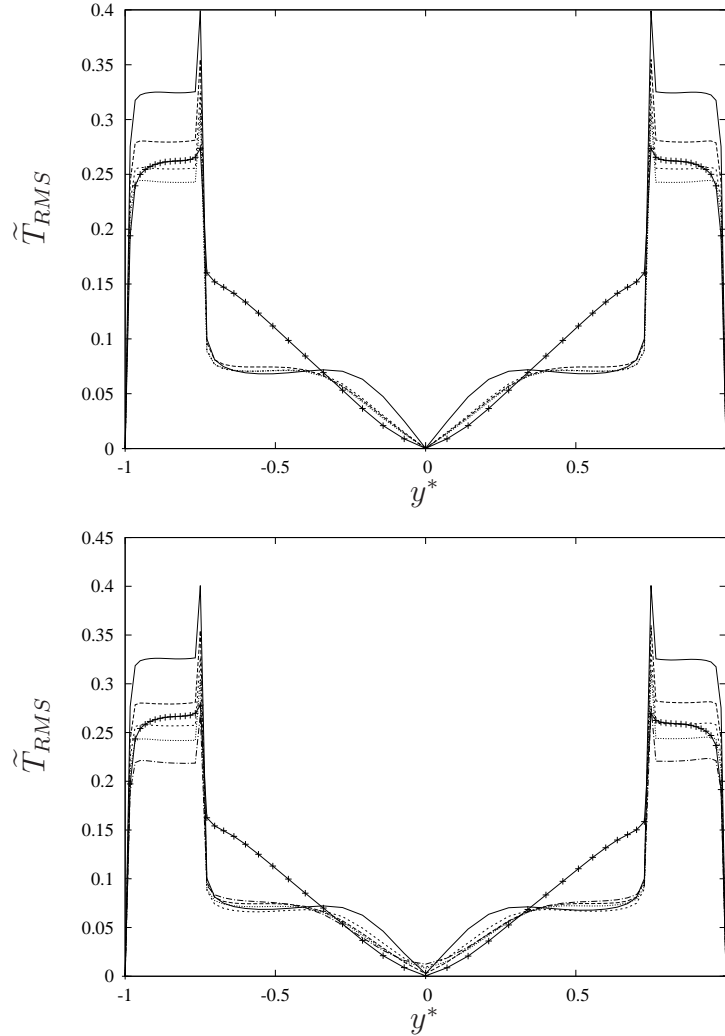


**Figure 7–10: Temperature RMS average in time for Segmented V-Shaped turbulators. Upper: Aligned, Lower: Staggered.**

(+)  $p/e = 1$ , (—)  $p/e = 3$ , (----)  $p/e = 5$ , (-·-·-)  $p/e = 8$ , (···)  $p/e = 10$ , (- - -)  $p/e = 15$

In the Figure 7–10 the temperature RMS is shown at the center of the channel where the minimal RMS temperature (the area which is presented has the average temperature) is found. The upper and lower walls of the channel present the largest

temperature RMS. High temperature RMS is observed also at the crest plane of the segmented V-shaped turbulators. The  $p/e = 3$  case is the one with the highest RMS temperature for both configuration (aligned and staggered).

## 7.5 Nusselt Number

The Nusselt number for the aligned and staggered configuration is shown in the Figure 7–11. The equation used to calculate the Nusselt number in the channel is the equation 4.2. In this figure it is seen that the  $p/e = 3$  case has the highest Nusselt number for both configuration. The  $p/e = 3$  case has the largest heat transfer compared to all the other cases. For the aligned case the Nusselt number is equal to 84.27 and for the staggered case the Nusselt number is 84.42. The difference is small and within numerical uncertainty.

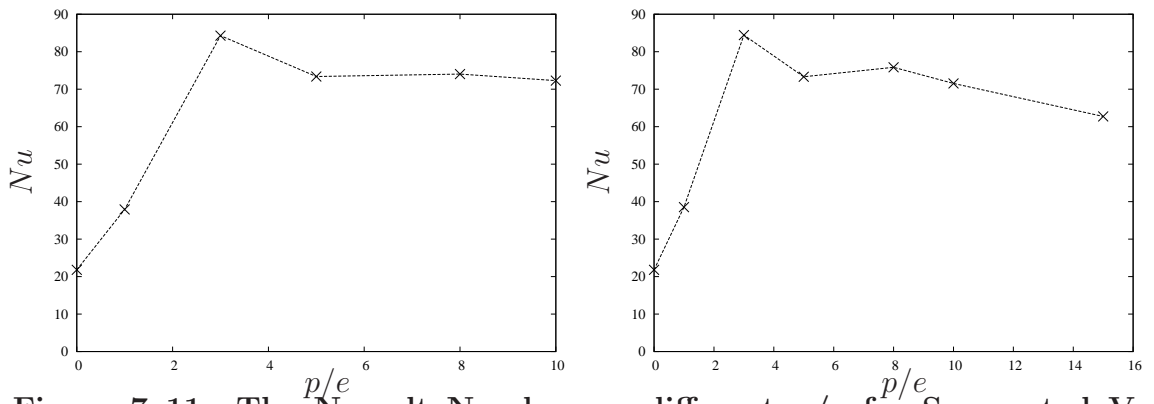


**Figure 7–11: The Nusselt Number on different  $p/e$  for Segmented V-Shaped turbulators. Left: Aligned, Right: Staggered**

## 7.6 Frictional Drag and Form Drag

The total drag is the sum of the form drag (Eq. 4.4) and the frictional drag (Eq. 4.3). The total drag and its component are plotted in the Figure 7–12. For both configurations (aligned and staggered) the case who present the highest total drag is the  $p/e = 3$ . For the aligned configuration the total drag is 0.0913 and for the staggered configuration is 0.0910.

The last paragraph shows that the segmented V-shaped turbulators are better compared with the other cases studied before. Using the segmented V-shaped

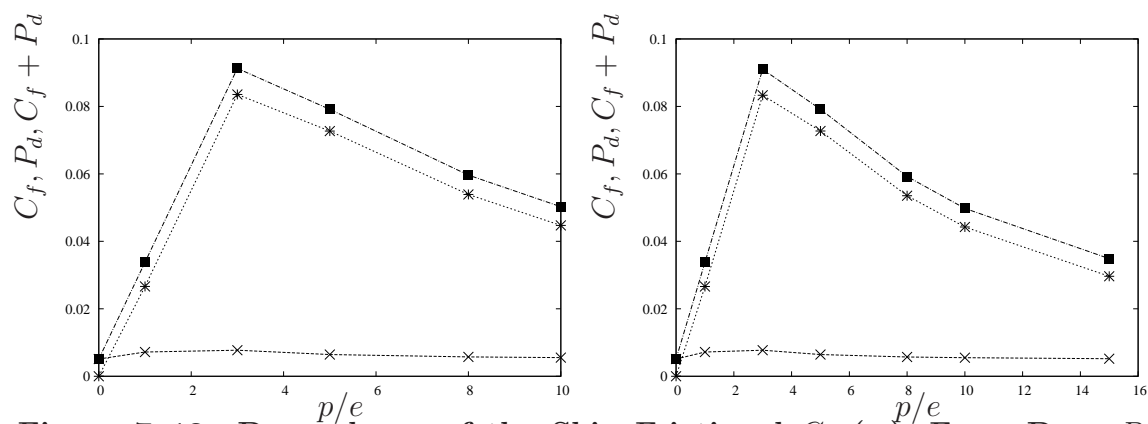


**Figure 7–12: Dependence of the Skin Frictional  $C_f$  ( $\times$ ), Form Drag  $P_d$  ( $*$ ) and Total Drag  $C_f + P_d$  ( $\blacksquare$ ) on different  $p/e$  for Segmented V-Shaped turbulators. Left: Aligned, Right: Staggered**

turbulators we have the advantage of having a higher Nusselt number (that means a higher heat transfer) with a lower total drag. That is due for the gap used in the segmented V-shaped turbulators. These gaps help to decrease the form drag by reducing the pressure between the leading edge and the trailing edge of the segmented V-shaped turbulators.

## CHAPTER 8

### CONCLUSION AND FUTURE WORK

Numerical simulations have been performed to analyze heat transfer for different configurations of turbulators. These configurations of the turbulators were: square bars (Fig. 5–1), V-shaped (Fig. 6–1) and segmented V-shaped (Fig. 7–1). For all the geometries considered the most efficient configuration was identified. The simulations performed in this study analyze aligned and staggered rib turbulators in a duct. The result shows clearly that the staggered configuration presents an improved heat and mass transfer. Similarly, Orlandi & Leonardi (2006) showed that the staggered roughness induces stronger flow ejection in the cavity compared to aligned configuration [6].

The Nusselt number indicates the intensity of the heat transfer. Among the cases here presented, the maximum Nusselt numbers:

- $Nu = 36.62$  for square bars turbulators  $p/e = 10$  (see Fig. 5–10);
- $Nu = 77.82$  for V-shaped turbulators  $p/e = 3$  (see Fig. 6–13); and,
- $Nu = 84.42$  for segmented V-shaped turbulators  $p/e = 3$  (see Fig. 7–11).

A bar chart comparison of the Nusselt number is shown in Figure 8–1. The V-shaped turbulators is the configuration with the highest Nusselt number among those considered here. The segmented V-shaped turbulators increase the heat transfer 7.82% more than the continuous V-shaped turbulators, and 56.6% more than the square bars turbulators.

The total drag is the sum of frictional and form drag. Heat transfer augmentation is correlated with drag increase. The form drag for the square bars, V-shaped

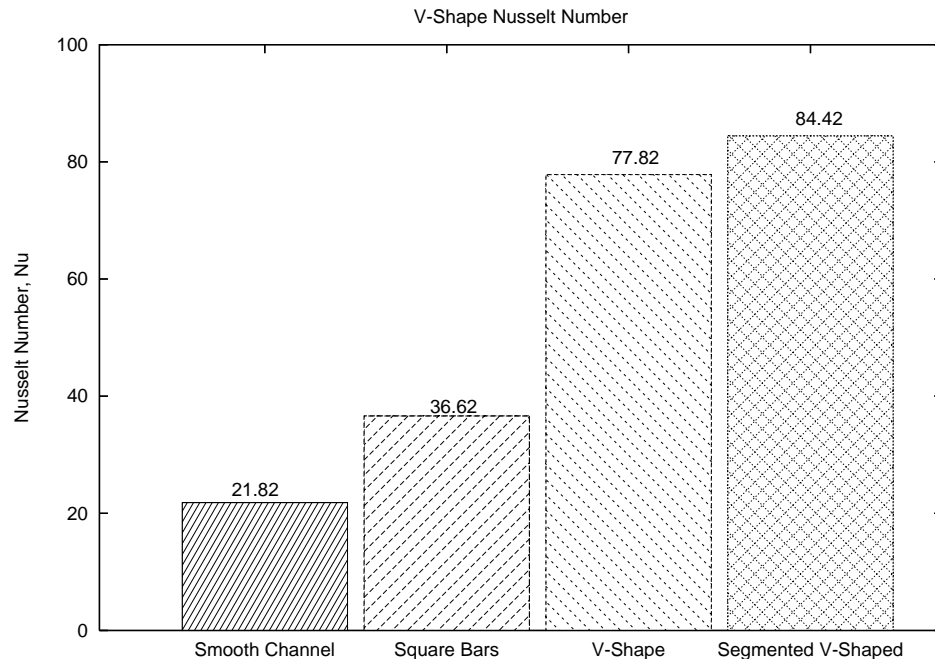


**Figure 8–1: Nusselt Number Comparison**

and segmented V-shaped turbulators (aligned and staggered) are shown in Figure 8–2. The segmented V-shaped turbulators present a form drag smaller than the square bars and the V-shaped turbulators. In the aligned and staggered configuration of V-shaped turbulators present the highest form drag in  $p/e = 3$ . On the other hand, the segmented V-shaped turbulators have smaller form drag for the same pitch height ratio.

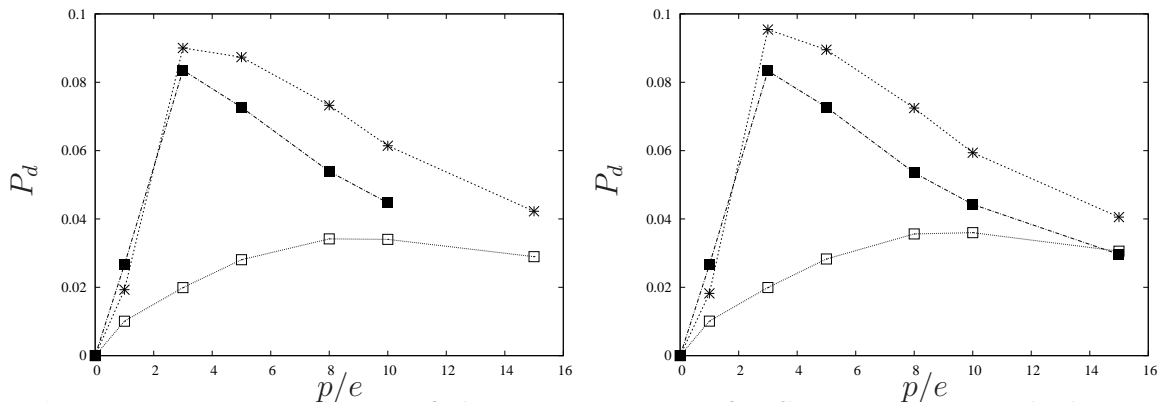


**Figure 8–2: Dependence of the Form Drag  $P_d$  for Square Bars Turbulators (□), V-Shaped Turbulators (\*) and Segmented V-Shaped Turbulators (■) on different  $p/e$ . Left: Aligned, Right: Staggered**

Compared with the form drag, the frictional drag for the segmented V-shaped turbulators is higher than that for the V-shaped turbulators (Fig. 8–3). This is due to the high velocity stream of fluid which flows through the gap of the segmented V-shaped turbulators. In Figure 8–3 it is possible to observe that for the square bars turbulators the skin friction has a negative contribution to the total drag. The negative skin friction was due to the high recirculation (and reverse flow) in the cavity area of the square bars turbulators.

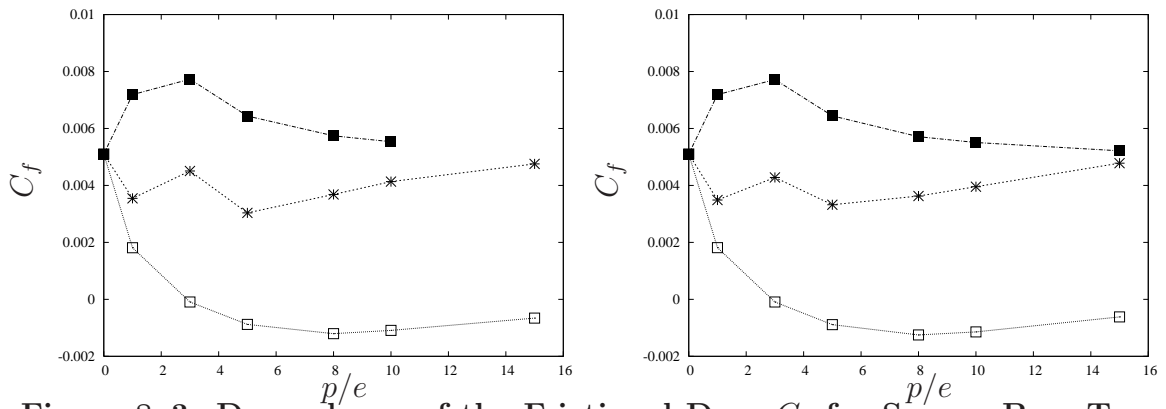


**Figure 8–3: Dependence of the Frictional Drag  $C_f$  for Square Bars Turbulators ( $\square$ ), V-Shaped ( $*$ ) and Segmented V-Shaped ( $\blacksquare$ ) on different  $p/e$ . Left: Aligned, Right: Staggered**

The total drag relative to square bars, V-shaped and the segmented V-shaped turbulators is shown in the Figure 8–4. The form drag is the larger contribution to the total drag, therefore the configurations presenting higher total drag are those maximizing form drag. For the aligned and staggered configurations, V-shaped and segmented V-shaped present the highest total drag the  $p/e = 3$ . In summary, the segmented V-shaped turbulators present the highest heat transfer among the cases here considered and lower drag than V-shaped turbulators.

A study of V-shaped turbulators and inclined ribs with a pitch ratio of  $p/e = 5$  and with different angles (see Appendix B) have been performed. In this study, the V-shaped turbulators  $45^\circ$  was found the one with the highest Nusselt number which means that this case had the highest heat transfer (Fig. B–10). For this case a highest total drag was also found (Fig. B–11). It will be an interesting study, to

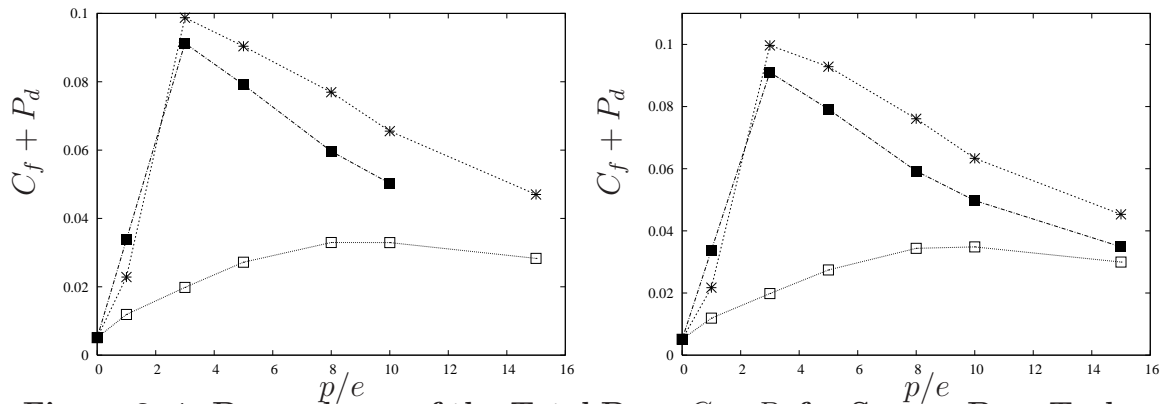


**Figure 8–4: Dependence of the Total Drag  $C_f + P_d$  for Square Bars Turbulators ( $\square$ ), V-Shaped ( $*$ ) and Segmented V-Shaped ( $\blacksquare$ ) on different  $p/e$ . Left: Aligned, Right: Staggered**

compare these different cases with the segmented V-shaped turbulators at different angles.

An interesting thing to do in future would be the analysis of different cases of turbulators varying the height of the turbulators, this will create cases more similar to the real applications. It will also be good to study the different situations in which the turbulators have more than one gap along the turbulators and observe the behavior of the heat transfer with these gaps. LES and DNS simulations for the different cases study in here will be interesting cases to assess the approximation and validity of RANS.

# APPENDICES

## APPENDIX A

The Navier-Stokes equation are needed to model the behavior of a turbulent flow. These equations are obtain for the equation of motion of an incompressible fluid

$$\frac{\partial u_i}{\partial x_i} = 0 \quad (\text{A.1})$$

$$\frac{\partial u_i}{\partial t} + \rho u_j \frac{\partial u_i}{\partial x_j} = \frac{1}{\rho} \frac{\partial}{\partial x_j} \sigma_{ij} \quad (\text{A.2})$$

In the equation (A.2) the term  $\sigma_{ij}$  is the stress tensor. For a Newtonian fluid the stress tensor term is

$$\sigma_{ij} = -p\delta_{ij} + 2\mu s_{ij} \quad (\text{A.3})$$

For the equation (A.3), the Kronecker delta is a term which have to values:

$$\delta_{ij} = \begin{cases} 0 & \text{if } i \neq j \\ 1 & \text{if } i = j \end{cases}$$

The  $p$  is the hydrodynamics pressure and  $\mu$  is the dynamic viscosity. The term  $s_{ij}$  is the rate of strain and is define by

$$s_{ij} = \frac{1}{2} \left( \frac{\partial u_i}{\partial x_j} + \frac{\partial u_j}{\partial x_i} \right)$$

Now, if the equation (A.3) is introduced in the equation (A.2) and knowing that exists continuity in the system the *Navier – Stokes equations* for a steady state system are

$$u_j \frac{\partial u_i}{\partial x_j} = -\frac{1}{\rho} \frac{\partial p}{\partial x_i} + \nu \frac{\partial^2 u_i}{\partial x_j \partial x_j} \quad (\text{A.4})$$

The constant  $\nu$  is the kinematic viscosity ( $\nu = \mu/\rho$ ). The velocity  $u_i$  is decomposed into the mean velocity  $\bar{u}_i$  and the velocity fluctuation  $u'_i$ , this is called the Reynolds decomposition ( $u_i = \bar{u}_i + u'_i$ ). By this concept it is possible to obtain the average Navier-Stokes equations.

There is some important concept to know to determine the average Navier-Stokes equations. Applying the Reynolds decomposition to the continuity equation (A.1) is

$$\frac{\partial u_i}{\partial x_i} = \frac{\partial(\bar{u}_i + u'_i)}{\partial x_i} = \frac{\partial \bar{u}_i}{\partial x_i} + \frac{\partial u'_i}{\partial x_i} = 0 \quad (\text{A.5})$$

Applying the ensemble average to the instantaneous equation it is obtained that

$$\overline{\frac{\partial u_i}{\partial x_i}} = \frac{\partial \bar{u}_i}{\partial x_i} \quad (\text{A.6})$$

Now, when is applied the ensemble average to the (A.4) the term  $\overline{u_i u_j}$  arises in the equation. The following equation shows that

$$\overline{u_j \frac{\partial u_i}{\partial x_j}} = -\frac{1}{\rho} \frac{\partial \bar{p}}{\partial x_i} + \nu \overline{\frac{\partial^2 u_i}{\partial x_j \partial x_j}} \quad (\text{A.7})$$

Similar to the process done in the (A.6), the average component can enter in the differential component, like is shown in the next equation

$$\frac{\partial \overline{u_i u_j}}{\partial x_j} = -\frac{1}{\rho} \frac{\partial \bar{p}}{\partial x_i} + \nu \frac{\partial^2 \bar{u}_i}{\partial x_j \partial x_j} \quad (\text{A.8})$$

To solve the component of  $\overline{u_i u_j}$  is used a correlated variables in which the average of the product is computed. This is shows in the following process

$$\overline{u_i u_j} = \overline{(\overline{u_i} + u'_i)(\overline{u_j} + u'_j)} = \overline{u_i u_j} + \overline{u'_i \overline{u_j}} + \overline{\overline{u_i} u'_j} + \overline{u'_i u'_j} = \overline{u_i} \overline{u_j} + \overline{u'_i u'_j}$$

Knowing that  $\overline{u_i u_j} = \overline{u_i} \overline{u_j} + \overline{u'_i u'_j}$  and introduce this in the equation (A.8) the Reynold Average Navier-Stokes equations obtain are

$$\frac{\partial(\overline{u_i} \overline{u_j} + \overline{u'_i u'_j})}{\partial x_j} = -\frac{1}{\rho} \frac{\partial \overline{p}}{\partial x_i} + \nu \frac{\partial^2 \overline{u_i}}{\partial x_j \partial x_j} \quad (\text{A.9})$$

$$\rho \frac{\partial \overline{u_i} \overline{u_j}}{\partial x_j} = -\frac{1}{\rho} \frac{\partial \overline{p}}{\partial x_i} + \rho \frac{\partial^2 \overline{u_i}}{\partial x_j \partial x_j} - \frac{\partial \overline{\rho u'_i u'_j}}{\partial x_j} \quad (\text{A.10})$$

$$\rho \frac{\partial \overline{u_i} \overline{u_j}}{\partial x_j} = -\frac{1}{\rho} \frac{\partial \overline{p}}{\partial x_i} + \rho \frac{\partial^2 \overline{u_i}}{\partial x_j \partial x_j} + \frac{\tau_{ij}}{\partial x_j} \quad (\text{A.11})$$

In the equation of Reynold Average Navier-Stokes Eq. (A.11) the term  $\partial \overline{u_i} \overline{u_j} / \partial x_j$  represent the mean transport of the fluctuation momentum by the turbulent velocity fluctuations. The term  $\tau_{ij} = \overline{\rho u'_i u'_j}$  represent the contribution of the turbulent motion in the mean stress tensor and it's call the Reynolds stress tensor. To solve this term it is needed a turbulent model, that is the reason to choose the realizable  $k - \epsilon$  model for the RANS equations.

## APPENDIX B

Direct numerical simulations of a turbulent channel flow have been performed. The channel have different turbulators on the upper and the lower wall in the staggered position. The Reynolds number used is  $Re = U_b H / \nu$  equal to 10,400, where  $U_b$  is the bulk velocity,  $\nu$  is the kinematic viscosity and  $H$  is the channel half height. For this Reynold number the Prandtl number is defined by  $Pr = 1$ . The channel is analyzed on a wide range of  $p/e = 5$  ( $p$  is the pitch and  $e$  is the height of the roughness). The analysis of the different cases are performed using Fluent with the RANS (Reynolds Average Navier Stokes) model. The purpose of this work is obtain the configuration that maximizing the heat transfer in the turbulent channel flow. The purpose of this chapter is analyze different turbulators configuration and observe the better which has the highest heat transfer.

### B.1 Flow Configuration

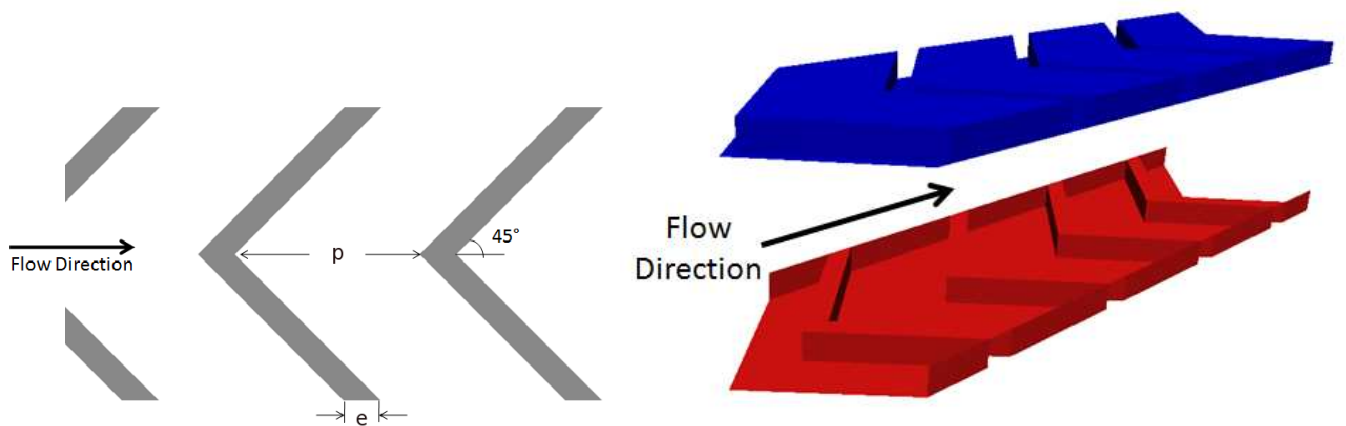
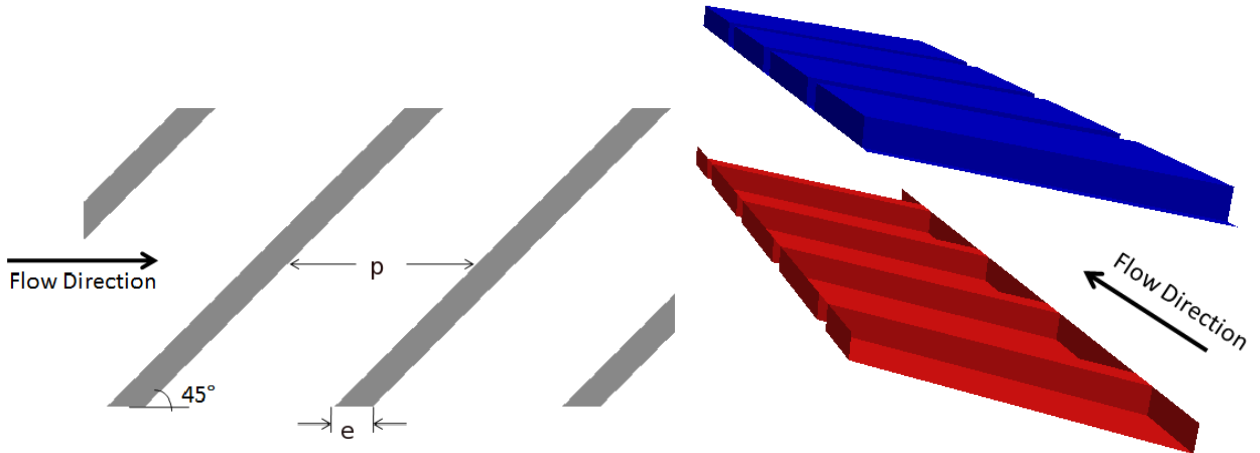


Figure B-1: Left: V-Shaped Turbulators Sketch. Right: 3-D V-Shaped Turbulators Configuration.

Reynolds Averaged Navier Stokes simulations of the turbulent flow in a channel with turbulators on the walls have been performed. V-shaped turbulators with an angle of  $45^\circ$  (see Figure B-1),  $60^\circ$  and  $75^\circ$  and square bars inclined at  $45^\circ$  (see Figure B-2),  $60^\circ$  and  $90^\circ$  with respect to the flow direction were considered. The computational box is  $6H \times 2H \times 2H$  in the streamwise, normal and spanwise direction, respectively. The pitch to height ratio  $p/e$  is equal to 5 and the height of the turbulators is  $e/H = 0.25$  ( $H$  is the half-height of the channel). The grid has  $128 \times 60 \times 64$  points in the streamwise, normal, and spanwise distance respectively. In the normal direction a non uniform grid was, 15 points were clustered in the roughness layer.



**Figure B-2: Left: Square Bars Inclined Turbulators Sketch. Right: 3-D Square Bars Inclined Turbulators Configuration.**

Periodic boundary conditions are applied in the streamwise ( $x$ ) and spanwise ( $z$ ) direction. No-slip conditions are applied in the wall-normal direction and at the walls.

## B.2 Mean Flow

The streamwise velocity averaged in  $x$ ,  $z$  and time is shown in Figure B-3 for V-shaped turbulators with an angle of  $45^\circ$ ,  $60^\circ$  and  $75^\circ$  and square bars turbulators inclined at  $45^\circ$ ,  $60^\circ$  and  $90^\circ$  with respect to the flow direction. The square bars turbulators inclined at  $45^\circ$  present the maximum value of the streamwise velocity

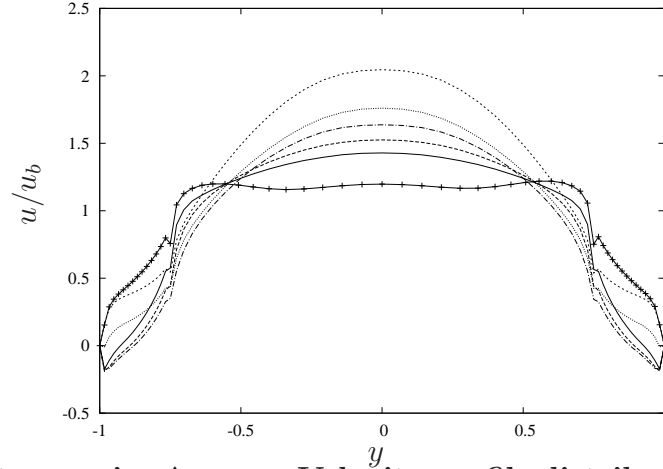


**Figure B-3: Streamwise Average Velocity profile distribution for different ribs turbulators:** (+) *V - Shaped 45°*, (—) *V - Shaped 60°*, (----) *V - Shaped 75°*, (-----) *Inclined Ribs 45°*, (···) *Inclined Ribs 60°*, (---) *Inclined Ribs 90°*.

compared with all configuration. Meanwhile the V-shaped turbulators of 45° has the highest values in the streamwise average velocity in the cavity area compared with all configuration. This is good because promote heat transfer in the turbulators area.

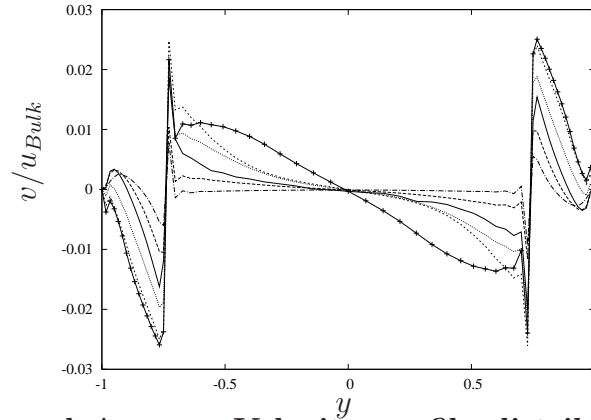


**Figure B-4: Normal Average Velocity profile distribution for different ribs turbulators:** (+) *V - Shaped 45°*, (—) *V - Shaped 60°*, (----) *V - Shaped 75°*, (-----) *Inclined Ribs 45°*, (···) *Inclined Ribs 60°*, (---) *Inclined Ribs 90°*.

The normal velocity averaged in  $x, z, t$  is shown in the Figure B-4. The V-shaped turbulator of 45° configuration has the maximum values of the normal average velocity in the roughness area. This means that in this configuration the largest amount of fluid enters into the cavity. This increases the heat transfer because the

fluid enters into the cavity and help in the remotion of heat. For the V-shaped turbulator of  $45^\circ$  configuration has the highest value of normal average velocity after the crest plane ( $y > -0.75, y < 0.75$ ) when compared with the other configurations. This high velocity is created by the secondary motion generate for the flow ejected in the turbulators area. This also is helpful in the heat removal process.

### B.3 Root Mean Square (RMS) Velocity

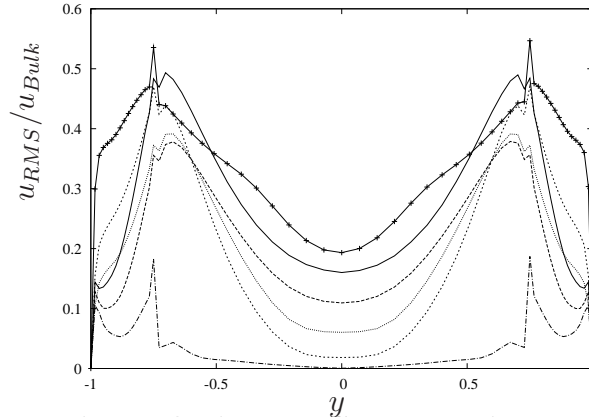


**Figure B-5: Streamwise Velocity RMS average in space for different ribs turbulators.** (+) *V- Shaped*  $45^\circ$ , (—) *V- Shaped*  $60^\circ$ , (----) *V- Shaped*  $75^\circ$ , (.....) *Inclined Ribs*  $45^\circ$ , (-·-·) *Inclined Ribs*  $60^\circ$ , (---) *Inclined Ribs*  $90^\circ$ .

In Figure B-5 the RMS for the streamwise velocity is shown. V-shaped turbulators present a high streamwise velocity RMS. The highest corresponds to the V-shaped turbulators with an angle of  $45^\circ$ . The lowest value of the streamwise velocity RMS is observed in the square bars inclined of  $90^\circ$ . The higher RMS is found at the crest plane for all the geometrical configurations ( $y = \pm 0.75$ ). At the crests plane, in fact, the velocity varies from 0 at the crests plane to a maximum value in the center of the cavity. Fluid particles undergoes favorable and adverse pressure gradient. In the middle of the channel the streamwise velocity RMS is the lowest. In fact, the effect of roughness is stronger near the crests plane and vanish farther away from it. Each roughness geometry has a different effect on the overlying flow. The weakest is found for transverse square bars. These particular geometries do not have the secondary motions that are present in the V-Shape configurations.

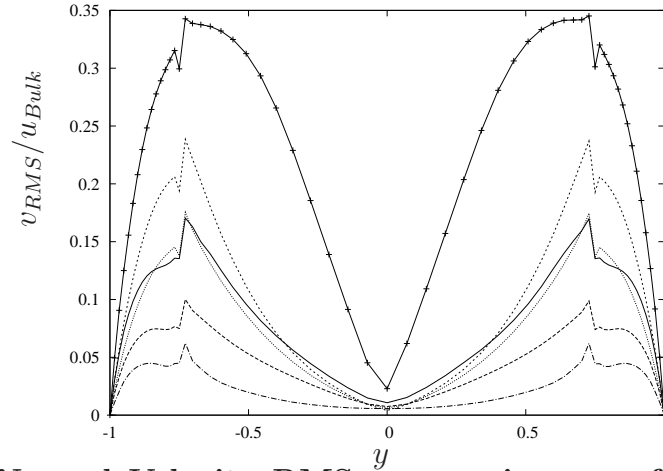


**Figure B-6: Normal Velocity RMS average in space for different ribs turbulators.** (+) *V- Shaped 45°*, (—) *V- Shaped 60°*, (----) *V- Shaped 75°*, (.....) *Inclined Ribs 45°*, (-.-) *Inclined Ribs 60°*, (---) *Inclined Ribs 90°*.

For the normal wall velocity RMS (Fig. B-6) shows a peak in the crest plane of the turbulators. This is due to the ejections at the crest plane of the turbulators. The V-shaped turbulator of 45° has the highest value of the normal RMS velocity compare with all configurations. The velocity RMS decreases by moving towards the center of the channel.

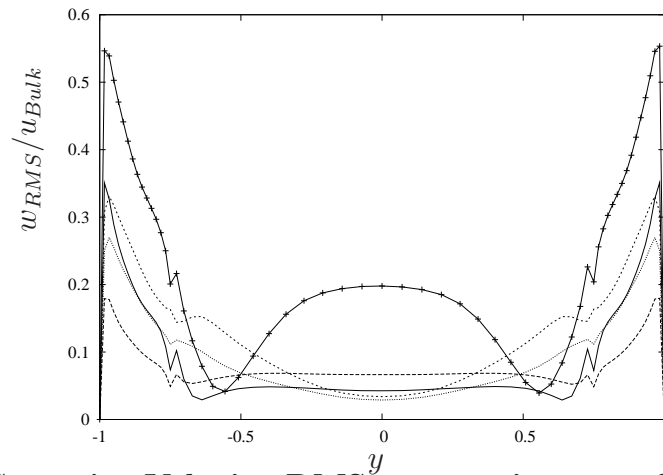


**Figure B-7: Spanwise Velocity RMS average in space for different ribs turbulators.** (+) *V- Shaped 45°*, (—) *V- Shaped 60°*, (----) *V- Shaped 75°*, (.....) *Inclined Ribs 45°*, (-.-) *Inclined Ribs 60°*, (---) *Inclined Ribs 90°*.

The Figure B-7 shows the RMS velocity for the spanwise direction. The highest spanwise RMS velocities are near the walls. The V-shaped turbulators with a 45° angle present the highest spanwise velocity RMS. In fact, for V-shaped turbulators,

the flow enters into the cavities and forms two streams which follow the inclination of the V-shaped turbulators and then the fluid moves in the spanwise direction. At the center of the channel the ejections from the upper and lower wall merge and the fluid converges in the streamwise direction towards the center of the channel. Therefore, at the center of the channel high streamwise velocity RMS is also observed.

## B.4 Mean Temperature

Figure B–8 shows the temperature profiles along the normal direction. To calculate the non-dimensional temperature profile a bulk temperature is used the Equation 4.1. It is possible observe the effect of the different turbulators in the temperature profile. In the crest plane of the turbulators the temperature has a small increase because the average temperature has the temperature of the cavity area in this area and the temperature of the crest plane of the turbulators. In the middle of the channel the temperature have a smooth behavior in all configurations. The configuration of V-shaped turbulator of  $45^\circ$  present the highest temperature gradient in the walls.

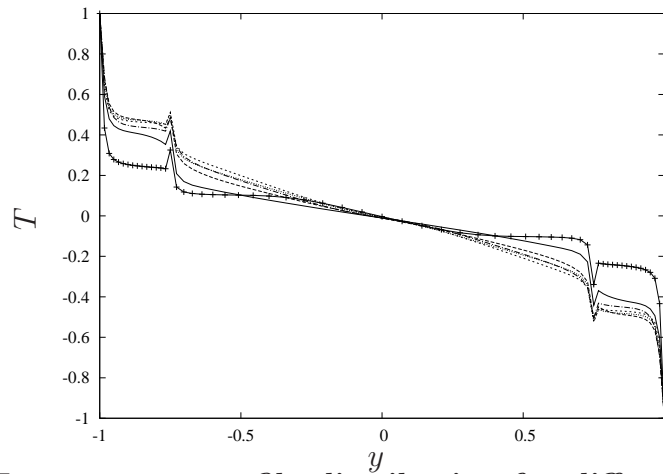


**Figure B–8: Temperature profile distribution for different ribs turbulators:** (+) *V – Shaped*  $45^\circ$ , (—) *V – Shaped*  $60^\circ$ , (----) *V – Shaped*  $75^\circ$ , (.....) *Inclined Ribs*  $45^\circ$ , (---) *Inclined Ribs*  $60^\circ$ , (---) *Inclined Ribs*  $90^\circ$ .

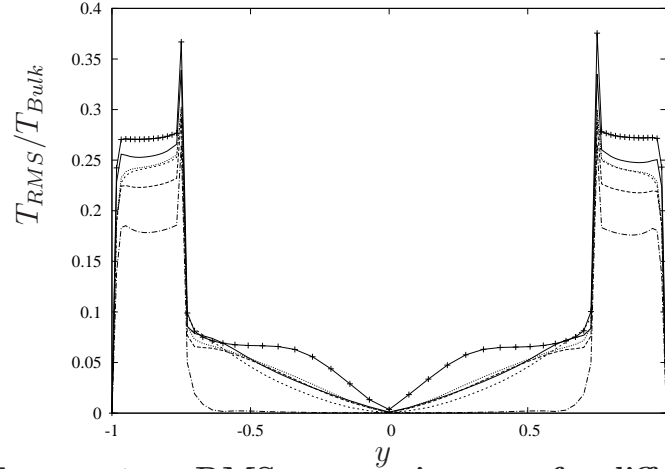


**Figure B–9: Temperature RMS average in space for different ribs turbulators.** (+) *V – Shaped* 45°, (—) *V – Shaped* 60°, (----) *V – Shaped* 75°, (– · – ·) *Inclined Ribs* 45°, (– – –) *Inclined Ribs* 60°, (– – –) *Inclined Ribs* 90°.

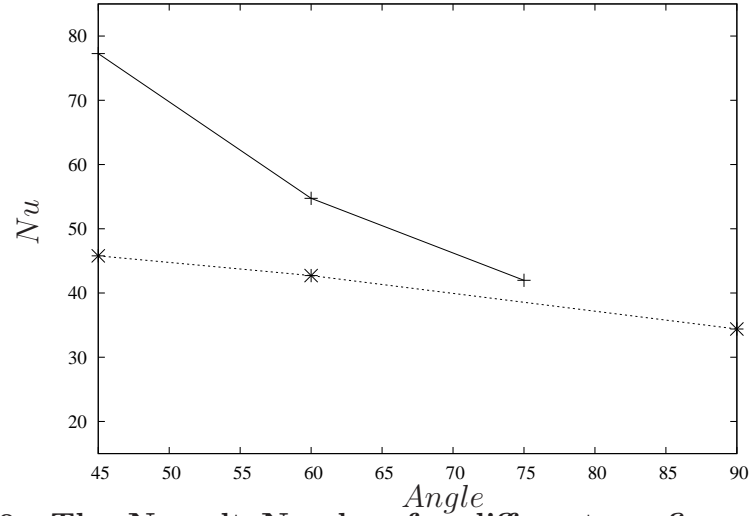
## B.5 Root Mean Square Temperature

Figure B–9 presents the temperature RMS. The temperature RMS is smaller at the center of the channel, while it is large in the cavity region. This means that close to the wall the temperature has a significantly difference between the average temperature and the mean temperature, while at the center of the channel this difference is very small. The V-Shape turbulator of 45° is the configuration with the highest temperature RMS. The transverse square bars inclined turbulators of 90° present the lowest temperature RMS.

## B.6 Nusselt Number

The Nusselt number (Nu) is a parameter that provides a measure of the convective heat transfer occurring at the surface of the channel. The Nu is defined by the difference of non-dimensional temperature with the difference of the non-dimensional distance at the surface (see Eq. 4.2).

The configuration with the highest Nusselt number is the V-shaped turbulator of 45° and this result is expected because this was the configuration with the highest gradient temperature in the wall (see Fig. B–8) and was the highest configuration that present the velocity RMS in the cavity area.



**Figure B-10:** The Nusselt Number for different configurations of ribs turbulators. (+) V-Shape and (\*) Square Bars.

## B.7 Skin Friction and Form Drag

The skin friction arises from the contact between the fluid and the surface of the channel (Eq. 4.3). The different turbulators present a form drag due to the difference between the pressure on the leading and trailing face of the turbulators. The form drag was calculated projecting the pressure force onto the streamwise direction (Eq. 4.4). The total drag is the sum of the following components, the skin friction coefficient and the form drag.

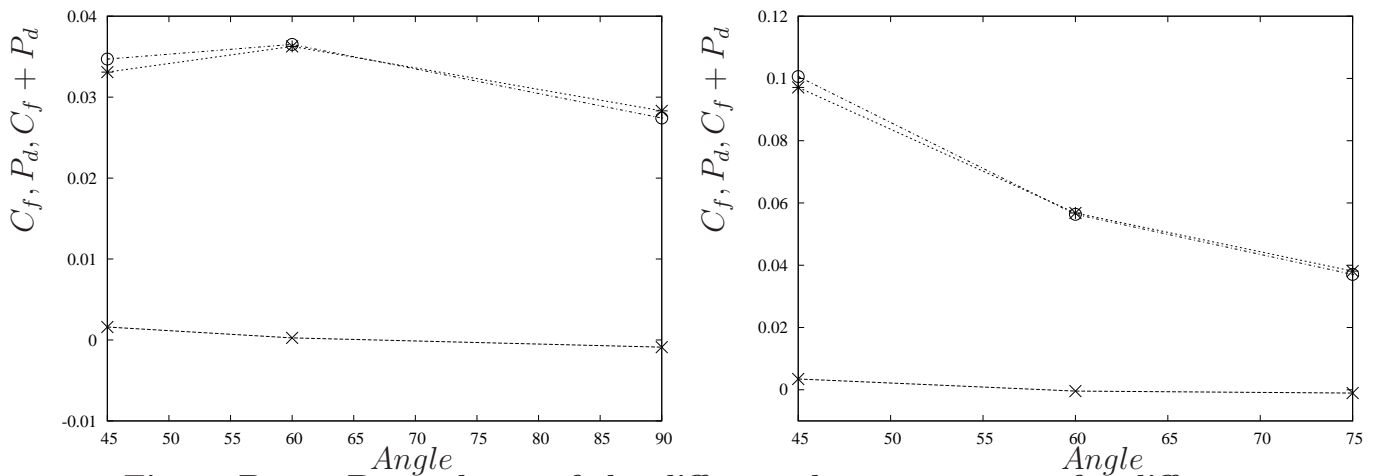


**Figure B-11:** Dependence of the different drag component for different ribs turbulators:  $C_f$  (×), form drag  $P_d$  (\*) and total drag  $C_f + P_d$  (○). Left: Square Bars Turbulators Inclined, Right: V-Shape Turbulators.

Figure B-11 shows the plot of the different drag component for the different configurations. The square bars turbulator inclined  $60^\circ$  presents the highest a total drag of all square bars turbulators inclined configurations. In this case the skin friction of 0.0002551 is very close to zero but the form drag that has a value of 0.03626. In these plot is very clear that the major component of the total drag is the form drag. For the V-shaped turbulators configurations the highest total drag occurs for V-shaped turbulator with an angle of  $45^\circ$ . The skin friction of this configuration is equal to 0.003481 and the form drag is 999. The total drag for the V-Shape turbulators of  $45^\circ$  is 999 which is the configuration with the highest total drag compared with all other turbulator configurations. For the V-shaped configurations, the V-shaped  $45^\circ$  is the only one that has a positive value of skin friction. The other V-shaped turbulators present a higher recirculation in the cavity area which is the cause of a negative friction coefficient.

## REFERENCE LIST

- [1] Kim, K. and Y. Lee. Design optimization of internal cooling passage with V-Shaped ribs. *Numerical Heat Transfer, Part A*, 51:1103–1118, 2007.
- [2] Han, J.C., S. Dutta , and S. Ekkad. *Gas Turbine Heat Transfer and Cooling Technology*. Taylor and Francis, 2000.
- [3] Moran, M.J. and H.N. Shapiro. *Engineering Thermodynamics*. John Wiley and Sons, Inc., 2008.
- [4] Han, J.C. Recent Studies in Turbine Blade Cooling. *International Journal of Rotational Machinery*, 10(6):443–457, 2004.
- [5] Ashrafiyan, A., H. Andersson and M. Manhart. DNS of turbulent flow in a rod-roughened channel. *International Journal of Heat and Fluid Flow*, 25:373–383, 2004.
- [6] Orlandi, P. and S. Leonardi. DNS of turbulent channel flows with two- and three-dimensional roughness. *Journal of Turbulence*, 7:1–22, 2006.
- [7] Leonardi, S., P. Orlandi , and R.A. Antonia. Heat transfer in a turbulent channel flow with roughness. *5th International Symposium on Turbulence and Shear Flow Phenomena. TU Munich 2729 August 2007.*, 2007.
- [8] Orlandi, P., S. Leonardi, L. Djenidi and R.A Antonia. Structure of the turbulent channel flow with square bars on one wall. *International Journal of Heat and Fluid Flow.*, 25:384–392, 2004.
- [9] Lee, D.H., D.H. Rhee, K.M. Kim, H.H. Cho, and H.K. Moon Detailed measurement of heat/mass transfer with continuous and multiple V-Shaped ribs in rectangular channel. *Energy. doi:10.10196/j.energy.2009.07.011*, 2009.

- [10] Jaime A. Toro Medina. *Direct Numerical Simulation Of Turbulent Channel Flow With V-Shape Turbulators*. University of Puerto Rico Mayaguez Campus. May 2010.
- [11] Han, J.C., H.C. Chen and Y.J. Jan. Flow and Heat Transfer in a Rotating Square Channel with 45 deg Angled Ribs by Reynolds Stress Turbulence Model. *ASME Paper*, 123:124–132, 2001.
- [12] Kelecy, F.J. Coupling Momentum and Continuity Increases CFD Robustness. *ANSYS Advantage*. Volume II, Issue 2, 2008.
- [13] Han, J.C., Y.M. Zhang and C.P. Lee. Augmented Heat Transfer in Square Channels With Parallel Crossed, and V-Shaped Angled Ribs. *Int. Heat Mass Transfer*, 21(8):1143–1156, 1991.
- [14] Leonardi, S., P. Orlandi, R.J. Smalley, L. Djenidi and R.A. Antonia. Direct numerical simulations of turbulent channel flow with transverse square bars on one wall. *Journal Fluid Mechanics.*, 491:229–238, 2003.
- [15] Sundén, B. Enhancement of Convective Heat Transfer in Rib-Roughness Rectangular Ducts. *J. Enhanced Heat Transfer*, 6:89–103, 1999.
- [16] Incropera F.P. and D.P. DeWitt. *Fundamentals of Heat and Mass Transfer*. John Wiley and Sons, Inc., 2002.
- [17] Versteeg, H.K. and W. Malalasekera. *An Introduction to Computational Fluid Dynamics. The Finite Volume Method*. PEARSON. Prentice Hall, 2007.
- [18] Tu, J., G.H. Yeoh and C. Liu. *Computational Fluid Dynamics. A practical Approach*. Butterworth-Heinemann, 2008.
- [19] John A. Lucena Jimenez. *DNS of Turbulent Channel Flow with Inclined, Continuous and Segmented V-Shape Turbulators*. University of Puerto Rico Mayaguez Campus. May 2011
- [20] Jia, R., B. Sundén and M. Faghri. Computational Analysis of Heat Transfer Enhancement in Square Ducts With V-Shaped Ribs: Turbine Blade Cooling.

*Journal Fluid Mechanics.*, 491:229–238, 2003.

- [21] Moin, P. and J. Kim The Structure of the Vorticity Field in Turbulent Channel Flow. Part 1. Analysis of instantaneous field and statistical correlations. *Journal Fluid Mechanics.*, 155: 441–464, 1985.
- [22] Blackwelder, R. and R.E. Kaplan. On the wall of the turbulent boundary layer. *Journal Fluid Mechanics.*, 76:89–112, 1976.

**HEAT TRANSFER IN TURBULENT CHANNEL FLOW WITH  
ROUGHNESS ON THE WALLS: NUMERICAL SIMULATION**

Amabel Reyes Rondon

(787) 942-7378

Department of Mechanical Engineering

Chair: Stefano Leonardi

Degree: Master of Science

Graduation Date: December 2011